

# **Power spectral density accuracy in Chirp Transform Spectrometers**

Dissertation  
zur Erlangung des Doktorgrades  
der Fakultät für Angewandte Wissenschaften  
der Albert-Ludwigs-Universität Freiburg im Breisgau

vorgelegt von  
**Lucas Paganini**  
aus Mendoza / Argentinien

Freiburg 2008

## **Bibliografische Information Der Deutschen Bibliothek**

Die Deutsche Bibliothek verzeichnet diese Publikation in der Deutschen Nationalbibliografie; detaillierte bibliografische Daten sind im Internet über <http://dnb.ddb.de> abrufbar.

D7

Referent: Prof. Dr. Leonhard Reindl

Korreferent: Prof. Dr. Oskar von der Lühe

Tag der mündlichen Prüfung: 27. März 2008

ISBN 978-3-936586-83-1

Copernicus Publications 2008

<http://publications.copernicus.org>

© Lucas Paganini

Printed in Germany

*To my family*



# Contents

<b>Abstract</b>	<b>ix</b>
<b>Zusammenfassung</b>	<b>xi</b>
<b>List of Figures</b>	<b>xv</b>
<b>List of Tables</b>	<b>xvii</b>
<b>List of Symbols</b>	<b>xix</b>
<b>1 Introduction</b>	<b>1</b>
1.1 Thesis Overview . . . . .	1
1.2 Microwave heterodyne spectroscopy . . . . .	3
1.2.1 Fundamentals . . . . .	4
1.2.1.1 Blackbody radiation and the brightness temperature . .	4
1.2.1.2 The relationship of thermal blackbody radiation and antenna temperature . . . . .	5
1.2.2 Heterodyne receivers . . . . .	5
1.2.3 Calibration . . . . .	6
1.2.4 The radiometer formula . . . . .	7
1.2.5 Scientific applications . . . . .	8
1.3 Aims of this thesis . . . . .	10
<b>2 The 400-MHz bandwidth CTS</b>	<b>13</b>
2.1 Introduction to CTSs . . . . .	13
2.2 The Chirp transform principle . . . . .	15
2.3 Development and design . . . . .	16
2.3.1 The dispersive filters . . . . .	21
2.3.2 Digital chirp generation, the DDS board . . . . .	23
2.3.2.1 The direct digital synthesizers . . . . .	23
2.3.3 Time synchronization . . . . .	26
2.3.4 Operating multiple AD9858s instances . . . . .	26
2.3.5 Recommendation on parallel AD9858s architecture . . . . .	27
2.3.5.1 Bypassing the REFCLK divide-by-2 . . . . .	27
2.3.5.2 Synchronizing SYNCLK among all DDSs . . . . .	27
2.3.5.3 Meeting setup and hold times between FUD and SYN- CLK . . . . .	28

2.3.6	The DDS and ASIC boards synchronization . . . . .	28
2.4	Characterization. Test measurements . . . . .	29
2.4.1	Analysis of the chirp signal . . . . .	29
2.4.2	Frequency and time domain analyses . . . . .	30
2.4.3	Stability . . . . .	32
2.4.4	Spectral resolution . . . . .	36
2.4.5	Power linearity and dynamic range . . . . .	37
2.5	Observations and results . . . . .	39
2.5.1	Ozone measurements . . . . .	40
2.5.2	Astronomical observations at the Heinrich Hertz Submillimeter Telescope (HHSMT) . . . . .	42
2.5.2.1	Comets . . . . .	42
2.5.2.2	Mars and other sources . . . . .	47
2.6	Analysis and performance . . . . .	48
2.7	Outlook . . . . .	53
<b>3</b>	<b>Impacts of nonlinearity in heterodyne systems</b>	<b>55</b>
3.1	Ground-based microwave spectroscopy of the Earth's atmosphere . . . . .	55
3.1.1	The atmosphere as physical system . . . . .	55
3.1.2	Physical properties. Composition and structure . . . . .	56
3.1.3	Absorption and emission by gases . . . . .	58
3.1.4	The shape of a spectral line . . . . .	58
3.1.5	Theory of radiative transfer . . . . .	59
3.1.6	Inversion technique . . . . .	60
3.2	Numerical analysis . . . . .	60
3.3	Simulations on the Earth's atmosphere . . . . .	66
3.4	Other sources of instrumental error . . . . .	67
3.4.1	Sky window . . . . .	67
3.4.2	Reference loads . . . . .	68
3.4.3	Single sideband filter . . . . .	68
3.5	Discussion . . . . .	68
<b>4</b>	<b>On the high accuracy of measured spectra</b>	<b>77</b>
4.1	Linearity . . . . .	77
4.2	Intercomparisons . . . . .	78
4.3	Linearity measurements . . . . .	80
4.3.1	A 3-dimensional analysis method . . . . .	81
4.3.1.1	Examples . . . . .	84
4.3.1.2	Improvements provided by this method . . . . .	84
4.3.2	A novel high-accuracy method . . . . .	87
4.3.2.1	Gain fluctuations . . . . .	90
4.3.2.2	Measurement results . . . . .	92
4.3.2.3	Methodology applied to CTSs . . . . .	92
4.3.2.4	Improvements . . . . .	96
4.4	The importance for future developments . . . . .	99

<b>5 Concluding remarks</b>	<b>101</b>
<b>A Receiver calibration</b>	<b>103</b>
A.1 Determination of the antenna temperature, $T_A$ . . . . .	103
A.2 Determination of the receiver temperature, $T_R$ . . . . .	103
<b>B Circuit diagrams</b>	<b>105</b>
<b>C Observations and data reduction</b>	<b>109</b>
C.1 Calibration and telescope efficiency . . . . .	109
<b>D Details of devices under test</b>	<b>113</b>
<b>Bibliography</b>	<b>115</b>
<b>Publications</b>	<b>125</b>
<b>Acknowledgements</b>	<b>127</b>
<b>Lebenslauf</b>	<b>129</b>



# Abstract

Heterodyne spectroscopy is a technique providing practically unlimited spectral resolution. Even the smallest features of atmospheric spectral lines can be resolved in frequency using this technique. This is especially important, for instance, in the study of planetary atmospheres where the structure of molecular transition lines provides detailed information about molecular distribution, temperature and pressure profiles along the line of sight. This thesis aims to address the specific properties required to maximize the reliability in heterodyne-system responses focusing mainly on the effects of nonlinear behavior in chirp transform spectrometers.

In this investigation, a comprehensive description and characterization of a new 400-MHz bandwidth Chirp Transform Spectrometer (CTS) with 100 kHz spectral resolution are presented. In order to achieve the 400-MHz bandwidth, a newly developed DDS board, driven by a 1-GHz fixed frequency clock source, creates a chirp signal using digital techniques. Novel methods have been applied to the RF section in the CTS, since the intrinsic properties of the SAW filter (with a bandwidth equal to 400 MHz) requires an input signal two times larger than the SAW filter's bandwidth. Furthermore, this spectrometer has been applied to atmospheric science, i.e. a 142-GHz ozone system by detecting the 142.175-GHz rotational transition of ozone in the Earth's atmosphere. In addition, the CTS system was used for astronomical observations at the Heinrich Hertz Submillimeter Telescope during the observation run of the 73P/Schwassmann-Wachmann 3 comet in May 2006, during the comet's closest approach to the Earth.

Any deviation from the spectrometer's (ideal) linear dynamic range may induce significant effects in the spectra, therefore, it is essential to model these deviations such that they are accounted for. These analyses are performed by means of numerical calculations and simulations which show how these deviations in the spectra might produce considerable changes in the retrieved vertical profile of trace gases in planetary atmospheres.

In several examples, deviations are evidenced in the measured spectra of heterodyne systems. Thus, two novel experiments were conducted in order to analyze the behavior of nonlinearity in backend spectrometers. Based on a differential approach, both analyses provide an effective solution in the identification of nonlinear processes.

Finally, experimental results in the ozone-radiometer test facility at the Max Planck Institute for Solar System Research (MPS) show the improvements in the 400-MHz-BW CTS response. It is confirmed that the overall deviations introduced by nonlinearity in the spectrometer have been decreased and thus the performance of the backend instrument has been improved.



# Zusammenfassung

Die Heterodyne-Spektroskopie ist eine Technik, die praktisch unbegrenzte spektrale Auflösung ermöglicht. Das heisst, dass selbst die kleinsten Kenndaten der atmosphärischen Spektrallinien im Frequenzraum aufgelöst werden können. Dies ist beispielsweise besonders wichtig bei der Erforschung der planetaren Atmosphären, bei der die Strukturen der molekularen Übergangslinien detaillierte Informationen über die molekulare Distribution, Temperaturen und Druckprofile entlang der Sichtlinie bieten. Ziel dieser Arbeit ist es die spezifischen Eigenschaften zur Maximierung der Zuverlässigkeit des Heterodyne-System Ansprechverhalten zu ermitteln, wobei hauptsächlich auf die Effekte nicht linearen Verhaltens in Chirptransformations-Spektrometern eingegangen werden soll.

In dieser Arbeit wird die komplette Beschreibung, Charakterisierung und Verbesserungen des neuen 400-MHz-Bandbreite Chirptransformations-Spectrometer (CTS) mit 100 kHz spektraler Auflösung vorgenommen. Um eine 400-MHz Bandbreite zu erzielen, erzeugte ein neu entwickeltes DDS-Board, dass durch eine feste Taktfrequenz von 1 GHz angetrieben wurde, ein Chirp-Signal mit Hilfe digitaler Techniken. Neue Methoden wurden am RF-Abschnitt im CTS angewandt, da die intrinsischen Eigenschaften des SAW-Filters (mit einer Bandbreite von 400 MHz) ein Eingangssignal erforderten, dass zwei mal grösser als die Bandbreite des SAW-Filter war. Dieses CTS wird in der Atmosphärforschung angewendet, d.h. in einem 142-GHz Ozonsystem (Radiometer) durch Erkennung des 142,175-GHz Rotatoinübergangs des Ozons in der Erdatmosphäre. Ferner werden Ergebnisse astronomischer Beobachtungen des Kometen 73P/Schwassmann-Wachmann 3 vorgestellt die, im Mai 2006, als er sich der Erde am nächsten befand, an dem Heinrich Hertz Submillimeter Teleskop gewonnen wurden.

Des weiteren wurden die möglichen Auswirkungen auf die gemessenen Spektren im Falle einer Abweichung von dem idealen linearen Dynamikbereich des Spektrometers untersucht. Solche Analysen wurden durch numerische Berechnungen und Simulationen ausgeführt. Diese zeigen wie Abweichungen in den Spektren signifikante Unterschiede in den gewonnenen vertikalen Profilen der Spurengase in planetaren Atmosphären hervorrufen können.

Nachdem Beispiele dargelegt wurden in denen Nichtlinearität in den gemessenen Spektren des Heterodyne-System gefunden wurden, wurden zwei neuartige Experimente entwickelt, welche die Analyse der Nichtlinearität bei Backend-Spektrometern erleichtern sollen. Auf der Grundlage eines differenziellen Ansatzes, boten beide Analysen eine effektive Lösung für die Identifikation nonlinearer Prozesse.

Abschliessend konnten durch experimentelle Ergebnisse des Ozonradiometer-Tests am Max-Planck-Institut für Sonnensystemforschung (MPS) Verbesserungen des 400-MHz-BW CTS Ansprechverhaltens nachgewiesen werden. Es wurde bestätigt, dass die gesamten Abweichungen die durch die Nichtlinearität im Spektrometer hervorgerufen wurden, ge-

mindert wurden und somit die Arbeitsleistung des Backend-Instrumenten verbessert werden konnte.

# List of Figures

1.1	Simple block diagram of a heterodyne receiver system. . . . .	4
1.2	Calibration of antenna temperature using two blackbody emitters (the hot and cold loads). . . . .	7
1.3	The electromagnetic spectrum. . . . .	9
2.1	The CTS working principle. . . . .	15
2.2	Multiplication and convolution with chirp waveforms. . . . .	16
2.3	The 400-MHz bandwidth chirp transform spectrometer. . . . .	17
2.4	The analog part. . . . .	18
2.5	The digital part. . . . .	19
2.6	Compressed pulse observed at the end of the analog part and before the digital acquisition by an oscilloscope for a 2.1-GHz CW input. . . . .	20
2.7	The real and imaginary components (red and green lines) are obtained by mixing the signal with a complex source. . . . .	21
2.8	The reflective array compressor (RAC). . . . .	22
2.9	DDS-board circuit diagram. . . . .	24
2.10	The DDS-based chirp principle. . . . .	24
2.11	AD9858: Internal synchronization block diagram. . . . .	25
2.12	AD9858 programming: Timing diagram. . . . .	26
2.13	Synchronizing the DDS and ASIC boards . . . . .	28
2.14	Chirp-signal analysis tools: simulated perfect chirp signal. . . . .	30
2.15	Chirp signal tools applied to the DDS board's output. . . . .	31
2.16	New analysis approach using Short-Term Fourier Transform (STFT) computation. . . . .	32
2.17	Frequency- and time-domain answers provided by the DDS board before the first up-conversion stage. . . . .	33
2.18	Frequency- and time-domain answers given by the first up-conversion process. . . . .	34
2.19	Frequency- and time- domain answers provided by the mixing stage where the incoming measured signal is mixed with the 800-MHz bandwidth chirp signal. . . . .	35
2.20	Allan variance calculation. . . . .	36
2.21	Spectral resolution and frequency linearity vs. channel number. . . . .	37
2.22	Power linearity. . . . .	38
2.23	Power linearity study: a 3D power analysis. . . . .	38
2.24	CTS data-observing software plot. . . . .	39

List of Figures

---

2.25	First light of the 400-MHz bandwidth CTS. . . . .	41
2.26	Calibration process. . . . .	43
2.27	As the comet approaches the Sun, the icy material begins to sublime, releasing dust and gas from the rocky nucleus. . . . .	45
2.28	Comet 73P/Schwassmann-Wachmann 3: an image showing several fragments. . . . .	45
2.29	HCN(3-2) emission line of the 73P-B/Schwassmann-Wachmann 3 comet during its closest approach on May 17, 2006 at HHSMT on Mt. Graham, Arizona. . . . .	46
2.30	Spectral map of the HCN(3-2) emission line of the 73P-B/Schwassmann-Wachmann 3 comet on May 12, 2006. . . . .	48
2.31	HCN $J = 3 \rightarrow 2$ emission from 73P-B/Schwassmann-Wachmann 3 (fragment B) on 12 May, 2006. . . . .	49
2.32	HCN $J = 3 \rightarrow 2$ emission from 73P-C/Schwassmann-Wachmann 3 (fragment C) on 12 May, 2006. . . . .	49
2.33	$^{12}\text{CO } J = 2 \rightarrow 1$ absorption line of Mars. . . . .	50
2.34	Observation of the N7538IRS1 star. . . . .	50
2.35	Observation of the Egg Nebula, also known as CRL2688 (used as a standard source). . . . .	51
3.1	Standardized Temperature Profile (the Earth's atmosphere). . . . .	57
3.2	Measurement geometry for the passive remote sensing of atmospheres. . . . .	59
3.3	Calibration of antenna temperature in case there is a possible nonlinear response. . . . .	61
3.4	Deviations ( $\Delta T_A$ ) for different values of $T_L$ which might appear in case of three different levels of nonlinearity. . . . .	64
3.5	Variations produced by a 50-mK standing wave for $R = 1.05$ . . . . .	66
3.6	Simulated effects in the spectral intensity of a synthetic spectrum: subtracting 5-K spectral intensity deviation over the line center. . . . .	69
3.7	Simulated effects in the spectral intensity of a synthetic spectrum: subtracting 1.5-K spectral intensity deviation over the line center. . . . .	70
3.8	Simulated effects in the spectral intensity of a synthetic spectrum: adding 1.5-K spectral intensity deviation over the line center. . . . .	71
3.9	Simulated effects in the spectral intensity of a synthetic spectrum: adding 5-K spectral intensity deviation over the line center. . . . .	72
3.10	Simulated effects in the spectral intensity of a synthetic spectrum: adding 1.9-K spectral intensity deviation over the wings. . . . .	73
3.11	Simulated effects in the spectral intensity of a synthetic spectrum: subtracting 0.4-K spectral intensity deviation over the wings. . . . .	74
3.12	Simulated effects in the spectral intensity of a synthetic spectrum: subtracting 0.4-K spectral intensity deviation over the wings. . . . .	75
3.13	Simulated effects in the spectral intensity of a synthetic spectrum: subtracting 1.2-K spectral intensity deviation applied in the wings. . . . .	76
4.1	Nonlinear behavior observed on intercomparison tests during September/November 2006. . . . .	79

---

4.2	3-dimensional measurement test setup. . . . .	82
4.3	Methods comparison: Traditional method vs. 3D differential method. . .	83
4.4	3D analysis applied to an RF ZFM-4212 mixer. . . . .	84
4.5	3D analysis method applied to an RF ZFM-15 mixer. . . . .	85
4.6	3D analysis method applied to an RF MCA-35LH mixer. . . . .	85
4.7	3D analysis method applied to an RF ABA-53563 amplifier. . . . .	86
4.8	3D analysis method applied to an RF MGA-82563 amplifier. . . . .	86
4.9	3D analysis method applied to the spectrometer's input stage. . . . .	87
4.10	3D analysis over a mixing stage in the 400-MHz bandwidth CTS using the ZFM-4212 mixer. . . . .	88
4.11	Achieved improvements by the 3D analysis method. . . . .	89
4.12	Scheme of the high-accuracy method. . . . .	89
4.13	Temperature variations on a 3-day-long analysis under laboratory condi- tions at MPS. . . . .	90
4.14	Information provided by the high-accuracy method. . . . .	91
4.15	High-accuracy method applied to an RF ABA-51563 amplifier. . . . .	93
4.16	High-accuracy method applied to an RF ABA-53563 amplifier. . . . .	93
4.17	High-accuracy method applied to an RF ABA-54563 amplifier. . . . .	94
4.18	High-accuracy method applied to an RF MSA-0735 amplifier. . . . .	94
4.19	High-accuracy method applied to an RF MCA-35LH mixer. . . . .	95
4.20	High-accuracy method applied to an RF ZFM-4212 mixer. . . . .	95
4.21	High-accuracy method applied to an RF ZFM-15 mixer. . . . .	96
4.22	Crucial regions ('zones') in the CTS. . . . .	97
4.23	High-accuracy method applied over zones 1, 2 and part of 3. . . . .	98
4.24	High-accuracy method applied over zone 4. . . . .	98
4.25	Achieved improvements by the high-accuracy method. . . . .	100
B.1	System diagram of the 400-MHz BW CTS. . . . .	106



# List of Tables

1.1	Sensitivity constants $K$ of different receiver configurations . . . . .	8
2.1	Specifications of current CTS system . . . . .	40
3.1	Calculated temperature deviations in case of nonlinearity . . . . .	65
4.1	Specifications for the R&S RSP step attenuators . . . . .	82
4.2	Specifications for the Agilent 11713A (+84904K) . . . . .	82
4.3	Specifications for the R&S FSP30 spectrum analyzer . . . . .	83
4.4	Methods comparison: measurement-uncertainty calculation . . . . .	83
4.5	Specifications for the R&S NRP-Z21 power meter (20 °C to 25 °C) . . . . .	90
B.1	RF components in the 400-MHz BW CTS . . . . .	107
C.1	Some useful physical constants and quantities . . . . .	110
C.2	Operator's log file. Map of the HCN(3-2) emission line of 73P-B . . . . .	111
C.3	Operator's log file. Map of the HCN(3-2) emission line of 73P-C . . . . .	112
D.1	Devices under test: Amplifiers . . . . .	114
D.2	Devices under test: Mixers . . . . .	114



# List of Symbols

$\alpha$	absorption coefficient
$P_A$	antenna power
$T_A$	antenna temperature
$B$	bandwidth (also BW)
$\theta_b$	beam size
$k$	Boltzmann's constant
$T_B$	brightness temperature
$T_{mb}$	brightness temperature as measured by the main diffraction beam of the telescope
$T_{bg}$	brightness temperature of the cosmic background radiation
$\mu$	chirp slope
$\mu_c$	chirp slope of compressor
$\mu_e$	chirp slope of expander
$P_C$	cold-load power
$C$	cold-load position
$T_C$	cold-load temperature
$\phi$	comet's elongation angle
$\beta$	comet's phase angle
$\eta_m^*$	corrected main beam efficiency
$Dec$	Declination offset
$r$	deviation from linearity
$t_C$	dispersion time of compressor
$t_E$	dispersion time of expander
$E_e$	electronic energy
$\eta_l$	forward efficiency
$F$	forward model
$\eta_{fss}$	forward scattering and spillover efficiency
$\nu$	frequency
$\Delta f$	frequency resolution
$\nu_o$	frequency of absorbed (or emitted) quantum
$\Delta$	geocentric distance
$z$	geometrical height (h)
$r$	heliocentric distance
$H$	hot-load position
$P_H$	hot-load power
$T_H$	hot-load temperature

## List of Symbols

---

$G$	internal gain of the receiver system
$F_{(\omega)}$	input signal in frequency domain
$f_{(t)}$	input signal in time domain
$\tau$	integration time
$\eta_{mb}$	main beam efficiency
$P_{lin}$	measured power considering (ideal) linear response
$y_{(v)}$	measured signal as a function of frequency
$k$	minimum Allan-variance time
$x_{(h)}$	mixing ratio
$K$	noise performances of different receiver configurations
$\tau$	opacity (or optical depth)
$h$	Planck's constant
$s$	point along a line in the direction of propagation
$PsAng$	position angle of the extended radius vector
$P$	power
$\Delta T_A$	Pseudo-Noise of a measured spectrum
$R$	$r_{max}$
$\Delta T$	radiometric sensitivity (or radiometer noise formula)
$T_R$	receiver noise temperature
$RA$	Right Ascension offset
$E_r$	rotational energy
$SPNR$	Signal to Pseudo-Noise Ratio
$A$	sky/atmosphere position
$I_v$	specific intensity
$B_v(T)$	spectral distribution of a blackbody
$c$	speed of light
$T_R^*$	source antenna temperature corrected for atmospheric attenuation, radiative loss, and rearward and forward scattering and spillover
$T_A^*$	source antenna temperature of the telescope corrected for atmospheric attenuation, radiative loss, and rearward scattering and spillover
$\eta_{cmb}$	source coupling between a disk source like the planets and a Gaussian
$T_R$	source radiation temperature
$\theta_s$	source size
$g$	system-gain factor
$T_S$	system temperature
$\eta_{mb}$	telescope efficiency (using a measurement of the continuum brightness of a planet)
$T$	temperature
$B(T)$	total brightness of a blackbody
$E$	total internal energy
$E_v$	vibrational energy
$\lambda$	wave longitude
$y$	y-factor

# 1 Introduction

In microwave heterodyne spectroscopy the short wavelength (15 mm – 0.5 mm) atmospheric emission (from planets or comets) entering the system is down-converted by a heterodyne receiver to larger wavelengths (typically 1000 mm – 50 mm). In this relatively low frequency range, electronic spectral analysis tools (real-time spectrometry) can be applied. Since these methods provide, in principle, arbitrary high spectral resolution, even the smallest features of atmospheric spectral lines can be resolved in frequency. For most astronomical objects the spectrometer should be highly accurate on the frequency scale, while, as a general rule, the power spectral density (PSD) should be known with better than 10%. The main exceptions from this rule are spectra of planetary atmospheres. The shape of planetary spectra are determined by the molecular parameters of the observed gas, the atmospheric temperature/density profile and the number density profile of the observed molecule, all along the line of sight. The molecular mass ratio of the observed gas and the main collider (for instance  $N_2/O_2$  in the Earth's atmosphere or  $CO_2$  in the Martian atmosphere) determines the pressure broadening parameter. With all these parameters known, the exact spectral shape can be calculated using a microwave radiative transfer model. Temperature and density may be approximated from climatological data provided by either another observation method or by simultaneous measurement of the same gas (i.e. several spectra) with different temperature sensitivity of the molecular parameters. Later, the number density profile of the observed gas along the line of sight can be inverted from a measured spectral line by using special retrieving techniques.

## 1.1 Thesis Overview

A former PhD thesis describes the development of a chirp transform spectrometer for SOFIA-GREAT, an airborne observatory carrying the "German REceiver for Astronomy at THz frequencies" (<http://www.sofia.gov>). The SOFIA-GREAT CTS has a bandwidth of 220 MHz and a spectral resolution of 47 kHz (Villanueva, 2004, Villanueva and Hartogh, 2004). In order to obtain the signal's spectral information, a pulse compression system is composed by an expander-compressor arrangement usually accomplished by means of Surface Acoustic Wave (SAW) devices (Hartogh, 1989). As part of his work Villanueva (2004) proposes a new means to perform the expander duty, the Adaptive Digital Chirp Processor (ADCP). The function of the ADCP is to digitally create the dispersive signal, i.e. the so-called chirp signal, using direct digital synthesis techniques (Villanueva et al., 2006a). The effectiveness behind the ADCP design relies on the feature to digitally modify the dispersive properties in order to match those of the compressor system as stated in Eq. 2.7 (see Section 2.2).

This investigation covers three major topics. Similarly, the first one presents the description and characterization of a new Chirp Transform Spectrometer (CTS). This CTS was developed with 400 MHz bandwidth and 100 kHz spectral resolution, thereby providing the advantage of a broader bandwidth analysis. As in the case of the SOFIA-GREAT CTS it uses digital techniques to generate the chirp signal. In the 400-MHz bandwidth CTS, however, a new DDS board was developed using a higher-frequency direct digital synthesizer (DDS) technology. Driven by a 1-GHz fixed frequency clock source, the new DDS entails more complex synchronization characteristics to create a chirp signal with a total bandwidth of 800 MHz (after RF doubling process). In addition, the RF processing of the analog chirp signal involves new techniques to match a new dispersive line, i.e. the SAW filter, with a 400-MHz bandwidth (although, the latter has not been developed within the scope of this thesis). The preprocessing unit (the ASIC board), based on a Complementary Metal Oxide Semiconductor (CMOS) and an Application-Specific Integrated Circuit (ASIC), is similar to the one used for the SOFIA-GREAT CTS, however, its clock comprises a higher frequency equal to 200 MHz (which is within the specification tolerance). Next, standard test analyses are performed to conduct the instrument's characterization, e.g. stability (i.e. the Allan-variance test), spectral resolution, and power linearity and dynamic range. Furthermore, novel ones, such as testing of the chirp signal (using Short-Term Fourier Transform analysis), frequency- and time-domain analyses, and 3D power analysis, are additionally implemented. Later, as in the case of Villanueva (2004), the 400-MHz bandwidth CTS is tested at the Heinrich Hertz Submillimeter Telescope (HHSMT) as a demonstration of its capabilities in Radio Astronomy. Following, the 400-MHz bandwidth CTS and the SOFIA-GREAT CTS are characterized in an ozone radiometer for comparison tests of their PSD response.

The second topic seeks to theoretically demonstrate the importance of high power-spectral-density accuracy in heterodyne systems and hence possible implications of systematic errors into the retrieval of atmospheric species, such as those created by small deviations on the PSD from a proper value. Hartogh (1989) suggested the examination on how considerable these effects would become in case there is deviation from the spectrometer's ideal linear dynamic range in heterodyne systems. Studies such as by Kleipool et al. (2000), de La Noë (1998), Kuntz et al. (1997), Seele (1999) analyze typical instrumental sources of errors for a passive heterodyne system; e.g., image sideband contribution, continuum emission, random noise and standing wave. In practice, these error sources induce uncertainties in the derived atmospheric information. These studies, however, are limited to analyze the frontend system without mentioning the power spectral density accuracy in the backend-spectrometer. In this study, numerical calculations demonstrate how considerable the deviations are from the heterodyne system's ideal linear dynamic range. Moreover, these calculations are based on a 142-GHz ozone radiometer with a receiver temperature  $T_R = 500$  K, a 78 K liquid-nitrogen cold load and a hot load at 300 K, i.e.  $T_C = 578$  K and  $T_H = 800$  K respectively (the one used for experimental analyses of the 400-MHz bandwidth CTS). Also, simulations in the ozone retrieval (in the Earth's atmosphere) illustrates the effects of line amplitude deviations, i.e. in the power spectral density, by producing arbitrary variations in both the line center and wings of a generated synthetic ozone spectrum. The aim is to account for the effects of such deviations in the synthetic spectrum by observing changes in the retrieved vertical profile. In here, the profiles are retrieved by using the Optimal Estimation Method (OEM) of Rodgers (1976)

using an existing radiative transfer model (Jarchow and Hartogh, 1995, Jarchow, 1998). The results of this investigation suggest that deviations in the ozone's spectral information, as those created by power amplitude deviations, may lead to erratic results in the retrieved volume mixing ratio. Consecutively, these results clearly indicate the importance of high power spectral density accuracy.

Once the importance of the power density accuracy has been addressed, the last topic of this thesis focuses on the detection of PSD error sources. Such deviations are suggested to be produced by small nonlinearities in microwave devices comprising the backend-spectrometer. Unfortunately, the measurement of such linearity characteristics requires low uncertainty where the demand of high accuracy usually outreaches those ones on standard measurement applications. The research on microwave measurements of nonlinearity can be separated at least in two branches: first, the characterization of microwave devices, such as amplifiers and mixers, by means of mathematical models; and second, the measurement instrument itself, i.e., the experimental test setup. In the first case, if the behavior is weakly nonlinear, it is possible to perform nonlinear analysis and modeling of RF devices by power-series or by Volterra-series expansions (for details, see Bedrosian and Rice, 1971, Borremans et al., 2007). Nevertheless, measurements of each relevant parameter (i.e., the kernels of the Volterra-series) can be time consuming, and thus exceeding measurement capabilities. This thesis addresses the second field, i.e. the experimental measurements. Based on a differential approach, two novel high-accuracy experiments facilitate the detection and analysis of possible nonlinear behavior in singular microwave devices or even an arrangement of them, such as RF stages in a CTS. The frequency-discrimination capability of a 3D-analysis method plus the low uncertainty (less than 0.1%) offered by a high-accuracy method provide an effective analysis in the identification of nonlinear features. These experiments are applied to different Devices Under Test (DUT) in the new CTS, such as amplifiers and mixers, to accurately determine their highest possible linear response and so avoid degradation produced by small nonlinear effects.

## 1.2 Microwave heterodyne spectroscopy

Spectrometry is typically divided into two classes according to its particular detection technique. On the one hand, incoherent detection offers a large bandwidth and limited sensitivity where the phase of the signal is lost. On the other hand, coherent (heterodyne) detection is characterized by a frequency conversion to lower frequencies where amplification and spectral analysis can be performed by electronic systems. In the latter, the signal's phase is preserved after the frequency conversion. Heterodyne systems involve two sections (Fig. 1.1): the "front-end" system (usually called a receiver or radiometer) which conducts the detection, frequency translation and amplification of the incoming atmospheric signal; and the "back-end" system which performs the spectral analysis, i.e. the spectrometer (Kraus, 1986).

Microwave heterodyne spectroscopy is the field of science that studies the measurement of electromagnetic radiation. Through proper choice of the radiometer parameters (wavelength, polarization and viewing angle), microwave heterodyne spectroscopy can establish useful relations between the magnitude of the energy received by the ra-

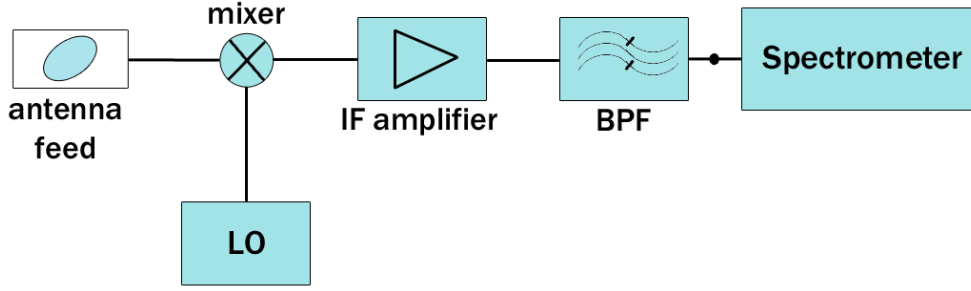


Figure 1.1: Simple block diagram of a heterodyne receiver system composed by: a) the frontend: i.e., the antenna, mixer, local oscillator (LO), band-pass filter (BPF), IF amplifier, and b) the backend: a spectrometer.

diometer and physical properties of the observed astronomical objects. The function of the radiometer is to measure the antenna radiometric temperature ( $T_A$ ), which represents the radiation power delivered by the antenna to the receiver when observing a particular physical process. As a highly-sensitive receiver, the microwave radiometer is capable of measuring low levels of microwave radiation.

## 1.2.1 Fundamentals

This section explains how the radiation resulting from thermal blackbody emission can be related, in the microwave region, to the radiometric antenna temperature measured by a receiver.

### 1.2.1.1 Blackbody radiation and the brightness temperature

The spectral distribution of the radiation of a blackbody in thermodynamic equilibrium is given by *Planck's law*,

$$B_\nu(T) = \frac{2h\nu^3}{c^2} \frac{1}{e^{\frac{h\nu}{kT}} - 1}, \quad (1.1)$$

which gives the power per unit frequency interval. Where,  $h$  is Planck's constant,  $k$  is Boltzmann's constant,  $T$  is the temperature,  $c$  is the speed of light, and  $\nu$  is the frequency. Integrating over  $\nu$ , the total brightness of a blackbody is obtained as

$$B(T) = \frac{2h}{c^2} \int_0^\infty \frac{\nu^3}{e^{\frac{h\nu}{kT}} - 1} d\nu. \quad (1.2)$$

A useful approximation in the (sub)millimeter-wave region is the *Rayleigh-Jeans law*, which allows the Planck function to be represented in a mathematically simpler way,

$$B_\nu(T) \approx \frac{2\nu^2 kT}{c^2} = \frac{2kT}{\lambda^2}. \quad (1.3)$$

Therefore, a brightness temperature,  $T_B$ , is defined by

$$T_B(\nu) = \frac{\lambda^2}{2k} I_\nu, \quad (1.4)$$

where, in large optical depth, the *specific intensity*  $I_\nu$ :

$$I_\nu = B_\nu(T). \quad (1.5)$$

In the Rayleigh-Jeans law, the brightness and the thermodynamic temperature of the blackbody that emits this radiation are proportional. Hence, the  $T_B$  is an important definition in the radiative transfer equation (see Section 3.1.5 for a further discussion of radiative transfer theory).

### 1.2.1.2 The relationship of thermal blackbody radiation and antenna temperature

*Nyquist's law* states that the thermal noise power of a matched resistor is proportional to its temperature. This situation was investigated in 1929 by H. Nyquist. Nyquist's law is closely related to Planck's Law, however, it is derived for the specific case of radiation propagating within a terminated transmission line instead of a general cavity (Janssen, 1993). Nyquist's law states that if the temperature of the matched resistor is  $T$ , then the thermal power  $P$  per unit frequency propagating from a resistor (in the Rayleigh-Jeans limit) is

$$P = kT, \quad (1.6)$$

where  $k$  is Boltzmann's constant. The above correspondence between power and temperature (the random walk process) has led to the definition of the *antenna temperature* to characterize the power emitted by, or received from, an object. In other words, the case where the transmission line is terminated by an antenna immersed in a uniform radiation field resulting from thermal blackbody emission at a temperature  $T$ . Likewise, the thermal power  $P_A$  received by an antenna is related to the antenna temperature  $T_A$  by:

$$T_A \equiv \frac{P_A}{k}. \quad (1.7)$$

If the object observed by the antenna beam is characterized by a uniform brightness temperature  $T_B$  (representing radiation in the direction of the antenna), then  $T_A = T_B$ . In the general case, however,  $T_A$  represents all radiation incident upon the antenna, integrated over all possible directions and weighted according to the antenna directional pattern. Additionally, in the real situation, other factors are also involved. These include the effects of the atmosphere and self-emission by the antenna structure (Ulaby et al., 1981). These factors are accounted for in the radiative transfer theory.

## 1.2.2 Heterodyne receivers

In many applications direct detection is not appropriate and conversion of the signal to a lower frequency, where further processing takes place, is required. A heterodyne receiver shifts the frequency of the input band by mixing the input signal with a coherent local oscillator (LO) signal by using a nonlinear element which shifts frequency of the input atmospheric signal to lower frequency, called intermediate frequency (IF), i.e. the heterodyne principle. The main advantage of this frequency translation is that amplification, filtering and detection can be effectively implemented since the high-frequency signal (in the mm and sub-mm wavelength ranges) is translated into a much lower frequency range.

Since this conversion is implemented at a fixed frequency, the IF chain can be effectively designed according to the detection and analysis problems to be solved. Such a conversion process (performed by the frontend) should be realized with a minimum of distortion and extra noise in order to attain a high sensitivity of the measuring system. After sufficient amplification and adequate filtering in the IF range, spectral signal processing can be optimally performed, e.g. detection of power, amplitude and phase/frequency (Hartfuss et al., 1997).

The most practical advantage of this technique is that the signal may be divided to produce arbitrarily many copies. This is especially significant for parallel processing since such technique introduces no degradation in sensitivity. In other words, this allows analysis of an entire spectral band with many detectors, i.e. backend instruments, at once.

It is clear that the high sensitivity and resolution provided by heterodyne-observation system in the short-millimeter through far-infrared wavelengths are of especial importance whenever detailed line shape information is required (Harris, 2003).

### 1.2.3 Calibration

In Fig. 1.1, the noise signal detected by the antenna is down-converted, amplified and filtered in the receiver. Later, this noise signal is measured by a backend-spectrometer whose main function is to represent the receiver's output in some quantitative manner, such as voltage, count or deflection. The quantity is relative to the observed power of the signal.

In microwave remote sensing, the observed noise power is measured in terms of the noise temperature (antenna temperature,  $T_A$ ). In order to establish such a connection, a calibration process is needed to attain the corresponding relation between noise power and temperature (see Janssen, 1993). That means finding the power scale of the heterodyne system, i.e. a certain gain and offset (the last accounts for the power generated by the system), by which a certain value of noise power (counts) can be translated into antenna temperature units (in degrees K).

The elements composing the heterodyne system radiate power at their own physical temperature. Subsequently, the integrated elements generate a total internal noise power called the *receiver noise temperature*,  $T_R$ . Usually, this internal noise temperature, generated by the receiver system, exceeds that of the atmospheric signal. By the same token, the noise temperature reaching the backend instrument consists of two constituents: a) the atmospheric signal detected by the antenna ( $T_A$ ), and b) the characteristic noise generated by the internal components in the receiver ( $T_R$ ). These two constituents form the *system temperature*,

$$T_S = T_A + T_R. \quad (1.8)$$

The calibration process can be implemented by observing two blackbody emitters at two different temperatures, the so-called hot  $T_H$  and cold  $T_C$  matched resistive loads (Fig. 1.2). In practice, the noise temperatures  $T_H$  and  $T_C$  are produced by well known microwave absorbers at different temperatures; for instance, at ambient temperature for the hot load ( $T_H \cong 293$  K or 20 °C) and at the temperature of liquid nitrogen ( $T_L \cong 78$  K or -195 °C) or liquid helium ( $T_L \cong 4.2$  K) for the cold load (Rohlf's and Wilson, 2004). For further details about the determination of  $T_A$  and  $T_R$ , the reader is referred to Appendix A.

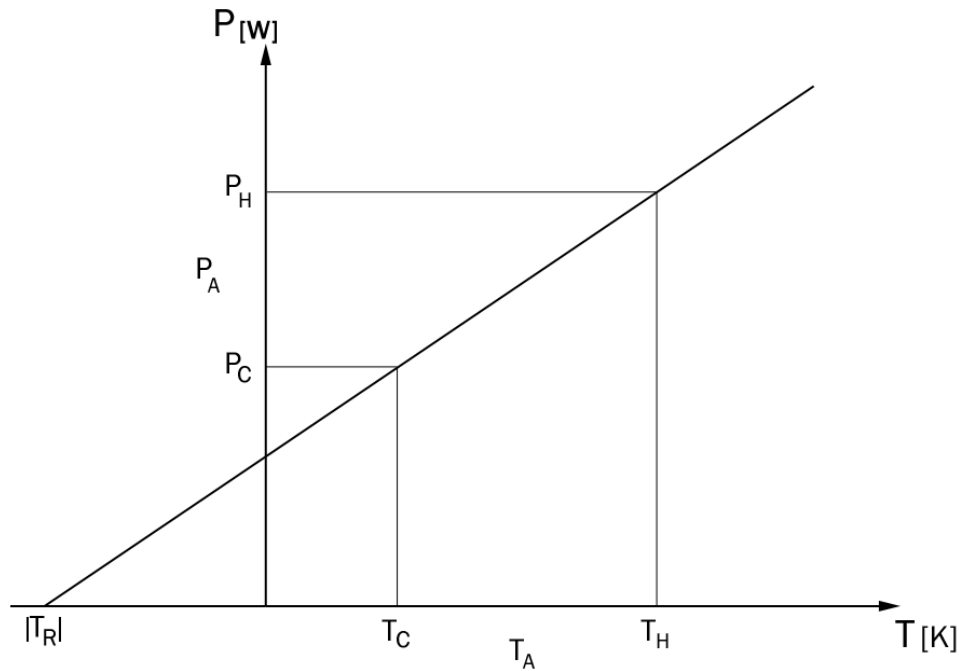


Figure 1.2: Calibration of antenna temperature using two blackbody emitters (the hot and cold loads).

Considering the radiometer as a *linear* power measuring device, the antenna temperature,  $T_A$ , is defined as

$$T_A = \frac{P_A - P_C}{P_H - P_C}(T_H - T_C) + T_C, \quad (1.9)$$

where  $P$  is power and the subscripts, H and C, imply hot and cold loads respectively (ref. Eq. A.2). Furthermore, the system-gain factor is

$$g = \frac{P_H - P_C}{T_H - T_C}. \quad (1.10)$$

#### 1.2.4 The radiometer formula

In radiometric terminology, the radiometric sensitivity (or radiometer noise formula)  $\Delta T$  is defined as the smallest change in  $T_A$  that can be detected by the radiometer output (Janssen, 1993). A more formal definition says that any measurement of noise power possesses an inherent statistical uncertainty that depends on the bandwidth  $B$  of the noise power and on the time  $\tau$  allowed for its measurement, which is given by

$$\Delta T = K \frac{T_S}{\sqrt{B\tau}}. \quad (1.11)$$

The above equation defines the radiometric sensitivity (or resolution) of a total power radiometer with no gain fluctuations (Ulaby et al., 1981). According to Janssen (1993), the total power radiometer is not well suited for many applications because it is difficult to

Table 1.1: Sensitivity constants  $K$  of different receiver configurations

Receiver type	$K$
Total-power receiver	1
Dicke or switched receiver	2
Graham's receiver	$\sqrt{2}$
Correlation receiver	$\sqrt{2}$
Adding receiver	$\frac{1}{2}$
Correlation interferometer (2 dishes)	$\frac{1}{\sqrt{2}}$
1-bit digital AC spectrometer	2.21
2-bit digital AC spectrometer	1.58

stabilize and calibrate. Since an ideal system with no gain is difficult to achieve in practice, a receiver configuration needs to be calibrated (i.e. a differential compensation principle). But, these configurations introduce a higher uncertainty in the temperature resolution of the instrument, the sensitivity constant  $K$ . This constant  $K$ , as shown in Table 1.1, defines the noise performances of different receiver configurations (cf. Rohlfs and Wilson, 2004, Kraus, 1986).

### 1.2.5 Scientific applications

Situated between the radio and infrared wavelengths of the electromagnetic spectrum, the microwave region extends from about a few GHz to 3 THz and beyond. Nevertheless, there is no clear approval of an exact range (especially in the upper frequency limit which may be considered of instrumental nature). Normally, applications involving the microwave region occur at the centimeter, millimeter and submillimeter wavelength ranges (Fig. 1.3).

The analysis of atmospheric constituents yields the physical qualities of an atmosphere whose characteristics can be acquainted with observational techniques. One important type of observational technique is that of microwave remote sensing, which depends on the detection of electromagnetic radiation emitted, scattered or absorbed by the atmosphere. For example, the knowledge of physical phenomena such as global temperature change, the Antarctic ozone depletion and global depletion of ozone or the day-night variation of ozone in the Earth's atmosphere may be attained by long-term measurements by means of microwave remote sensing of the ozone abundance through its fairly strong line emission. Molecules such as water vapor play a major role in mesospheric ozone photochemistry, where minimum water mixing ratios are observed in winter and maximum values in summer, for instance in the appearance of noctilucent clouds (NLC) in northern Europe (see Seele and Hartogh, 1999, von Zahn et al., 2004). Additionally, nonresonant pressure-induced absorption by  $\text{CO}_2$  constitutes the governing factor for most absorption in the deep atmosphere of Venus, and the inversion band of  $\text{NH}_3$  (centered around 24 GHz) is the major absorber in the deep atmospheres of the outer planets.

The high spectral resolution achieved by heterodyne (coherent) systems offers detailed and highly accurate information in the study of emission (or absorption) lines in planetary atmospheres. For instance, unique investigations of the upper atmospheres of the Earth,

Molecular Absorptions:

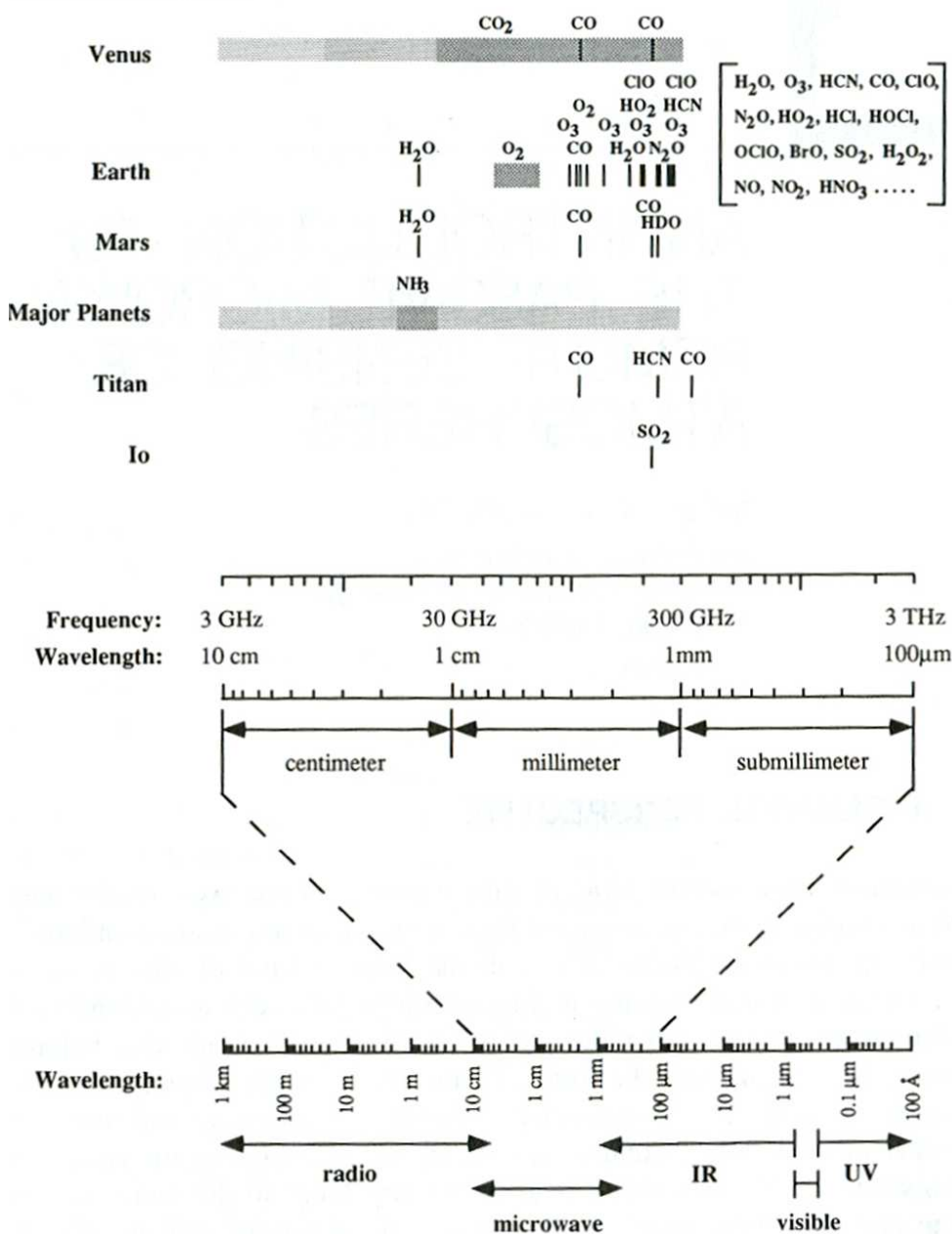


Figure 1.3: The microwave region spans at least two, arguably three, decades between the radio and infrared regions of the electromagnetic spectrum. Gases responsible for absorption in the atmospheres of the Earth and the planets are indicated, from Janssen (1993).

Venus, Mars and the Giant planets (including some of their moons) have been possible owing to high-resolution measurements of the millimeter lines of the minor constituents (Janssen, 1993). Furthermore, the development of the submillimeter region is actually opening new vistas not only in planetary studies but also of minor bodies such as comets (e.g. see Hofstadter et al., 1999, Küppers et al., 2006, Drahus et al., 2007).

### 1.3 Aims of this thesis

The current development of spectrometers for application in microwave heterodyne spectroscopy is predominately focused on achieving a wide bandwidth and high spectral resolution, whereas little is mentioned about accuracy of the power spectral density of their data. It has been noticed that small differences may appear while several backend instruments are observing a particular molecule, like ozone in the Earth, using the same heterodyne frontend. Retrieval simulations demonstrate that such small deviations in the accuracy of the power density of the spectral line might produce significant changes in the retrieved volume mixing ratio. Also, numerical analyses show, in general, that some measurements require signal-to-noise ratios larger than 1000, i.e., that the power spectral density is known with an accuracy of better than 0.1%. Such deviations in the power spectral density are likely to be created by nonlinearity in microwave devices.

Traditional methods for linearity measurement in similar applications hardly achieve an uncertainty lower than 1 to 2% because of instabilities in step attenuators and power sensors. Based on these, similar techniques are applied in order to analyze regions where the instrument behaves linearly. In the past, such ranges were attained by injecting a noise source at the CTS input and, by producing variable 1-dB attenuation steps in a 60-dB dynamic range, procure deviations of  $\pm 0.1$  and  $\pm 1$  dB after performing a linear fit of the spectrometer's response (see Villanueva et al., 2006a, Paganini and Hartogh, 2006). Unfortunately, the lack of accuracy and sensitivity due to the 1 to 2% uncertainty of these methods, it is difficult to discern whether these differences in the volume mixing ratio are a consequence of nonlinearity. Therefore, a different approach is required in order to determine deviations from linearity with the expected accuracy.

This thesis further presents the experimental study of nonlinear behavior affecting components in the new chirp transform spectrometer. As commented in the preceding discussion, nonlinearities are likely to be responsible for phenomena that might degrade the heterodyne system's performance and thus must be minimized.

The rest of the thesis is structured as follows. Chapter 2 contains the design, characterization and testing of the new chirp transform spectrometer, where special emphasis is placed on the characterization measurements of the design parameters. This is followed by the presentation of some practical applications of the CTS, namely the detection of ozone in the Earth's atmosphere and astronomical observations of comet 73P/Schwassmann-Wachmann 3 and other bodies.

Chapter 3 reviews the basic concepts for retrieving vertical profiles from the spectra arising from planetary atmospheres. These are helpful for a subsequent simulation setup. In addition, the physical properties of the Earth's atmosphere are presented. In order to explain the shape of the spectral line, it is also necessary to describe the well known absorption and emission processes of gases. This leads to the theory of radiative transfer,

which describes the intensity of radiation propagating in a general class of media, and the inversion technique, which is useful for the vertical profile retrieval. In the following sections, a numerical calculation demonstrates how considerable the effects are in the measured spectra in case of deviation from the ideal spectrometer's linear dynamic range. Later, a simulation study shows how such deviation in the spectra can produce significant changes in the retrieved vertical profile.

Finally, two novel experiments were designed and conducted such that the nonlinear behavior of the spectrometer could be identified and analyzed. All the results from these two experiments and their improvements on the spectrometer system are presented in detail in Chapter 4.



## 2 The 400-MHz bandwidth CTS

A CTS with a larger bandwidth, of 400 MHz, and a spectral resolution of 100 kHz has been developed. It bears some new technical developments which are described in this chapter. As in the case of the SOFIA-GREAT CTS it uses digital techniques to perform the chirp signal generation. For the 400-MHz bandwidth CTS, a newly developed DDS board, driven by a 1-GHz fixed frequency clock source, creates a chirp signal with 400 MHz bandwidth. The RF processing of the analog chirp signal involves a completely new design. The preprocessing unit (the ASIC board), based on a Complementary Metal Oxide Semiconductor (CMOS) and an Application-Specific Integrated Circuit (ASIC), is similar as the one used for the SOFIA-GREAT CTS. A build-in PC104 computer handles the process control and the external communication via ethernet and a Transistor-Transistor Logic (TTL) interface. The CTS was applied in atmospheric science, i.e., a 142-GHz ozone system. In addition, astronomical observations were performed using the Heinrich Hertz Submillimeter Telescope.

This chapter is organized as follows. Section 2.1 reviews the functional principle of chirp transform spectrometers and its recent progress and applications. Following on, Section 2.2 explains the theoretical framework of the Chirp transform and its application in power-spectral measurements. In Section 2.3, the description and design of the spectrometer is presented. Later, the instrument's characterization is described in Section 2.4, i.e., the digitally-created chirp signal analysis, spectral resolution, dynamic range, nonlinearity of the frequency scale and the overall stability. Section 2.5 is devoted to the results of observation test measurements. Next, Section 2.6 discusses the improvements and performance enhancement in the new CTS. Finally, the outlook for future developments is presented in Section 2.7.

### 2.1 Introduction to CTSs

As mentioned before, heterodyne spectroscopy is a technique providing practically unlimited spectral resolution. This is specially important for instance in the study of planetary atmospheres where the structure of molecular transition lines gives detailed information about molecular distribution, temperature and pressure profiles as a function of altitude (Hartogh, 2004) or for instance outgassing features in case of comets (Gulkis et al., 2007). In atmospheric spectroscopy or radioastronomy the down-converted signals are in general of stochastic nature. As a consequence, the derived power spectra are stochastic as well and require averaging.

The spectral analysis method requires a high efficiency or high duty cycle. Spectrometers with nearly 100% duty cycle are called real-time spectrometers since the a priori data

rate of the calculated spectrum is the same as the incoming time domain signal. Reduction of the data rate is done by averaging of power spectra. Real-time or nearly real-time spectrometers such as Filter Banks (FB), Acousto-Optical Spectrometers (AOS), Auto-correlators are widely spread especially in radioastronomy (see Harris, 2002, Harris et al., 1998). In addition, high-bandwidth Fast Fourier Transform Spectrometers (FFTS) have been developed (for further details see Benz et al., 2005, Klein et al., 2006).

The chirp transform spectrometer has a successful history of more than two decades in ground-based, airborne and space missions. The first millimeter-wave heterodyne spectroscopy with a CTS was performed in the middle of the 1980s by detecting the 142-GHz rotational transition of ozone in the Earth's middle atmosphere (Hartogh, 1989, Hartogh and Hartmann, 1990, Hartogh and Jarchow, 1995). Since the early 1990s, there exist continuous ground-based measurements of water vapor (22/183 GHz) and ozone (142 GHz). Furthermore, a wide range of topics of modern astrophysics has been addressed upon the integration of a CTS spectrometer into the Heinrich Hertz Submillimeter Telescope on the Mt. Graham in Arizona, USA (Hofstadter et al., 1999). These topics go from questions about comets, planetary atmospheres and the interstellar medium in the galaxy to investigations related to the early Universe. Lately, a CTS (from MPS) provided high-quality spectra of comet 2002 T7 (LINEAR) and the Earth from the Microwave Instrument for the Rosetta Orbiter on-board the Rosetta Mission, the first deep space mission carrying a submillimeter heterodyne spectrometer (Beaudin et al., 1998, Gulkis et al., 2007).

The CTS has been proven to be a reliable and accurate spectrometer (for instance in Seele and Hartogh, 1999, Hartogh et al., 2004). As stated earlier, the newly developed 400-MHz bandwidth CTS combines the advantage of broader bandwidth analysis with keeping the characteristics of previous CTSs. The new techniques applied for creating the chirp signal, which also involves similar digital techniques as used in the SOFIA-GREAT- (Stratospheric Observatory for Infrared Astronomy - German REceiver for Astronomy at THz frequencies) CTS (Villanueva and Hartogh, 2004), yield a perfect matching to the dispersive properties of the CTS's compressor unit and an improvement of the signal-to-noise ratio (SNR) up to 50 dB (Paganini and Hartogh, 2006).

The CTS is based on the Chirp transform (Klauder et al., 1960, Darlington, 1964, Mertz, 1965), an algorithm derived from the Fourier transform and implemented by linear frequency-modulated waveforms and their matched filters. In the CTS, the input signal is first multiplied with a chirp (called expander). Thereby, a fixed frequency signal for instance becomes linearly modulated. The latter signal is fed into a linear dispersive delay line (a matched filter, also called compressor) with a delay time depending on frequency and equal dispersive characteristics of the initially created chirp signal but opposite slope (i.e., the transfer function is the complex conjugate of the chirp spectrum). As shown in Fig. 2.1, the filter's output for the fixed frequency looks like a single peak (in reality a sinc function) at a specific time providing the spectrum as a function of time (see Hartogh, 1989, Villanueva, 2004). The dispersive elements are Surface Acoustic Wave (SAW) filters. These filters are characterized by the propagation of acoustic energy along the surface of a piezoelectrical crystal base which selectively redirects the acoustic waves. Hence, the wave pattern of the surface acoustic wave can be modified by microstructures on the substrate surface, translating in amplitude and/or phase changes of the input signal (see Section 2.3.1 for further details).

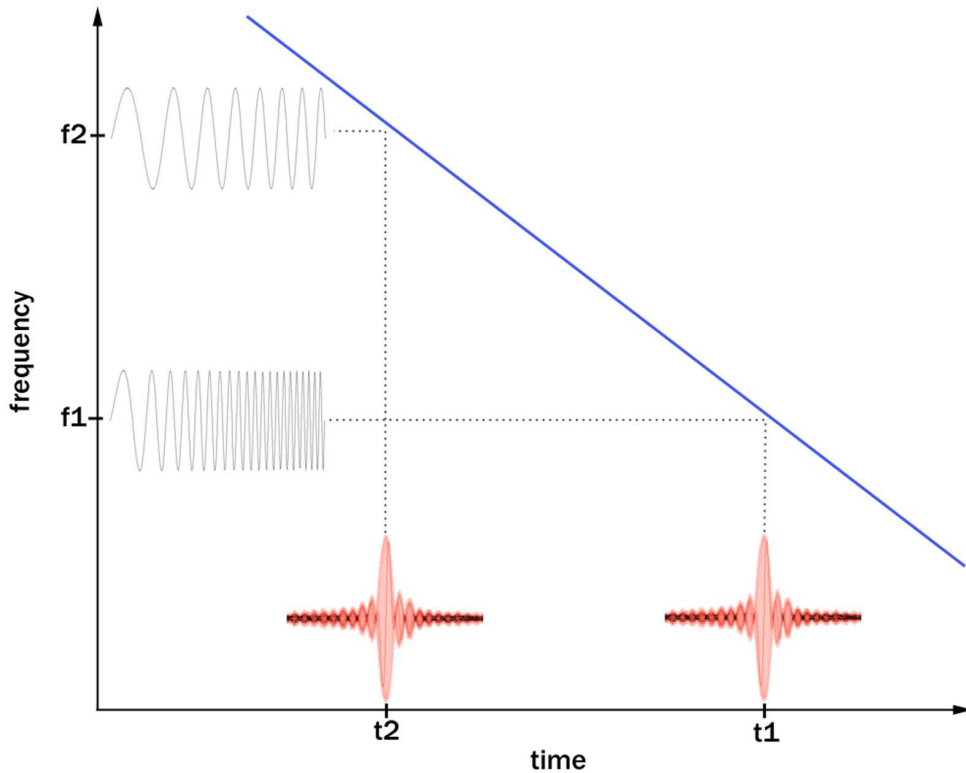


Figure 2.1: In the CTS, the input signal is first multiplied by a chirp. In case of a fixed-frequency input signal (or CW), the output of the SAW filter looks like a single peak (in reality a sinc function) at a specific time providing the spectrum as a function of time.

## 2.2 The Chirp transform principle

The Chirp transformation (CT) is a time-frequency domain transformation, the principle behind the CTS. This can be mathematically explained starting from the well-known Fourier transform equation,

$$F(\omega) = \int_{-\infty}^{+\infty} f(t)e^{-j\omega t} dt, \quad (2.1)$$

where  $\omega = 2\pi f$ .

Thereafter, assuming a linear relation: frequency  $\longleftrightarrow$  time,

$$f = \mu\tau \quad (2.2)$$

where  $\mu$  is the chirp slope, i.e., the rate at which the frequency increases or decreases with time, defined as

$$\mu \equiv \frac{\Delta f}{\Delta t} \left[ \frac{\text{MHz}}{\mu\text{s}} \right], \quad (2.3)$$

obtaining

$$F(\tau) = \int_{-\infty}^{+\infty} f(t)e^{-j2\pi\mu\tau t} dt. \quad (2.4)$$

Then, using the identity:  $2\tau t = t^2 + \tau^2 - (t - \tau)^2$ , it results in the following expressions:

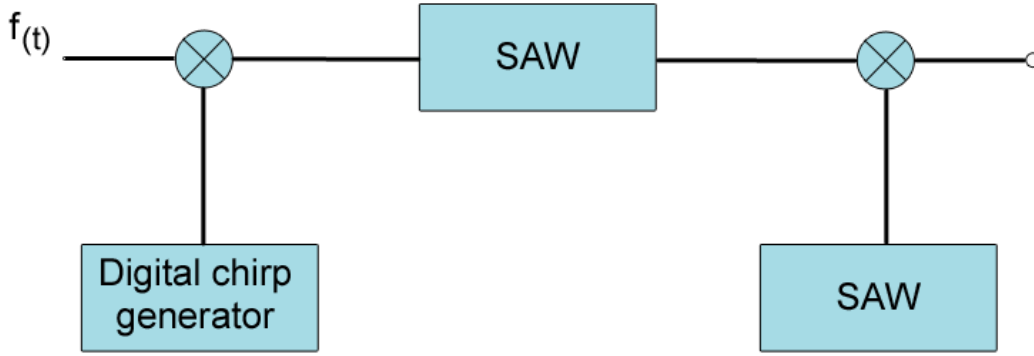


Figure 2.2: The Fourier transform can be implemented with an alternative arrangement involving multiplication and convolution with chirp waveforms.

$$F_{(\tau)} = e^{-j\pi\mu\tau^2} \int_{-\infty}^{+\infty} f_{(t)} e^{-j\pi\mu t^2} e^{-j\pi\mu(\tau-t)^2} dt \quad (2.5)$$

$$f_{(CTS)} = f_{(t)} * h_{(t)} = \int_{-\infty}^{+\infty} f_{(t)} h_{(t-\tau)} dt. \quad (2.6)$$

The last expressions indicate the interaction between two linear systems by means of the convolution: the dispersive filter ( $e^{-j\pi\mu(\tau-t)^2}$ ) and the chirp signal mixed with the incoming signal ( $f_{(t)} e^{-j\pi\mu t^2}$ ); i.e., the Fourier transform can also be realized with an alternative arrangement (Atzeni et al., 1975) involving multiplication and convolution with chirp waveforms. As can be seen in Eq. 2.5 and represented in Fig. 2.2, the expression " $e^{-j\pi\mu\tau^2}$ " denotes another SAW device which function is to recover the signal's phase. However, since only the power spectra of stochastic signals is required, the phase is lost after squaring and thus it is not implemented in the design.

It should be emphasized that Eq. 2.5 is valid if a perfect matching is considered between the dispersive characteristics of the SAW device (compressor),  $\mu_c$ , and the generated chip signal (expander),  $\mu_e$ :

$$\mu = \mu_c = \mu_e \quad (2.7)$$

Last but not least, it can be inferred that the chirp signal, a linear frequency-modulated signal, can also expressed as a quadratic phase modulated signal,

$$f_{chirp}(t) = e^{-j\pi\mu t^2}. \quad (2.8)$$

## 2.3 Development and design

As observed in Fig. 2.3, the CTS involves two parts: the analog and the digital. On the one hand, the analog part (Fig. 2.4) is integrated by the RF stages which include mixers, amplifiers, filters, doublers, splitters, and SAW filters. On the other hand, the digital part (Fig. 2.5) involves the chirp generation board (DDS board), the data processing and synchronization board (ASIC board), an ISA-ASIC (Industry Standard Architecture) interface, and an embedded PC104 computer. For detailed diagrams of the system and its RF components' characteristics, the reader is referred to Appendix B.

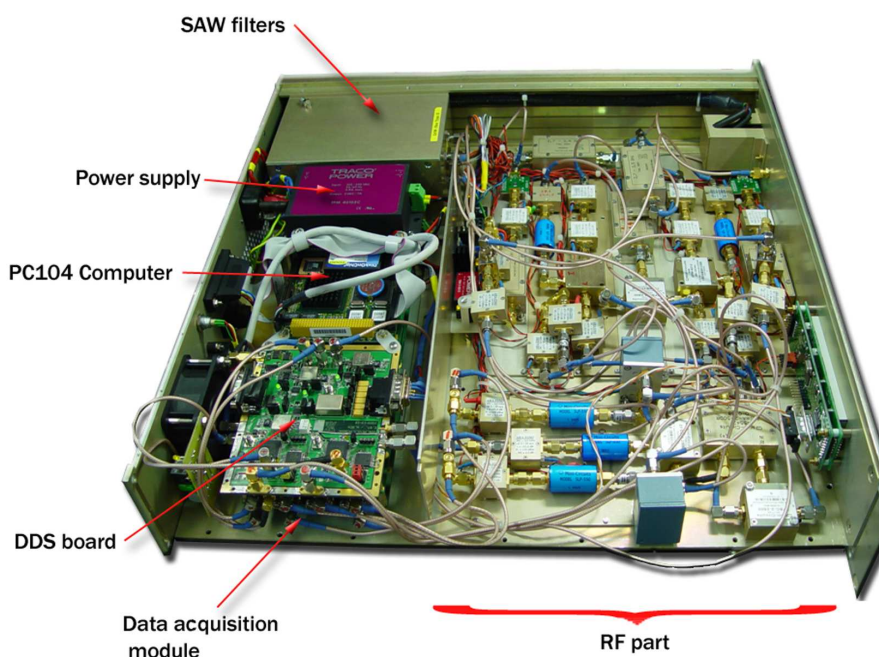


Figure 2.3: The 400-MHz bandwidth chirp transform spectrometer.

The duty of the CTS is, as a heterodyne backend system, to acquire an incoming signal (supplied by frontend systems) and then provide the spectral information in real time with 100% efficiency.

The chirp is digitally created using direct digital synthesizers (DDS) which are driven by a 1-GHz frequency clock. The importance of such technique relies in the possibility to fix every aspect of the chirp signal in order to achieve a perfect dispersive matching as required previously in Eq. 2.7. It must be stressed that any dispersive characteristic of the SAW device can be accurately matched by means of digital properties changes in the DDS board. The created chirp signal in the DDS board has a 400-MHz bandwidth centered at 250 MHz and a dispersion time of  $20 \mu\text{s}$ . The DDS device incorporates an integrated 10-bit current output DAC, wherein the amount of common-mode noise that might be present (at the DAC output) is reduced by means of differential outputs. Such arrangement offers the advantage of an increased signal-to-noise ratio (SNR) up to 50 dB.

In the SOFIA-GREAT CTS, the chirp signal is quadrature modulated and up-converted, and then the frequency is tripled (achieving a bandwidth equal to 409.6 MHz). In contrast, the chirp signal is frequency up-converted using RF mixers in the new implementation of the 400-MHz bandwidth CTS. This up-converted chirp signal is latterly doubled in the RF stage achieving an 800-MHz bandwidth (see Fig. B.1 for a detailed description of RF components and different parts involved in the 400-MHz bandwidth CTS).

After the doubling process, it follows the mixing stage where the incoming atmospheric signal is frequency modulated with the chirp signal. As a result, a linear changing

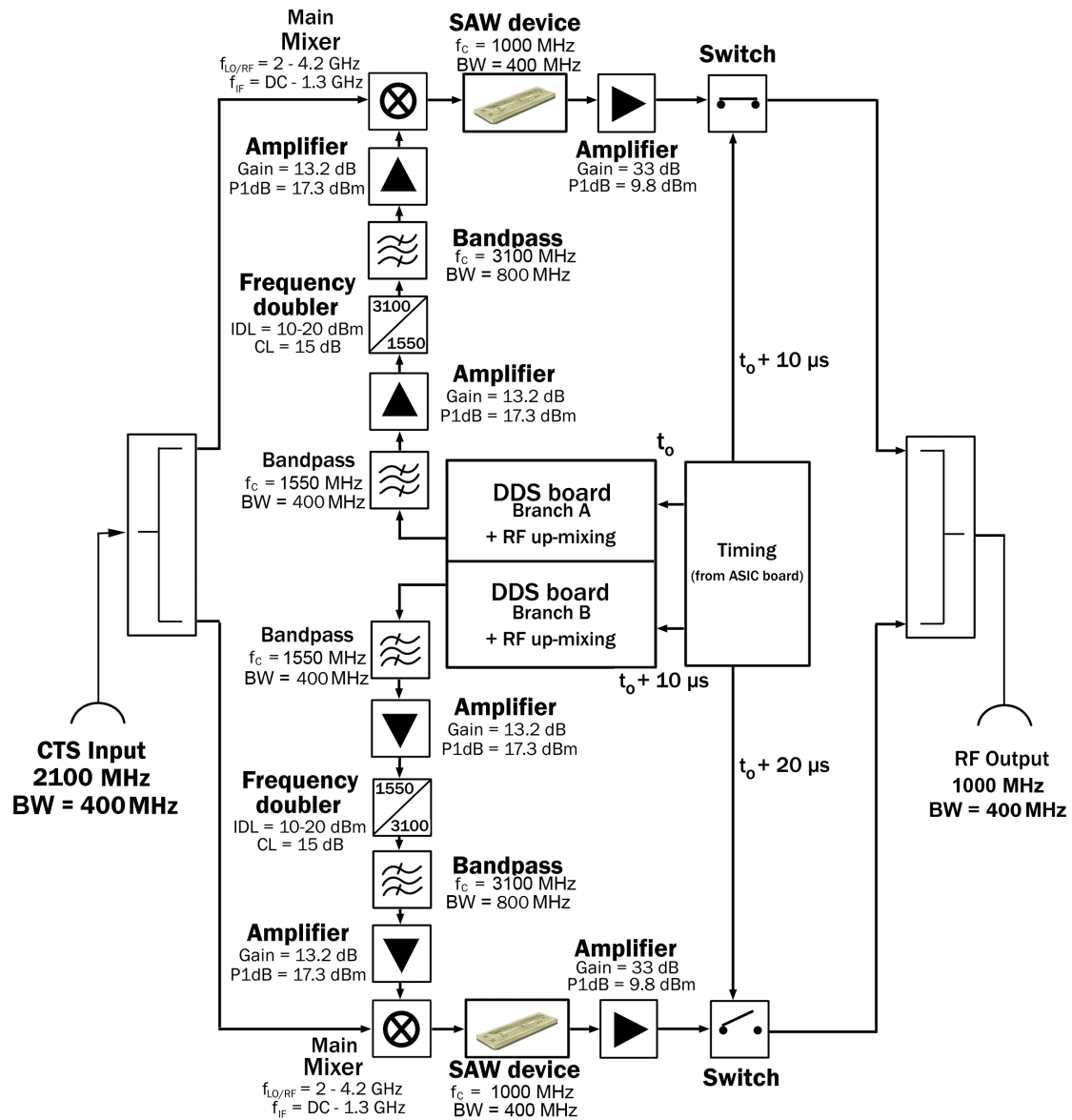


Figure 2.4: After the chirp signal is digitally created and up-converted with an RF mixer, it follows a series of filtering, amplifying and doubling processes. Then, it is modulated with the incoming atmospheric signal and consequently fed into the SAW device. After the convolution process, the resulting signal is down-converted and separated in real and imaginary part after a mixing process with a complex source (see Fig. B.1 and Table B.1 for more details). Acronyms IDL: Input Drive Level, CL: Conversion Loss, P1dB: Output Power at 1 dB Gain Compression.

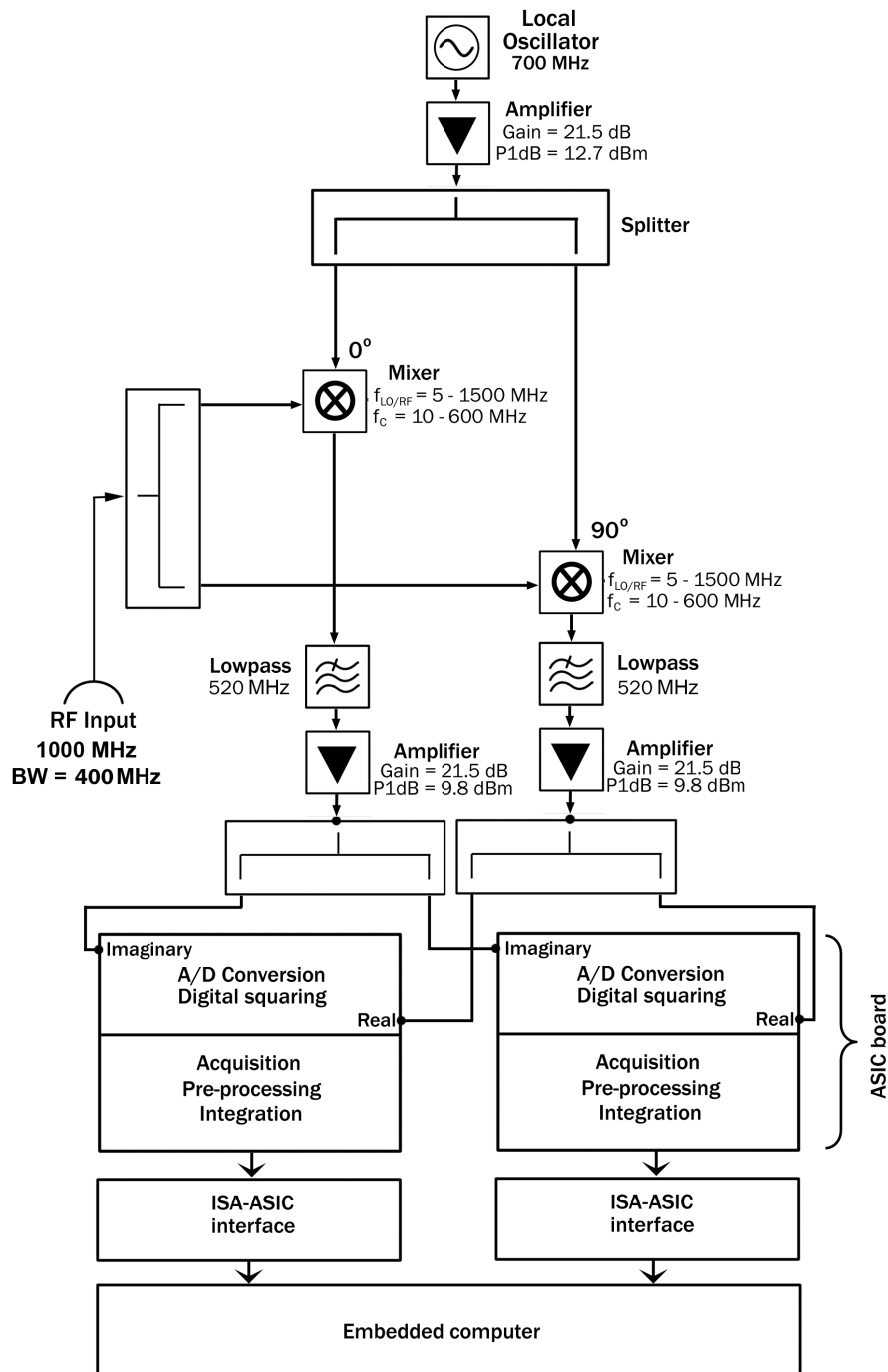


Figure 2.5: After down-conversion (see Fig. B.1 and Table B.1 for more details), in the digital part the real and imaginary signals are digitized with four pairs of ADCs where digital squaring, preprocessing and integration is performed in the ASIC board. At the end, an embedded computer provides external communication through ethernet. Acronym P1dB stands for Output Power at 1 dB Gain Compression.

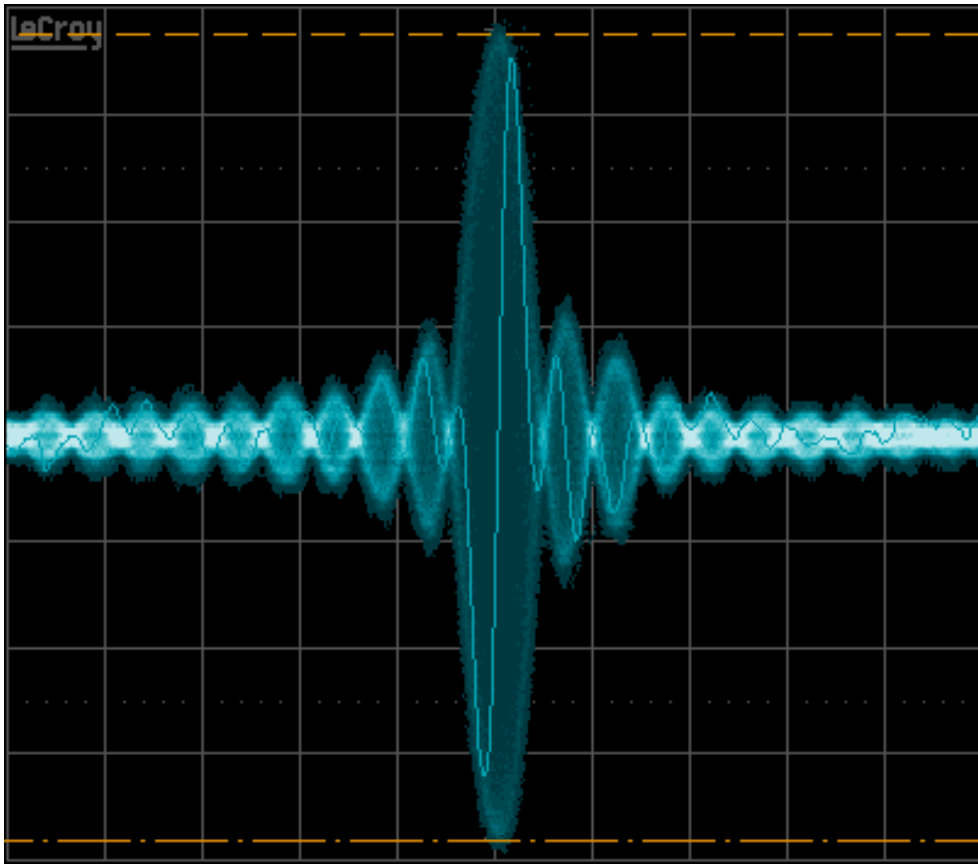


Figure 2.6: Compressed pulse observed at the end of the analog part and before the digital acquisition by an oscilloscope for a 2.1-GHz CW input.

frequency signal of 800 MHz bandwidth lies within the 600 to 1400 MHz frequency range depending on the frequency of the input atmospheric signal, which lies within the 1.9 to 2.3 GHz range. Next, the 800-MHz-bandwidth modulated signal is fed into the SAW filters which have a 400-MHz bandwidth (800-1200 MHz range). The filter's output represents the analog spectrum of the input signal in the time domain, mapped on a  $10\text{-}\mu\text{s}$  time interval (Fig. 2.6).

The duty cycle of an expander-compressor scheme is only 50% due to intrinsic properties of the chirp transform. In other words, this means that the setup takes  $20\text{ }\mu\text{s}$  to perform a transform, however, it only produces useful spectral information half of that time. For that purpose, two branches are combined through a commutator with a switching period of  $10\text{ }\mu\text{s}$  with the idea of 100% efficiency (Paganini and Hartogh, 2006, Hartogh and Hartmann, 1990).

Later on, the signal is down-converted. The real and imaginary components are obtained by mixing the signal with a complex source (Fig. 2.7). In the ASIC board, these two components are digitally acquired with a set of eight 100-MSPS, 475-MHz bandwidth analog-to-digital converters (ADC), i.e. 4 for the imaginary and 4 for the real component. The signal is digitally analyzed by an integrated preprocessor in an ASIC (Application-Specific Integrated Circuit) chip with low power consumption. This preprocessor computes the power from the complex spectrum. Here, the signal is numerically squared (real

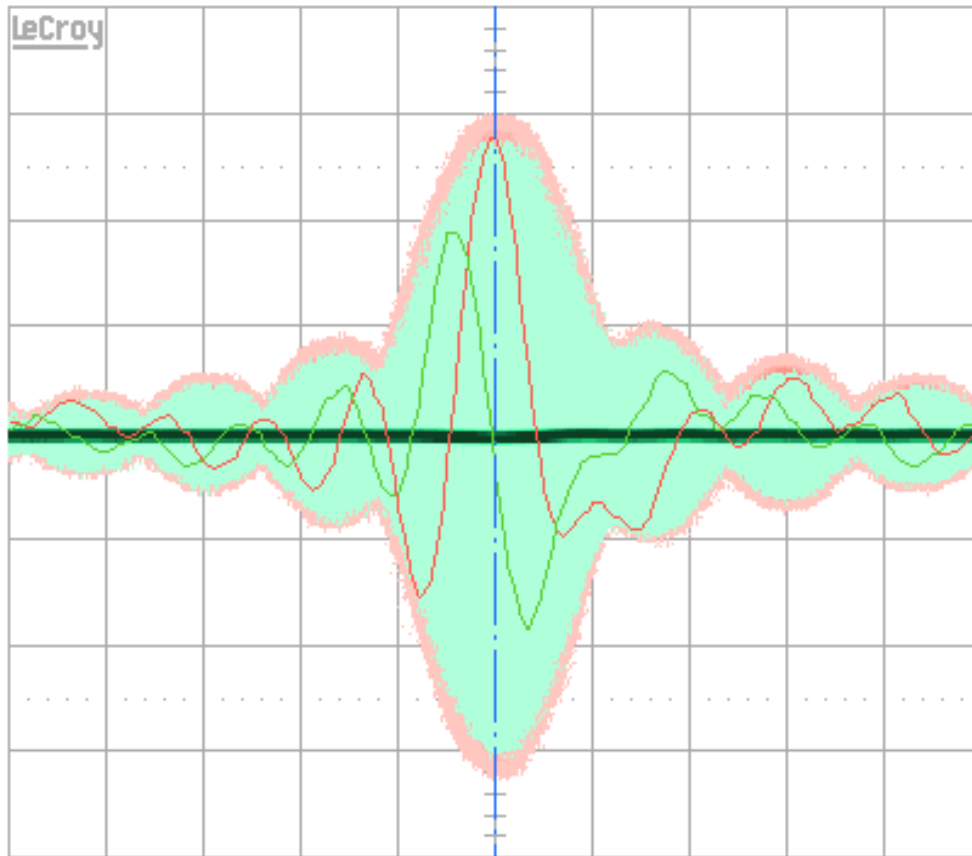


Figure 2.7: The real and imaginary components (red and green lines) are obtained by mixing the signal with a complex source.

and imaginary parts), added, and finally mapped into a 4096-channel memory where it is integrated. Furthermore, the ASIC board handles the synchronization signals needed to control the switching time of the two branches. This also involves a signal which defines the generation start of the chirp signal at a specific moment. Finally, an embedded computer provides the instrument control and external communication through an ethernet connection.

### 2.3.1 The dispersive filters

SAW dispersive or linear frequency-modulated chirp filters are key elements in the implementation of the Chirp transform in the CTS. Initially designed for use in signal processing such as pulse-compression in radar systems (Klauder et al., 1960), the main significance of the chirp-transform algorithm is that the required convolution can be efficiently performed by SAW filters (Atzeni et al., 1975). The premultiplication of an input signal  $f(t)$  with a chirp waveform followed by the convolution in a chirp filter (SAW filter) yield to the power density spectrum of that signal according with Eq. 2.5. Additionally, SAW devices are widely used in communications and industrial measurements systems, such as wireless sensors (see Reindl et al., 2001a,b, Reindl and Shrena, 2004).

In the 400-MHz bandwidth CTS, the type of chirp filters are reflective array compres-

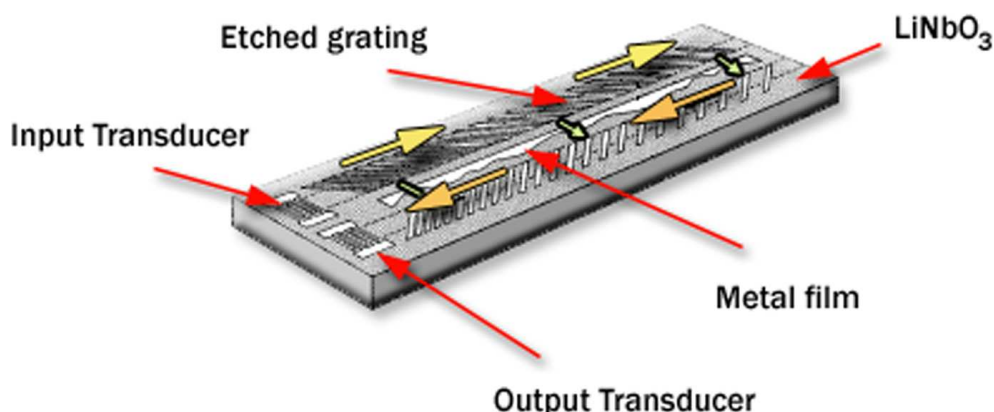


Figure 2.8: The reflective array compressor (RAC). The conversion of electric into acoustic energy is performed using inter digital electrode transducers (IDT's); however, filtering is achieved in a bank of reflective grooves where the filter amplitude response is controlled by variations in the groove depth and the frequency response by the groove separation.

sor (RAC) devices (see Williamson and Smith, 1973). In this technology the transduction, i.e., conversion of electric into acoustic energy, is performed using interdigital electrode transducers (IDTs). However, the filtering process is achieved in a bank of reflective grooves (Fig. 2.8). The surface acoustic wave, with a typical velocity of  $3 \times 10^5$  cm/s (Maines and Paige, 1976), propagates through an array of etched grooves which selectively redirect the waves on a piezoelectric substrate. For this design, the substrate is lithium niobate ( $LiNbO_3$ ). The filter amplitude response is controlled by variations in the groove depth and the frequency response is controlled by the groove separation at a point where the propagation direction matches the wavelength of the surface wave. Therefore, the surface wave propagates in a U-shaped path using two of such grooves after the input IDT. Finally, the surface wave reaches the output IDT transducer. The groove positions are established such that the surface wave travels from input to output along a path whose length is an increasing or decreasing function of frequency. Ideally, one desires zero temperature coefficient of delay, high coupling (Slobodnik, 1976) and low insertion loss (Morgan, 1998, Williamson, 1976). The advantage of RAC devices is that device phase errors can be compensated after fabrication by introducing a metallized 'phase plate' (see Jack et al., 1980, Williamson, 1976).

CTS designs employ the M(l)-C(s) (sliding) expander-compressor arrangement for the study of power spectrum in stationary signals (Hartogh and Hartmann, 1990, Villanueva and Hartogh, 2004, Paganini and Hartogh, 2006). This arrangement is characterized by a longer time duration of the premultiplying chirp signal compared to the impulse response of the convolution filter (Jack et al., 1980). Wherein, the larger time duration of the premultiplying chirp signal can be achieved for instance through frequency-multiplication techniques (Villanueva et al., 2006a). The notation used is 'M' denoting multiplication, 'C' denoting convolution, '(l)' denoting long-duration chirp and '(s)' denoting short-duration chirp.

### 2.3.2 Digital chirp generation, the DDS board

As stated earlier, the detected input signal is mixed with a chirp signal (expander) in the CTS. Such chirp signal is digitally created using direct digital synthesis (DDS) in the DDS board (see Fig. 2.9). Basically, the direct digital synthesis is a technique for using digital data processing blocks (Fig. 2.10) as a means to generate a frequency- and phase-tunable output signal referenced to, in this case, a 1-GHz fixed frequency clock source. In principle, the DDS board performs the following actions:

- Generate two chirp signals from 50 MHz to 450 MHz in a dispersion time equal to 20  $\mu$ s.
- Produce a 1000-MHz-frequency signal, which serves as the clock source for the DDS chips. Later, this signal is used to create the 200-MHz clock signal for the ASIC boards (master and slave).
- Supply local oscillator signals at two different frequencies, i.e. 700 MHz and 1300 MHz.
- After a synchronized-start initiation given by the 'master' microcontroller, provide a synchronization clock signal for the PG pulses, i.e. the DDS/ASIC synchronization (for further details see Section 2.3.6).

The maximal achieved signal's bandwidth is 400 MHz in a 20  $\mu$ s period due to Shannon's sampling theorem. This is obtained after proper suppression of undesired alias frequencies (sinc envelope), produced by zero-order-hold associated with the output circuit of the DDS (typically a DAC), in a low pass filter.

The M(1)-C(s) expander-compressor arrangement indicates that, for a 400-MHz bandwidth 10- $\mu$ s SAW filter (compressor), an 800-MHz 20- $\mu$ s expander chirp signal (with opposite dispersive slope) is required. This requirement provides a complete coverage within the 1.9-2.1 GHz frequency range of input signal and accomplish Eq. 2.7 as well. Therefore, since a 400-MHz bandwidth chirp signal is obtained from the DDS board, a doubling process is latterly needed in the RF stage.

#### 2.3.2.1 The direct digital synthesizers

A DDS is a sampling-data system. As the fundamental frequency of the DDS approaches the Nyquist frequency, the lower first image approaches the Nyquist frequency from above. As the fundamental frequency approaches the Nyquist frequency, it becomes difficult, and finally impossible, to design and construct a low-pass filter that will provide adequate attenuation for the first image frequency component. The maximum usable frequency in the fundamental range of the DDS is typically between 40% and 45% of the Nyquist frequency, depending on the reconstruction filter. With a 1-GHz REFCLK, the AD9858 is capable of producing maximum output frequencies of 450 MHz.

The frequency sweep feature is implemented through the use of a frequency accumulator. The frequency accumulator repeatedly adds a frequency incremental quantity to the current value, thereby creating new instantaneous frequency tuning words, causing the frequency generated by the DDS to change with time. The frequency increment, or step

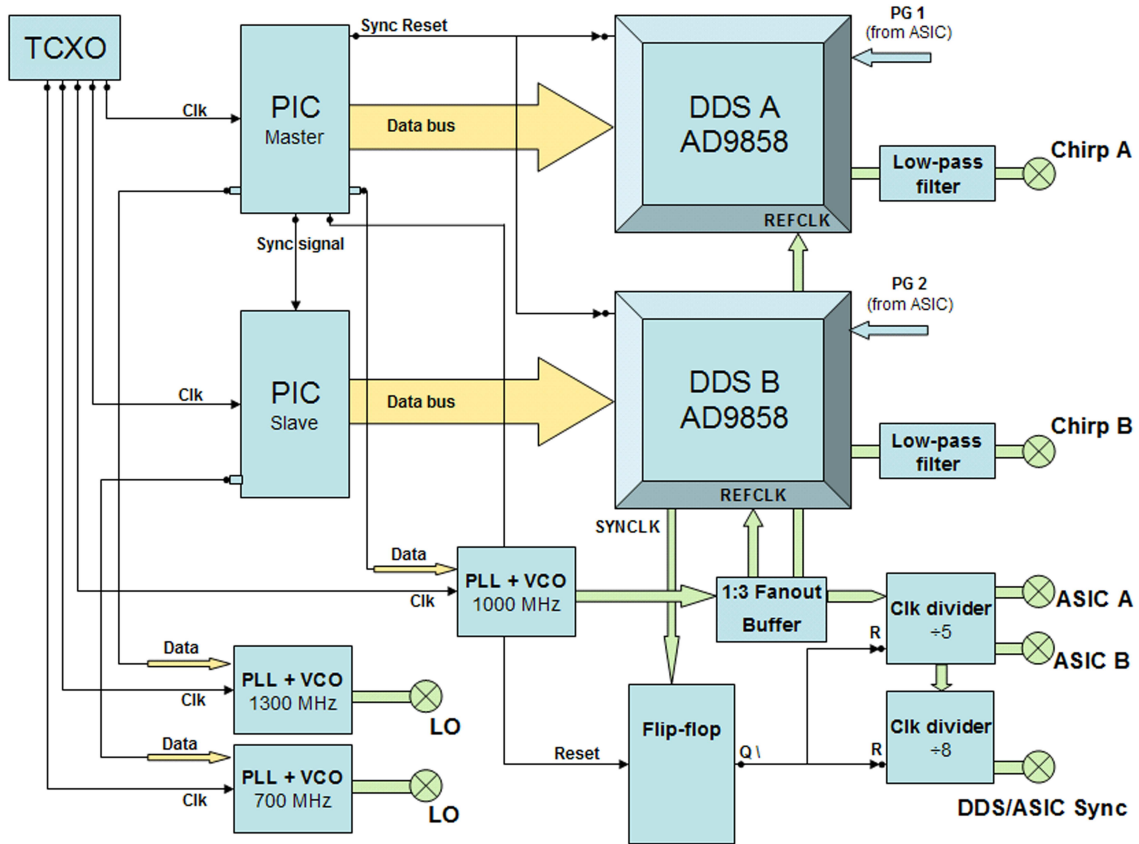


Figure 2.9: DDS-board circuit diagram.

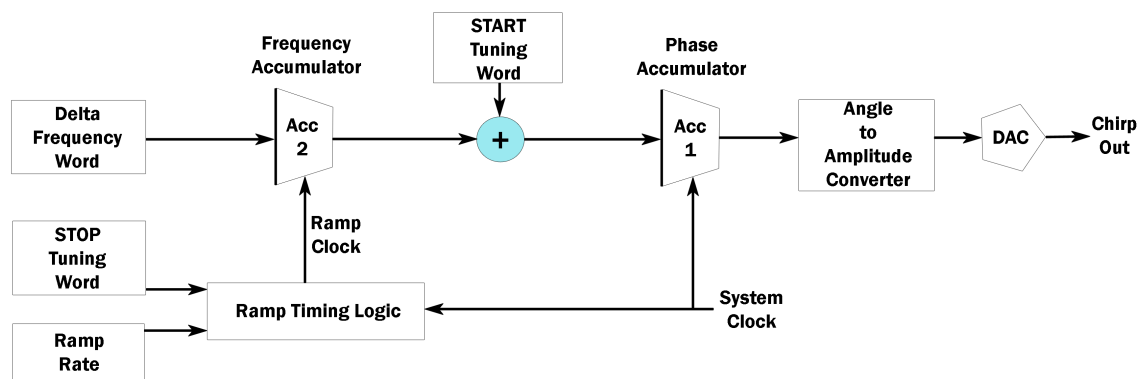


Figure 2.10: The DDS-based chirp principle: using digital data processing blocks as a means to generate a frequency- and phase-tunable output signal referenced to a 1-GHz precision clock source.

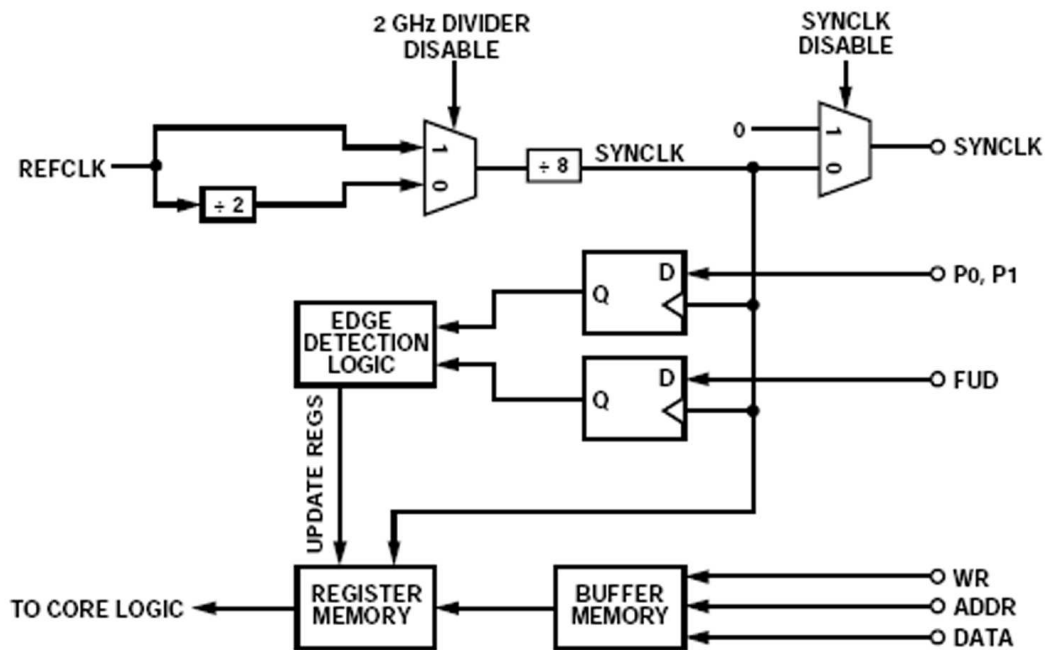


Figure 2.11: AD9858: Internal synchronization block diagram. Source: Analog Devices.

size, is loaded into a register known as the delta frequency tuning word (DFTW). The rate at which the frequency is incremented is set by another register, the delta frequency ramp rate word (DFRRW). Together these two registers enable the DDS device to sweep from a beginning frequency set by the start frequency tuning word (FTW), upwards or downwards, at a desired rate and frequency step size. The result is a linear frequency sweep or chirp (see <http://www.analog.com> for further details).

For this design, a pair of AD9858-DDS chips is programmed using programmable intelligent computers (PIC microcontrollers) in order to create the chirp signal. After start up, the microcontroller programs a phase-locked loop (PLL) chip which provides a 1-GHz reference clock to the DDS's input (REFCLK) as observed in Fig. 2.11. The device is designed for a maximum REFCLK frequency of 2 GHz (via a programmable divide-by-2 function set in the control function register CFR). The buffered REFCLK, which serves as the sample clock for the digital-to-analog converter (DAC), is fed to a divide-by-8 frequency divider to produce the SYNCLK. In principle, this enables synchronization of external hardware with the AD9858's internal DDS clock. Wherein, the external hardware which is synchronized to the internal system clock (SYNCLK) can then be used to provide the frequency update (FUD) signal to the AD9858. After the microcontroller sends the instructions to the parallel input ports of the DDS chip, the FUD signal and SYNCLK are used to transfer the internal buffer register contents into the memory registers of the device (Fig. 2.12 shows an I/O synchronization timing diagram). As a result, the DDS creates a chirp signal from 50 MHz to 450 MHz in a 20- $\mu$ s period shortly after the FUD signal is provided by the ASIC board.

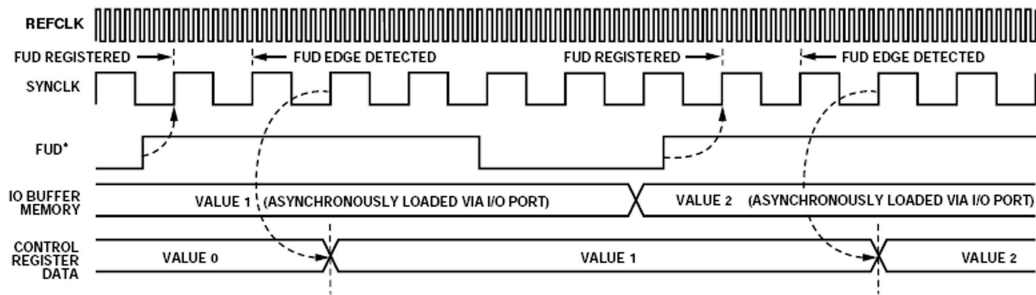


Figure 2.12: AD9858 programming: Timing diagram. Source: Analog Devices.

### 2.3.3 Time synchronization

In the following, the specific timing issues involved in the CTS electronics are described. As mentioned before, two branches are combined through a commutator with a switching period of  $10\ \mu\text{s}$  with the idea of 100% efficiency in the CTS. This procedure comprises an extra constraint: the digital chirp-signal creation and the digital acquisition part (ASIC board) must be perfectly synchronized in order to avoid phase ambiguities during the commutation process. Such synchronization defines one of the most critical issues since the spectral information spans in the time domain; hence, an unmatched synchronization would lead to erratic results such as jitter. This time synchronization is performed by a complex arrangement of the ASIC board together with the DDS board. Both boards share the same 1-GHz frequency reference clock, i.e., the REFCLK (from the PLL chip in the DDS board).

After digitization by means of ADCs in the ASIC board, the signal is analyzed by a set of two ASIC integrated-preprocessor chips working in tandem. These preprocessors compute the power from the complex spectrum; i.e., these ASIC chips square numerically the signal (real and imaginary parts), add, and finally map them into a 4096-channel memory where the power spectrum is latterly integrated. The ASIC chip is the same one for the SOFIA-GREAT CTS; in this development, however, each ASIC uses 2048 channels. Therefore, an ASIC needs a 200-MHz frequency driving clock to oversample the analog 400-MHz bandwidth, 100-kHz resolution signal (this clock frequency is supplied from the fifth order of the REFCLK). In other words, two ASIC chip possess 4096 channels with 97-kHz channel sampling resolution per channel.

At this point, the so-called PG pulses (provided by the ASIC board) control the synchronous initiation of the digitally-created chirp signals in the DDS board (FUD signal) since both (ASIC and DDS) boards have the same clock source, i.e., the PLL's REFCLK.

Summarizing, the ASIC board is in charge of the synchronization by providing the PG (i.e. FUD) pulses to the DDS chips and the  $10\text{-}\mu\text{s}$  commutation pulse in the RF part.

### 2.3.4 Operating multiple AD9858s instances

The previous section has broadly described the issues and various time setting techniques for a correct synchronous operation. Nevertheless, an atypical behavior occurred during laboratory tests over the finally assembled 400-MHz-BW CTS unit. Unexpectedly, jittering was observed after injecting a 2.1-GHz central frequency (CW) pulse. This test

derived to a complete check in the clock quality and controlling pulses provided by the DDS and ASIC boards. However, the problem was produced by a glitch in the DDS chips. In contrast with previous DDS designs, the AD9858-DDS chip possesses no capability to work in parallel with another DDS chip (Analog, priv. comm.).

As observed in Fig. 2.11, the REFCLK's divide-by-2 output state contains no controlling reset signal, thus this introduces a potential phase ambiguity. This situation leads to jittering among the internal system clocks (SYNCLK) of multiple devices.

### 2.3.5 Recommendation on parallel AD9858s architecture

To successfully synchronize multiple instances of the AD9858 DDS, one must first bypass the REFCLK divide-by-2 feature. Unfortunately, this is not as simple as disabling the REFCLK divider bit in register 00 hex. This is because the REFCLK divider's state machine does not get initialized by any control signal (e.g., MASTER RESET). As a result, the output of the divider introduces a potential phase ambiguity of one-half REFCLK cycle. This leads to phase differences among the internal system clocks of multiple devices, which can either be in phase or 180° out of phase relative to one another. Following, there are some actions performed by a microcontroller in order to work around this limitation.

#### 2.3.5.1 Bypassing the REFCLK divide-by-2

The device can be placed into a factory test mode which disables the divide-by-2 at start-up, or upon MASTER RESET. Setting this test mode does not inhibit any other feature. The device will function as normal, except for disabling the divide-by-2 feature. The test mode requires that pins 25 and 28 are connected to VCC, and pins 23,24,26,27 to ground. This will bypass the REFCLK divider immediately, while still supplying a SYNCLK at 1/8th the REFCLK frequency.

#### 2.3.5.2 Synchronizing SYNCLK among all DDSs

In order to achieve SYNCLK alignment among multiple AD9858s, the REFCLK must be coincident at all of the DDSs. Any timing skew among rising edges of REFCLK may result in SYNCLK and DAC output misalignment among the DDSs. Next, there needs to be a constraint imposed on the relationship between the MASTER RESET and the REFCLK. They must be synchronous, and the falling edge of MASTER RESET needs to occur outside of an interval of  $\pm 200$  ps surrounding the rising edge of REFCLK. In other words, the falling edge of MASTER RESET should not occur within 200 ps of the rising edge of REFCLK, either before or after. This is accomplished by the 'master' microcontroller. This constraint is due to the SYNCLK being derived from REFCLK through a divide-by-8 stage. When the MASTER RESET is high, the divide-by-8 is initialized to a known state. When the MASTER RESET is released, the divide-by-8 starts. It is necessary for the falling edge of MASTER RESET to occur simultaneously at all DDSs, while meeting the keep-out time specified above.

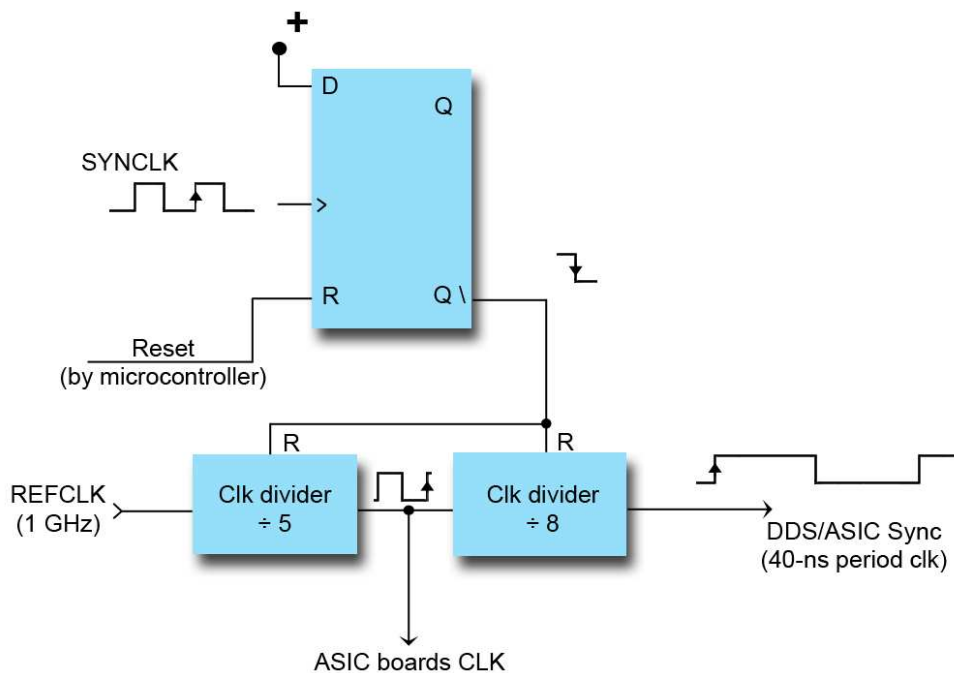


Figure 2.13: Synchronizing the DDS and ASIC boards: a 40-ns period clock was created in order to produce PG pulses synchronized with the SYNCLK.

### 2.3.5.3 Meeting setup and hold times between FUD and SYNCLK

Finally, the FUD pulse is sent simultaneously to all DDSs. FUD is the clock that transfers the data from the I/O port buffers to the programming registers, making the data active. The rising edge of FUD must meet a minimum setup time of 4 ns before the rising edge of SYNCLK. The minimum hold time should be one SYNCLK period after the rising edge of SYNCLK.

### 2.3.6 The DDS and ASIC boards synchronization

As previously mentioned, the fact that the AD9858 is driven by the SYNCLK means that the PG pulses (provided by the ASIC board) must perfectly match the SYNCLK instead of REFCLK (the latter is the case for the SOFIA-GREAT-CTS design). However, the ASIC board is operated by a 5-ns clock period (i.e.,  $\frac{1}{200\text{MHz}}$ ) and, on the other side, the SYNCLK consist of an 8-ns period one (i.e.,  $\frac{1}{125\text{MHz}}$ ) in the DDS board. This implies a new limitation since both clock periods may occasionally produce initiation at different phase instants and thus asynchronous PG pulses supplied to the DDS board (FUD).

As shown in Fig. 2.13, the solution can be attained by synchronizing the generation of PG pulses with the SYNCLK through a flip-flop device. In order to implement that, the SYNCLK serves as clock source for the flip-flop circuit which is reset by a microcontroller. As a result, the 'Q\'' port provides a synchronous reset pulse for two dividers: the first one generates the ASIC board's clock (divide-by-5 device); and the second, a divide-by-8 device, creates a 40-ns period clock source. The last yields PG pulses and SYNCLK without phase ambiguities.

## 2.4 Characterization. Test measurements

In Astronomy, the performance of an instrument is described by different standard analyses and tests, usually under laboratory conditions. This is the so-called *characterization* of the instrument. To accomplish the characterization of the 400-MHz BW CTS, novel and standard test analysis were performed. In this section, the characterization tests include: test of the chirp signal, frequency- and time-domain analyses, stability (i.e. the Allan-variance test), spectral resolution, and the power linearity and dynamic range (deviation from linearity of  $\pm 1$  and  $\pm 0.1$  dB in both the digital and analog parts). A summary of these results and other important characteristics of the instrument are presented in Table 4.2 at the end of this section.

### 2.4.1 Analysis of the chirp signal

It is especially important to understand the behavior of the digitally-created chirp signal. The quality requirements for this signal are: a) a small passband ripple, b) a good signal-to-noise ratio (SNR), c) small phase deviation, and d) the knowledge of both group delay and chirp rate ( $\mu$ ).

Different chirp-signal analysis methods are applied in order to calculate the previously mentioned quality factors after acquiring and digitizing the chirp signal (using a digital storage oscilloscope, DSO). Namely, this denotes: the calculated magnitude, the wrapped phase and fitting at a desired frequency range, phase deviation and root-mean-square error, and the chirp rate. Figure 2.14 displays the results after applying these analysis methods over a synthetic perfect chirp signal. In contrast to the ideal reference, Fig. 2.15 indicates the real case offered by the DDS board's output.

Most of these methods, based on Fourier transforms, analyze the acquired signal in a stationary regime. This can be explained by the fact that the Fourier transform equation takes as limits of its integral infinite boundaries ( $F(\omega) = \int_{-\infty}^{+\infty} f(t) e^{-j\omega t} dt$ ); therefore, it is not possible to distinguish separately which events occur at a specific time. However, the chirp signal is a non-stationary wave; i.e., it changes with time.

The analysis of this kind of waveform can be conducted by a novel Short-Term Fourier Transform (STFT) analysis method (cf. Narasimhan and Pavanalatha, 2004). Among others, the STFT yields to calculate the Fourier transform at small time intervals, thus allowing the chance to discriminate events at defined time slots (Kramer and Jones, 1994, Allen, 1977, Allen and Rabiner, 1977). In Fig. 2.16, the first plot (a) shows the applied method over a simulated perfect chirp signal. On the other hand, the second one (b) suggests that created harmonics in the real case may slightly produce deviations from the theoretically expected results.

The aim is to analyze frequency components in the time domain. This analysis tool can be methodologically implemented at different RF stages between the DDS board's output and the SAW device's input. Hence, the plan is to determine whether harmonics observed in a spectrum analyzer are influencing the 20- $\mu$ s transformation interval or not. If that is the case, unwanted noise is added because of chirp signal deterioration. This is especially important during the instrument design process while different RF devices are being evaluated. Thereby, it is possible to estimate if the influence of undesired harmonics could be neglected or should be suppressed; e.g., through the addition of filters. For

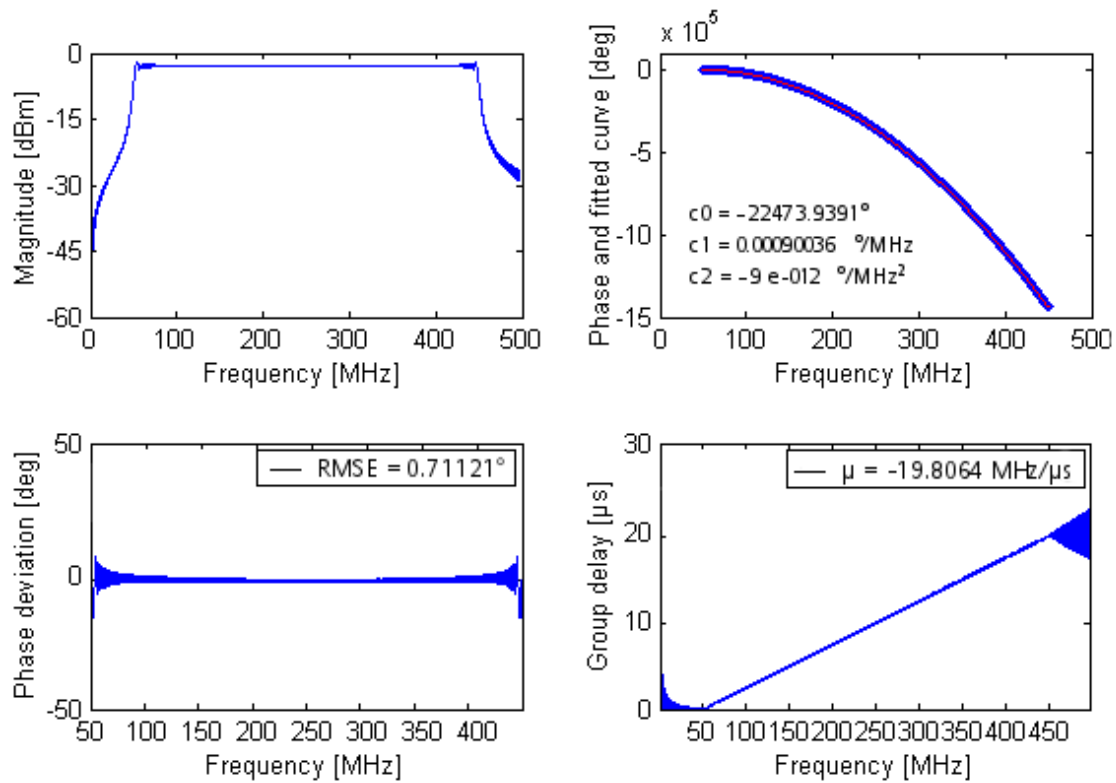


Figure 2.14: Chirp-signal analysis tools: simulated perfect chirp signal. *Upper left*: Calculated magnitude. *Upper right*: Wrapped phase and fitting in the desired frequency range. *Bottom left*: phase deviation and root mean square error. *Bottom right*: Calculation of the chirp rate.

instance, the third plot (c) displays the signal fed into the SAW filter where deterioration is observed after a specific stage involving mixing, amplifying and doubling processes. As stated earlier, it is clear that such anomalies imply undesirable harmonics which diminish the overall instrument performance, such as added system noise.

It must be stressed that this method yields the identification of harmonics and, consequently, the chance to implement suppression techniques. A real case scenario, in order to improve the chirp signal quality (from Fig. 2.16-c) was the addition of filters and the replacement of the RF mixer before the doubling process (for one with better isolation properties).

## 2.4.2 Frequency and time domain analyses

In the last section, the quality of the chirp signal was analyzed and improved according to a stage-by-stage analysis along the RF sections of the CTS. In this section, another important stage-by-stage analysis is described as an extensive examination of the instrument's response. The objective of this analysis is to observe both frequency- and time-domain by means of a spectrum analyzer and a DSO respectively.

The principle of the instrument is based on a frequency-time dependence as that given by the Fourier transform equation and theoretically explained in Section 2.2. Wherein,

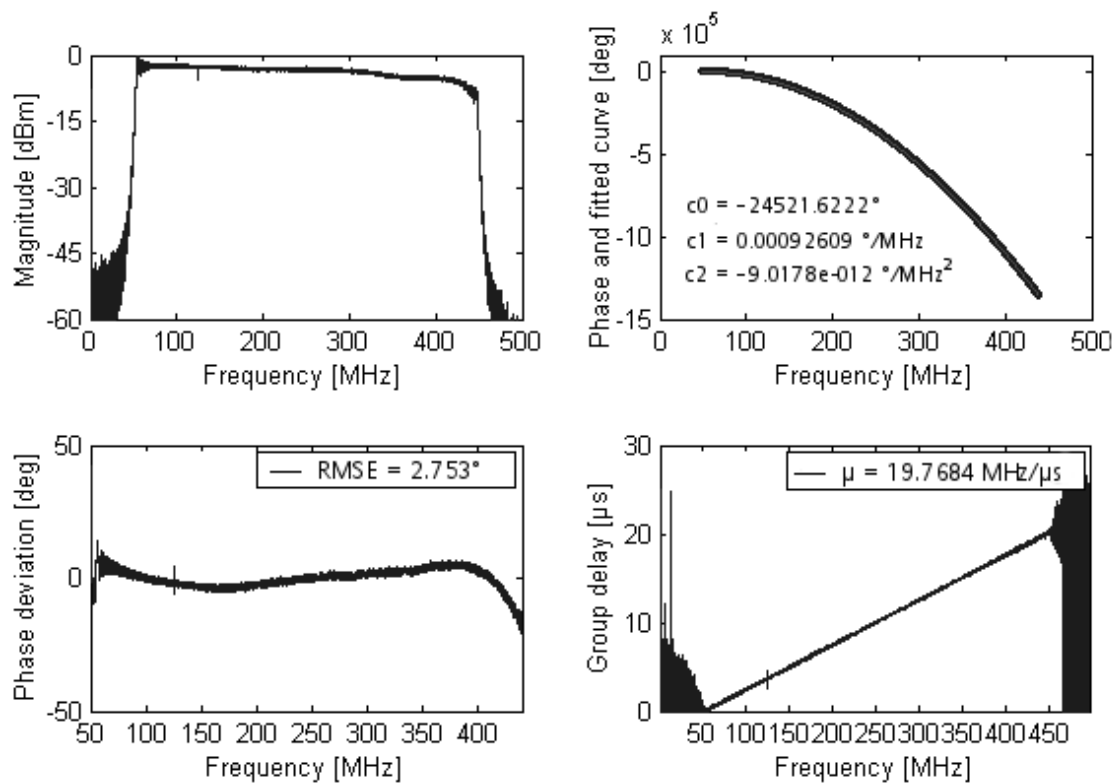


Figure 2.15: Chirp signal tools applied to the DDS board's output. *Upper left*: Calculated magnitude. *Upper right*: Wrapped phase and fitting in the desired frequency range. *Bottom left*: phase deviation and root mean square error. *Bottom right*: Calculation of the chirp rate.

quality aspects are affected by unwanted behaviors such as: nonlinearity, low SNR, base-band ripple produced by filters, and the amplifier's compression and saturation points. These sources of error typically signify deterioration in the system performance and thus produce effects which may be observed in the frequency and/or time domains (a suitable example is phase deviation).

As a result of this method, Fig. 2.17 displays the frequency- and time-domain response provided by the DDS board before the first up-conversion stage. In the frequency domain, it can be observed the 400-MHz bandwidth digitally-created chirp signal plus some harmonics after the first low-pass filtering (on the right side). In the time domain, the chirp signal lies within a 20- $\mu$ s period region where a smooth amplitude answer is typically required; as contrary to passband ripple which could increasingly appear after filtering stages.

Following, Fig. 2.18 shows the responses of the first up-conversion process where the initially created chirp signal within the 50 MHz to 450 MHz range is translated into the 1350 MHz to 1750 MHz frequency range. Here, one can appreciate the image band created in the mixing procedure; however, it is filtered by means of a passband filter.

Finally, Fig. 2.19 depicts the response before the main mixing stage. In this stage, the incoming atmospheric signal is mixed with the 800-MHz bandwidth chirp signal (the last is created after a doubling and passband filtering processes). A strong power density of

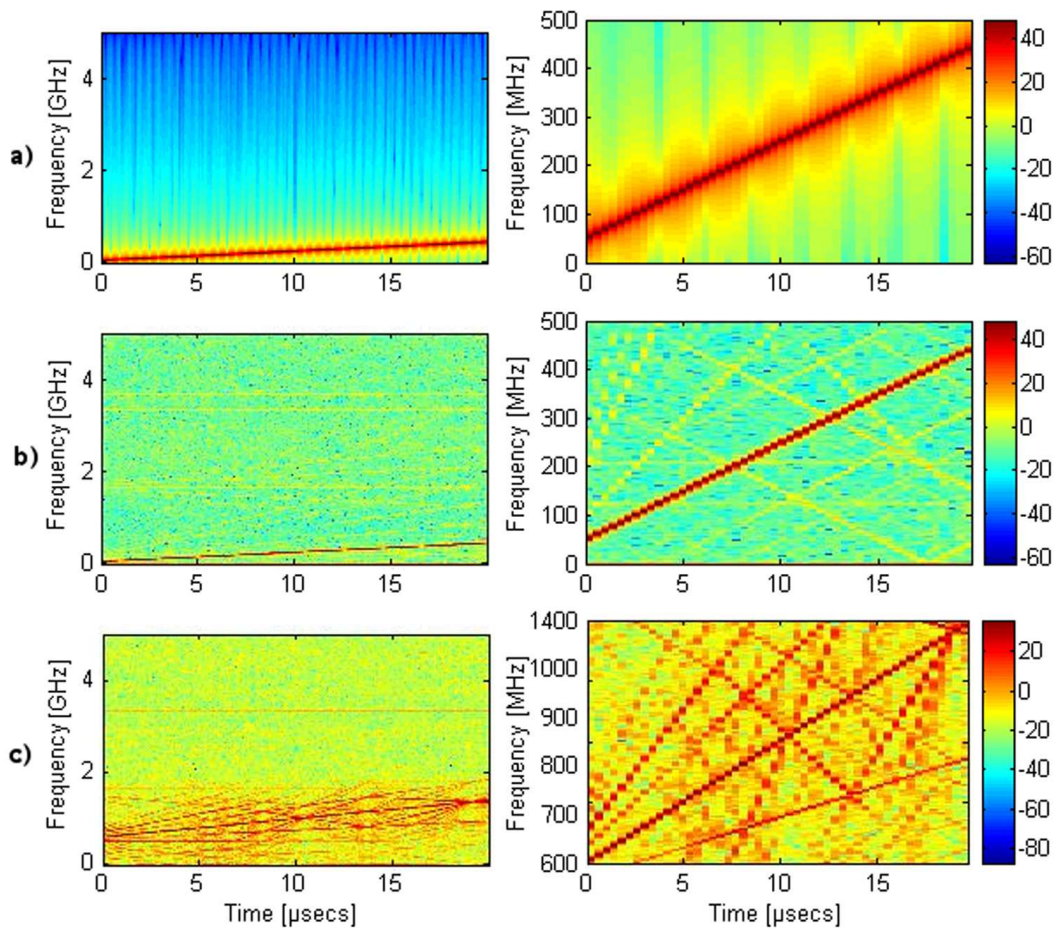


Figure 2.16: New analysis approach using Short-Term Fourier Transform (STFT) computation. *a)* Study in case of a synthetic perfect chimp signal. *b)* Chimp signal analysis right after the digital generation in the DDS board. *c)* Signal fed into the SAW filter. It can be seen that after the processes of amplification, doubling, mixing and filtering spurious frequencies appear producing deterioration in the signal.

the chimp signal should be expected in the frequency domain since this signal is injected in the LO port of the mixer.

### 2.4.3 Stability

Allan variance measurements are typically used in order to quantify the stability of microwave heterodyne spectrometers. The radiometer formula (Eq. 1.11) can be applied while the instrument is stable during the observation time between two calibrations. Since any additional noise above the radiometric level is unfavorable, one has to find the optimum integration time where the impact of drift contributions is nearly negligible. In other words, the radiometer equation is valid within the white noise part, i.e., prior to the Allan-variance minimum. The latter describes the turnover point where the radiometric noise with a negative slope of -1 in the logarithmic plot becomes dominated by the additional and undesired drift noise (see Schieder and Kramer, 2001).

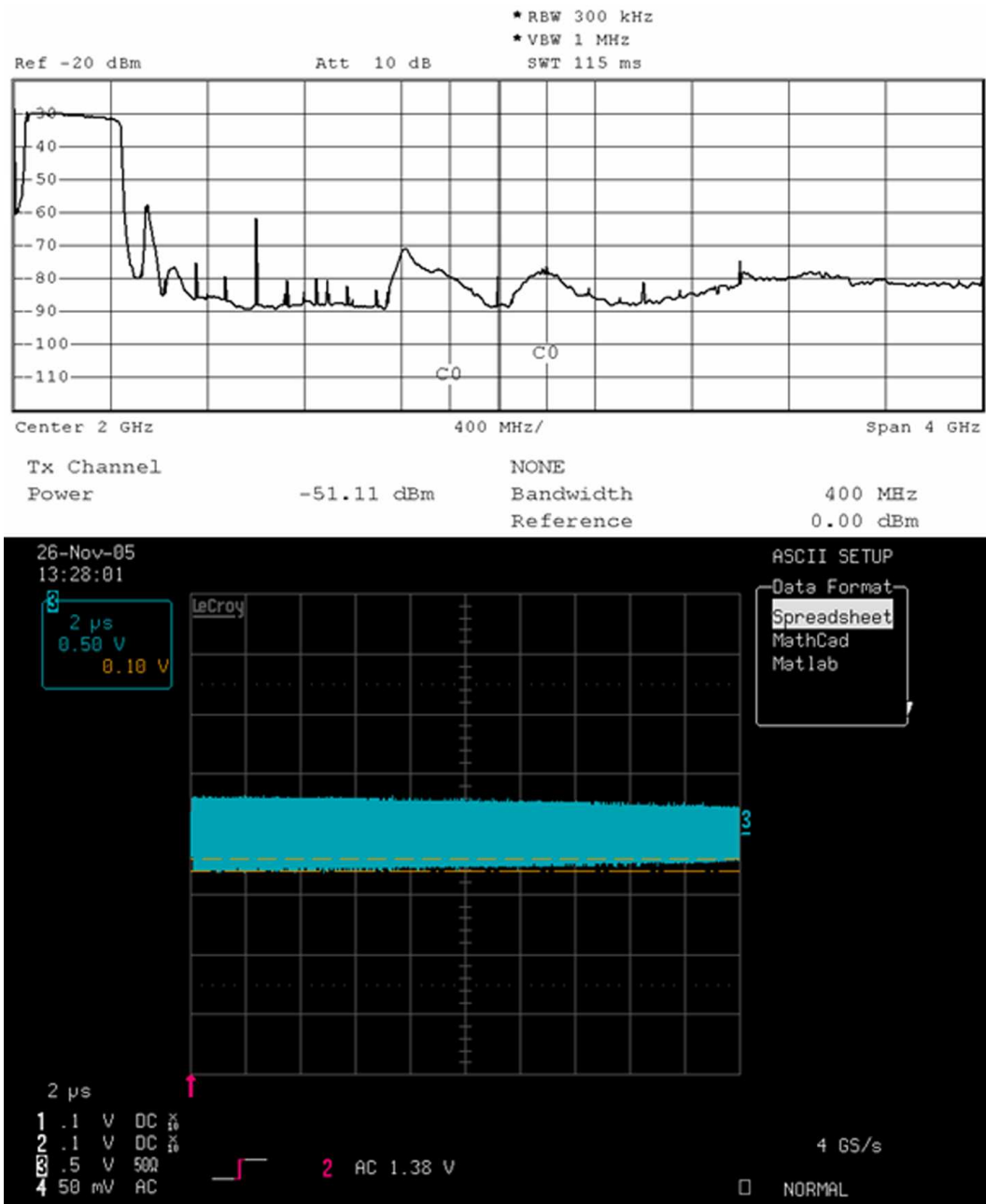


Figure 2.17: Frequency- and time-domain answers provided by the DDS board before the first up-conversion stage.



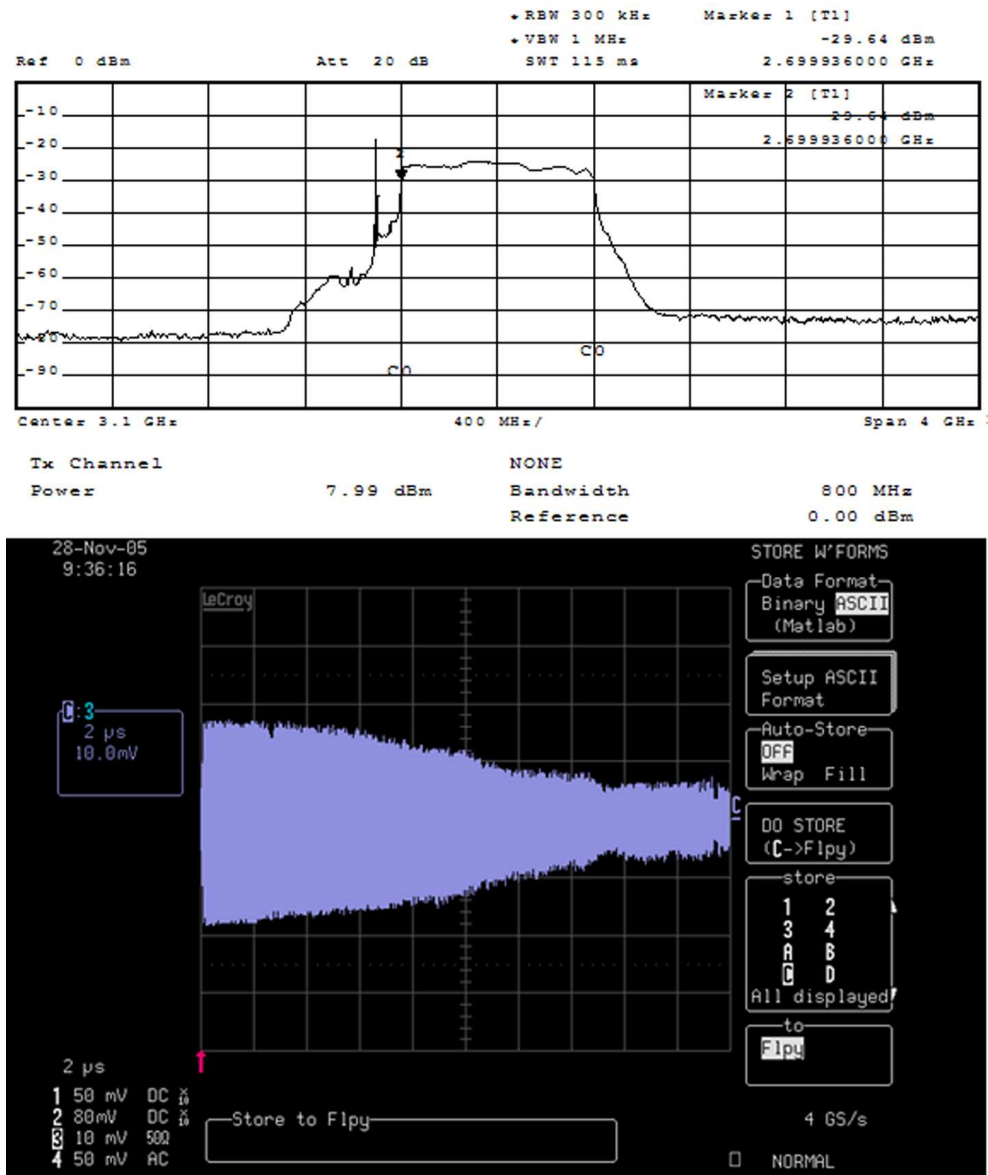


Figure 2.19: Frequency- and time- domain answers provided by the mixing stage where the incoming measured signal is mixed with the 800-MHz bandwidth chirp signal.

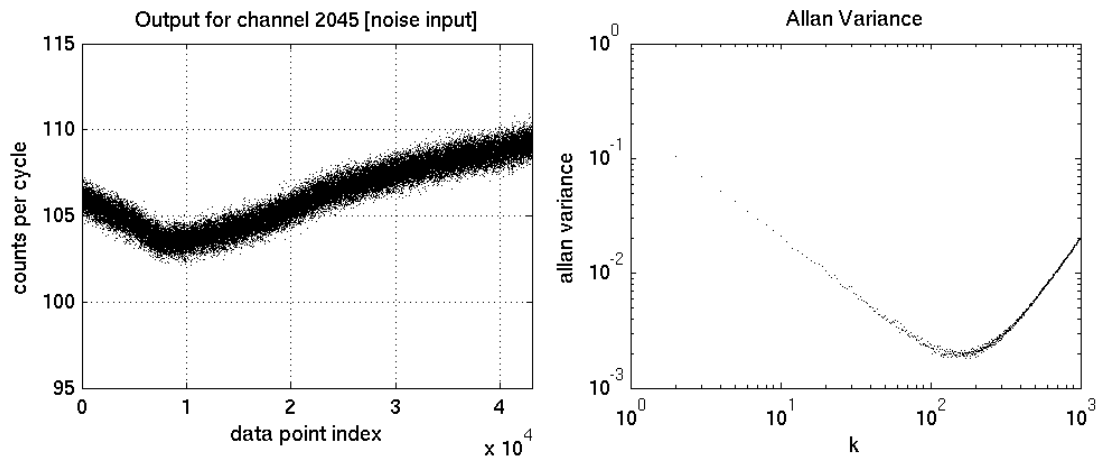


Figure 2.20: Allan variance calculation. *Left*: output count per cycle for the channel 2045 using a noise source during 43,000 spectra integrated in 1 second each. *Right*: the Allan variance of a frequency channel vs. integration time [s]. The Allan-variance time is defined by the minimum  $k$ , i.e., 173 s.

After warming up, 43,000 spectra with 1 second integration time for each were acquired using an ultra stable noise source input at a constant power level. The analysis of the data indicated a minimum Allan-variance time of 173 seconds, represented in the plot by the value  $k = 173$  (Fig. 2.20). The spectroscopic Allan variance, which performs a similar study in two independent channels, showed no independent drift behavior between them (Paganini and Hartogh, 2006).

The frequency stability of the spectrometer is linearly related to the temperature stability of the SAW filters. Thus, it is essential a good thermal stabilization of these devices. The used thermal stabilization results in a frequency stability of 550 Hz/°C (Villanueva, 2004).

#### 2.4.4 Spectral resolution

The response of the spectrometer to a sine wave is a  $\text{sinc}^2$  function with the first zero crossing in the frequency domain at  $1/t_C$ , this point defines the spectral resolution of the spectrometer. The dispersion time ( $t_C$ ) of 10  $\mu\text{s}$  incorporated by the SAW filter denotes a 100-kHz spectral resolution.

Another approach is to obtain the Full Width at Half Maximum (FWHM) of each channel (Fig. 2.21). A value of 121.2 kHz was obtained by calculating the FWHM of the sampled curved at each single channel in the whole range. The used step size was equal to a tenth of the nominal resolution (i.e., 10 kHz).

Furthermore, the deviations in the spectral scale linearity were calculated. This property describes the relationship between the input frequency and the corresponding expected frequency denoted by a specific channel index. This is performed by acquiring the mean standard deviation of each channel (referenced to the FWHM) in the complete operational instrument's bandwidth. As seen in Fig. 2.21, deviations smaller than 6% were determined for the complete amount of channels.

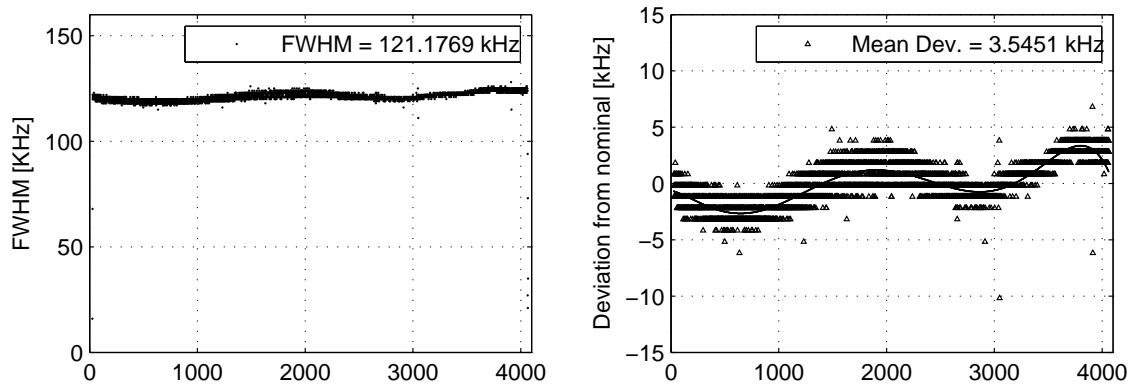


Figure 2.21: Spectral resolution and frequency linearity vs. channel number. *Left*: measurement of the spectral resolution (FWHM). *Right*: deviation of the obtained calculation from the expected nominal value ( $\sim 0.06$  of a channel).

### 2.4.5 Power linearity and dynamic range

As suggested by Villanueva and Hartogh (2004), three effects constrain the instrument's dynamic range: the high insertion loss of the SAW devices (more than 40 dB), the noise and interferences introduced during the RF signal processing, and the compression point of the different passive (mixers) and active components. The maximum signal amplitude in the RF part is the one which drives the main mixer (+10 dBm); i.e., where the incoming atmospheric signal is mixed with the chirp signal. Moreover, the lowest signal amplitude is the output of the SAW device (-60 dBm). The addition of digital techniques into the CTS design and the 50-dB SNR provided by the new arrange allow a wide range of adaptability which assures a proper dynamic range setup.

The linear response of the instrument (analog and digital parts) was attained by injecting a noise source at the CTS input connector and, by producing variable 1-dB attenuation steps in a 60-dB dynamic range, procure deviations of  $\pm 0.1$  and  $\pm 1$  dB after performing a linear fit of the spectrometer's response (see Paganini and Hartogh, 2006, Villanueva et al., 2006a). The input power is supplied by a noise source with  $\sim 1$  dB flatness, +10 dBm power level and an operational frequency which lies within the 1.9 to 2.3 GHz frequency band. The results, displayed in Fig. 2.22, show a dynamic range with a maximum deviation from linearity of  $\pm 1$  dB equal to 35 dB and  $\pm 0.1$  dB equal to 20 dB; and an optimum input power level of -35 dBm.

The previous explained analysis allows to predict the overall instrument's response by calculating the mean of the whole channels. In addition, a 3-dimensional plot allows to separately observe the response of each channel versus power input and power output (in counts/cycle). This analysis provides a more detailed evaluation of the instrument response on each single channel which is especially important to establish not only linear dynamic range, but also unexpected behaviors, e.g. possible regions which go into saturation and compression faster than others or even damaged SAW filters. Figure 2.23 displays an example of the last case where the upper plot indicates an unusual response of the instrument between channel numbers 2500 and 3000. In contrast, the lower plot depicts the normally expected operation. In Fig. 2.24, the sudden drop in channel 2700 clearly confirms an abnormal instrument's response while observing the hot load at the

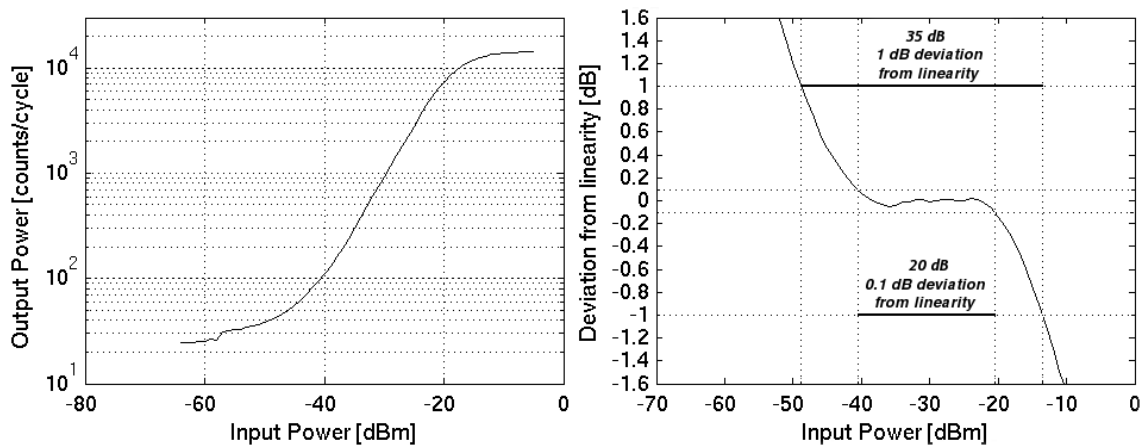


Figure 2.22: Power linearity study. *Left*: output power obtained by injecting a variable power noisy source at the CTS input connector. *Right*: the dynamic range calculation is attained from  $\pm 1$  dB and  $\pm 0.1$  dB deviations from a linear fit.

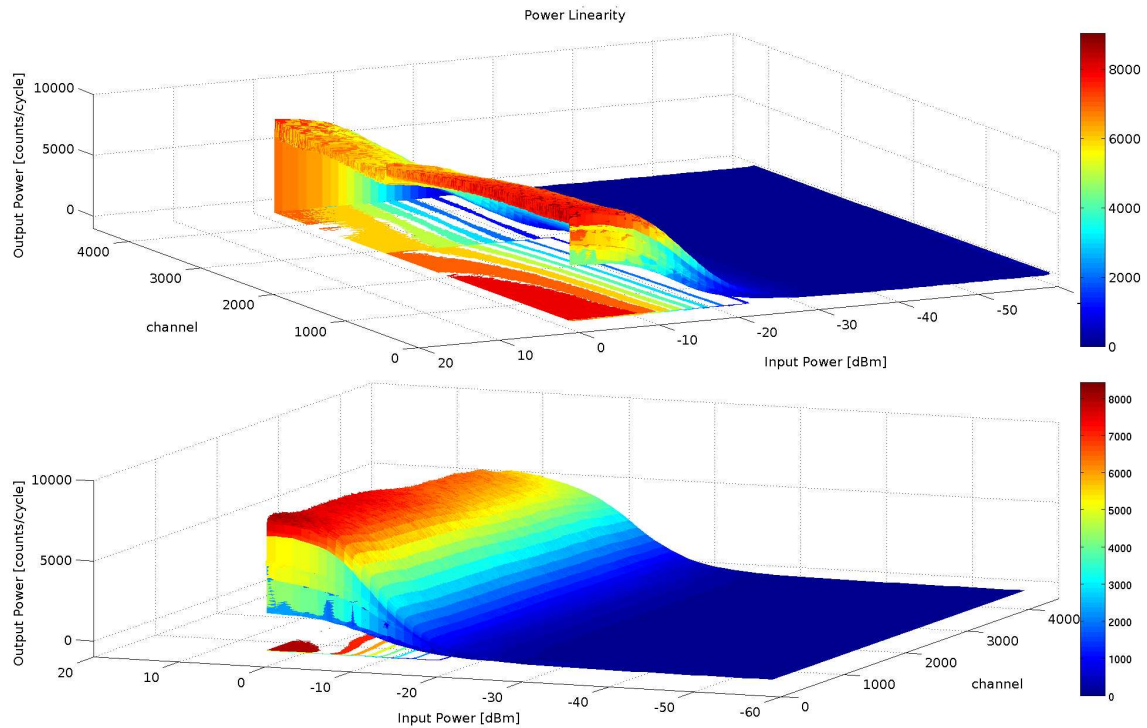


Figure 2.23: Power linearity study: a 3D power analysis of the output power against input power and channel number. This analysis is implemented in order to observe possible deterioration in the system. *Upper*: unusual instrument's response between channel numbers 2500 and 3000. *Bottom*: normal instrument's operation.

ozone radiometer using the CTS data-observing software (in an external computer). Later on, several RF stages were separately tested with the 3D power analysis. As a conclusion, this analysis truly suggested that such strange behavior might have been produced by a damaged SAW filter in the instrument.

An advantage of this method is the possibility to check complex devices in-situ with-

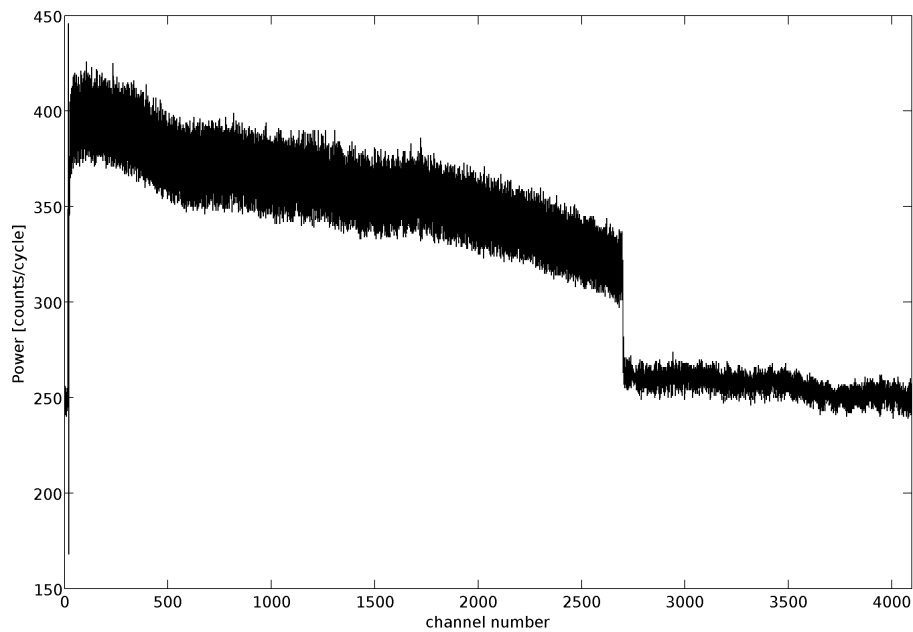


Figure 2.24: CTS data-observing software plot. The sudden drop in channel 2700 clearly confirms an abnormal instrument's response while observing the hot load at the ozone radiometer.

out removing them from the spectrometer. An illustrating case is SAW filters damage like after applying a high input power, which may lead to acoustomigration in the SAW's thin metal electrodes and thus deteriorates the performance or even destroy the device (Kubat et al., 2004). At first glance, this tool avoids the need for scanning-electron microscopes. In the CTS, SAW filters are embedded in Styrofoam<sup>®</sup> (a form of polystyrene), isolated by several layers of a thin polyimide film (Kapton<sup>®</sup>) and packed altogether in a temperature-controlled aluminum case at 40 °C in order to conserve their calibration in terms of temperature stability. Therefore, unnecessary demounting the SAW filter package could lead to variations in the filter's dispersive characteristics since they are highly sensitive to environmental temperature variations (Carr et al., 1972).

## 2.5 Observations and results

The previous section has broadly described the development, design and common laboratory analysis techniques used to evaluate a new 400-MHz bandwidth CTS. This section reviews some recent performance of the new CTS consisting on test results under real observing conditions. First light was observed in December 2005 by measuring the O<sub>3</sub> line using a 142-GHz ozone system as test facility at MPS in Katlenburg-Lindau, Germany (Fig. 2.25).

In order to test its response by observing astronomical objects, the instrument was installed at the Heinrich Hertz Submillimeter Telescope Observatory during the observing run of the 73P/Schwassmann-Wachmann 3 comet in May 2006 when it had its closest approach to the Earth (Paganini and Hartogh, 2006, Drahus et al., 2007, Küppers et al., 2006).

Table 2.1: Specifications of current CTS system

	Value	Error
Center frequency	2.1 GHz	$\pm 100$ kHz
Min. input frequency	1.9 GHz	$\pm 100$ kHz
Max. input frequency	2.3 GHz	$\pm 100$ kHz
Spectral resolution (noise equivalent) $1/t_C$	100 kHz	$\pm 10$ kHz
Spectral resolution (FWHM)	121.2 kHz	$\pm 2.4$ kHz
Channel spacing	97.6 kHz	$\pm 245$ Hz
Bandwidth (-3 dB)	400 MHz	$\pm 1$ MHz
Optimal RF power input (noise)	-35 dBm	$\pm 0.1$ dB
Min. RF power input (noise)	-45 dBm	$\pm 0.1$ dB
Max. RF power input (noise)	-25 dBm	$\pm 0.1$ dB
Noise input dynamic range	35 dB	$\pm 1$ dB
Noise input dynamic range	20 dB	$\pm 0.1$ dB
Frequency linearity	3.5 kHz	$\pm 2.4$ kHz
Absolute Allan-variance time	173 s	$\pm 20$ s
Channels	4096	-
Maximum power consumption [AC]	79.5 W	$\pm 2$ W
Nominal power consumption [AC] (>30 min)	68.6 W	$\pm 2$ W
Dimensions [ $cm^3$ ]	43 (w) x 8 (h) x 45 (d)	
Data interfaces	Ethernet, RS232, TTL	

#### Specifications for the dispersive elements

Compressor bandwidth	400 MHz	$\pm 1$ MHz
Dispersion time ( $t_C$ ) of compressor	10 $\mu s$	$\pm 1$ $\mu s$
Insertion loss of compressor	-45 dB	$\pm 3$ dB
Time-bandwidth product of compressor	4000	-
Expander bandwidth after RF doubling	800 MHz	$\pm 8$ MHz
Expander sampling frequency	1 GHz	$\pm 3$ ppm
Dispersion time ( $t_E$ ) of expander	20 $\mu s$	$\pm 400$ ns

### 2.5.1 Ozone measurements

Detection of the rotational transition of ozone at 142.175 GHz is typically performed since 1992 at MPS (51.39° N, 10.13° E and 140 m.a.s.l) providing altitude profiles from 20 to 80 km (Hartogh and Jarchow, 1995). Currently, the frontend radiometer detects the 142-GHz ozone line using two backend CTSs: a) a 40-MHz bandwidth CTS described by Hartogh (1998), Hartogh and Jarchow (1995) and b) a 220-MHz bandwidth SOFIA-GREAT CTS (Villanueva and Hartogh, 2004, Villanueva, 2004). In this heterodyne system the atmospheric signal is first filtered by a Martin-Puplett single sideband filter, then combined with a local oscillator signal using a folded Fabry-Perot and afterward fed back into a cooled single-ended Schottky mixer. The Schottky mixer provides a down-converted signal which is amplified and finally analyzed in the (backend) spectrometer. Data are taken with a fixed elevation angle of 30° and calibrated every six seconds using two external reference loads at 78 K and ambient temperature. The heterodyne system possesses a sin-

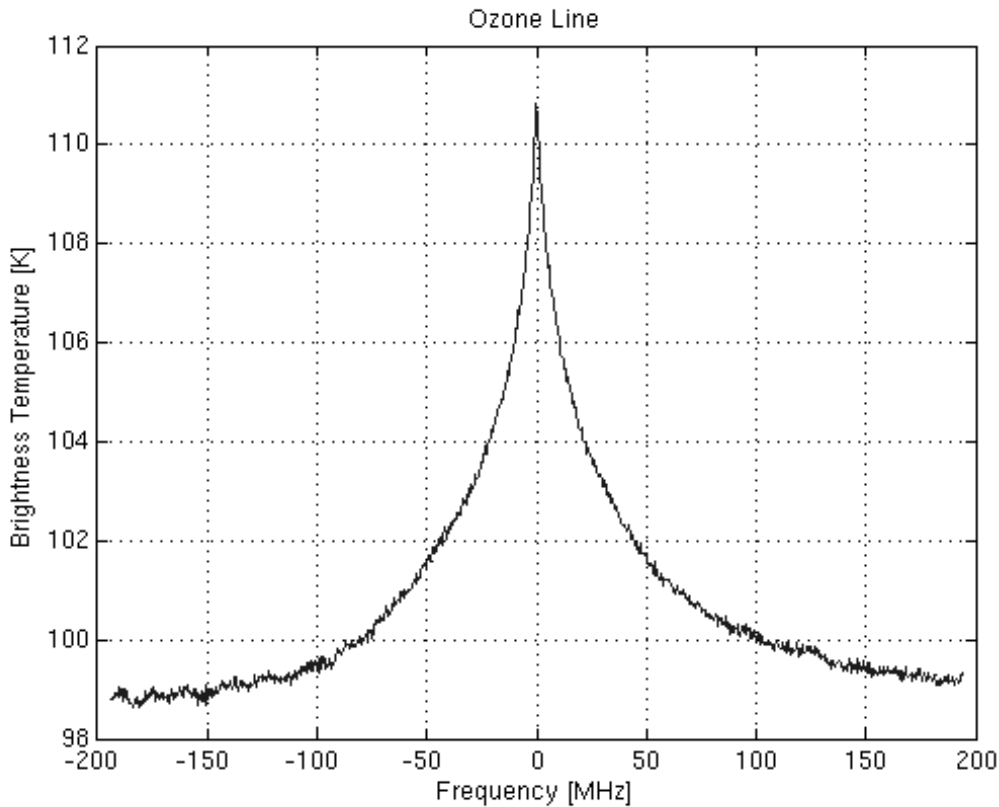


Figure 2.25: First light: Ozone spectrum obtained using a 142-GHz ozone radiometer at MPS in Katlenburg-Lindau, Germany.

gle sideband noise temperature of 500 K (Hartogh et al., 2004) and has demonstrated to provide accurate and consistent results (see Hartogh, 1989, Hartogh and Hartmann, 1990, Hartogh and Jarchow, 1995).

The 400-MHz bandwidth CTS was implemented as third-running backend. Several tests have been conducted over the last 2 years in order to evaluate the instruments' responses. Figure 2.25 shows the first successfully detected ozone spectrum by the 400-MHz CTS in December 2005 (Paganini and Hartogh, 2006).

As explained earlier in Chapter 1, the ozone spectrum, in brightness temperature units ( $T_A$ ) is obtained from a calibration process. Basically, this process is performed by the heterodyne system using the following formula (cf. Section 1.2.3 and Eq. A.2):

$$T_A = \frac{P_A - P_C}{P_H - P_C}(T_H - T_C) + T_C \quad (2.9)$$

where  $P_A$  is the power density of the observed object (atmosphere/sky), e.g. some planetary atmosphere,  $P_H$  is the power density of the hot load,  $P_C$  is the power density of the cold load (power is represented in counts/cycle), whereas  $T_H$  and  $T_C$  are the cold- and hot-load temperatures calculated by a PT100 sensor.

If the system performs a 6-second observation at each position [Hot|Atm|Cold positions] and possesses a calibration cycle: H-A-C-A-H, it denotes that the system takes 12 seconds to fulfill Eq. 2.9 and therefore conduct a complete integration (i.e., obtain a

calibrated spectrum). A continuous ozone-measurement process can be displayed in Fig. 2.26, wherein: a)  $T_B$  is derived using Eq. 2.9; b) and c) plot  $T_H$  and  $T_C$  as measured by the PT100 sensor, respectively; d) and e) show the measured power density,  $P_H$  and  $P_C$ , at the calibration loads; and finally, f) the calculated power density at sky position, represented by the red line between the black and blue ones, which represent the hot and cold loads. Here, it can be observed that the  $T_B$  variations mainly represent the tropospheric humidity variation. High  $T_B$  means rainy weather, meanwhile low  $T_B$  indicates clear sky or at least dry tropospheric air. The strange ripple in the hot load is due to variations of the air temperature produced by the air conditioning in the laboratory. The cold load behavior is related to the filling interval of liquid nitrogen.

## 2.5.2 Astronomical observations at the Heinrich Hertz Submillimeter Telescope (HHSMT)

The HHSMT is located on Mt. Graham in south-east Arizona (longitude W 109°53'26'', latitude N 32°42'05'') at an altitude of 3200 m. The Telescope consists of a Cassegrain system with paraboloidal main reflector and hyperboloidal secondary reflector. The antenna has a diameter of 10 m, the absolute pointing accuracy is about 2'', with a tracking accuracy of better than 1'' (Baars et al., 1999). The observations were performed using the dual polarization, single sideband 1.3mmJT (130-300 GHz) and the dual-channel, double sideband MPIfR SIS-345 receivers. The spectral data are automatically calibrated by the telescope software into antenna temperature scale ( $T_A^*$ ) using the chopper-wheel method (Ulich and Haas, 1976). The pointing accuracy was periodically checked after some hours, either on a planet or other bright source such as a star. The HHSMT is equipped with several backends: a 218-MHz bandwidth (BW) chirp transform spectrometer with 46.6 kHz frequency resolution ( $\Delta f$ ); a set of three AOSs: a) AOSA:  $\Delta f = 934$  kHz, BW = 1 GHz, b) AOSB:  $\Delta f = 913$  kHz, BW = 1 GHz, c) AOSC:  $\Delta f = 370$  kHz, BW = 250 MHz; the so-called Forbes filterbank with 1 GHz bandwidth and 250 kHz frequency resolution; and the newly integrated 400-MHz bandwidth CTS with 100 kHz frequency resolution (0.11 km/s spatial resolution at  $f = 250$  GHz). The measured spectra were reduced using the CLASS software from the GILDAS software package.

### 2.5.2.1 Comets

Comets are considered as primitive, leftover building blocks of the outer solar system formation process. Therefore, their chemical composition provides clues about the different physical processes that led to the formation of giant planets. Comets are frequently classified according to their orbital periods in two dynamical reservoirs: the Oort Cloud with long-period comets and the Kuiper Belt with short-period comets (Gladman, 2005). Individual comets from both reservoirs can be perturbed towards the inner solar system by various gravitational effects.

A convenient method to determine the chemical composition of comets, i.e. the nature of ices and rocks which comprise the nucleus, is to observe secondary products such as parent molecules (rotational and vibrational-rotational transitions) and daughter molecules (electronic transitions) which result from their photodissociation (Crovisier and Encrenaz, 2000). As a comet approaches the Sun (Fig. 2.27), the ices sublime and

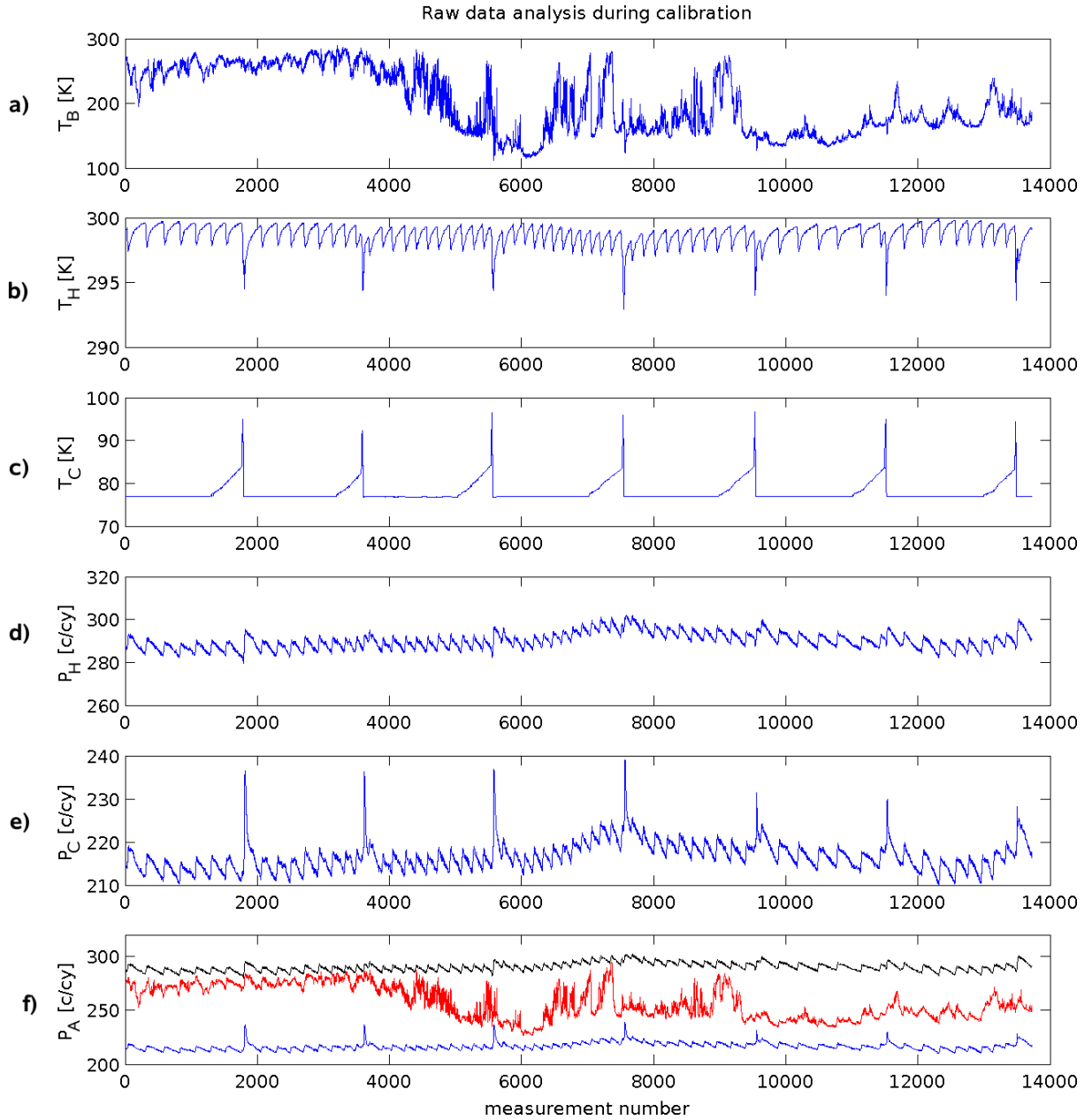


Figure 2.26: Calibration process: a)  $T_B$  is derived using Eq. 2.9; b) and c) plot  $T_H$  and  $T_C$  as measured by the PT100 sensor, respectively; d) and e) show the measured power density,  $P_H$  and  $P_C$ , at the calibration loads; and finally, f) the measured power density at sky position represented by the red line between the black and blue ones, which display the hot and cold loads respectively.

the ejected molecules can be spectroscopically detected, e.g. in the (sub)mm-wavelength range by observing their rotational transitions. Chirp transform spectrometers have proven to be an efficient tool in identifying cometary parent molecules because the frequency of narrow lines can be observed with very high accuracy and resolution, and thus lead to unambiguous identification of molecules and their spectral features.

The Jupiter-family comet 73P/Schwassmann-Wachmann 3 (SW3) broke up into several pieces during its perihelion passage in 1995. At least four fragments named alphabetically were observed (Bohnhardt et al., 1995), however, the fourth was not seen elsewhere and therefore might have been a very short-lived condensation. Several phenomena may trigger break-up of a cometary nucleus, the extremely low cohesion being one of the main reasons. During the close approach of the comet to the Earth, in May 2006, over three dozen separate pieces were observed. This provided a unique opportunity to study the homogeneity of the cometary nucleus by comparison of the composition of the different fragments (see Villanueva et al., 2006c, Dello Russo et al., 2007) which due to outburst started to defragment (Fig. 2.28).

Additionally, measurements of the same molecule at different geocentric distances sampled different spatial scales at the comet. These allow to derive the spatial distribution of molecules in the coma and to derive conclusions about their sources (Küppers et al., 2006) thanks to the freshly released cometary material (due to break-up). The observed components were mainly fragments B and C focusing on molecular species (HCN, HNC, CH<sub>3</sub>OH, CO, H<sub>2</sub>CO, CS) and isotopic ratios (H<sup>13</sup>CN), under good weather conditions (see Fig. 2.29 for HCN spectrum).

The cause of cometary break-ups is still uncertain. One suggested mechanism is splitting due to fast rotation of the nucleus. Drahus et al. (2007) studied the rotation period of the comet fragments by measuring the HCN production rate which was stimulated by the nucleus rotation. The light curve of comet 73P-C in HCN showed strong non-random variations. Among several plausible solutions for periodicity, a rotation period between 3.0 and 3.4 hours was suggested to be the most likely.

The observing mode for cometary observation was position switching (PS) where the telescope was first pointed on the source (on-position) for 15 seconds integration time, and then the same was repeated for the background (off-position). As a rule of thumb, the integration time (in seconds) is chosen such that the system is stable during this time (i.e., within the Allan-variance time) providing good baseline except for some occasional receiver instabilities. A complete scan was finished after 5 minutes. After each 1-hour observing interval, a pointing source (such as Mars) was observed again for pointing-accuracy determination and flux calibration (4 minutes). Afterwards, the scanning procedure was repeated; i.e., the comet was observed again for 1 hour.

An important part of cometary physics is concerned with understanding the flow of gas and dust released by the nucleus. Close to the nucleus, molecules are subjected to frequent collisions. The gas is then governed by the laws of classical hydrodynamics (Crovisier and Encrenaz, 2000). As suggested by Veal et al. (2002), understanding the distribution and temporal behavior of molecular gases in cometary comae is essential for accurate production rate calculations and correct modeling of the comae. Additionally, several questions about the origin and time variability of coma gas have not yet been answered such as understanding the production mechanism of cometary cyanide (CN) and hydrogen isocyanide (HNC) or even their volatile composition (e.g. see Villanueva et

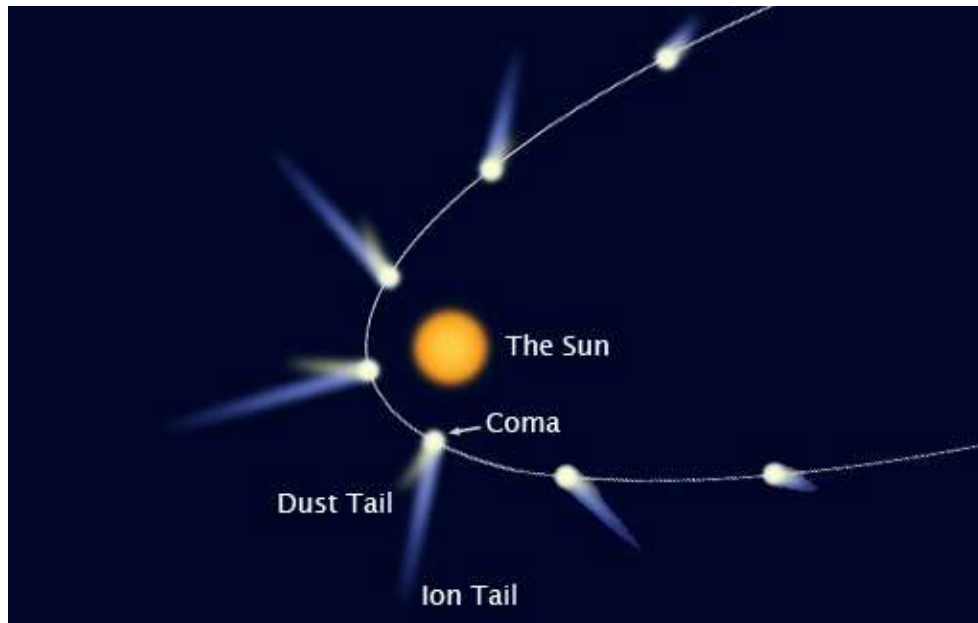


Figure 2.27: As the comet approaches the Sun, the icy material begins to sublimate, releasing dust and gas from the rocky nucleus.

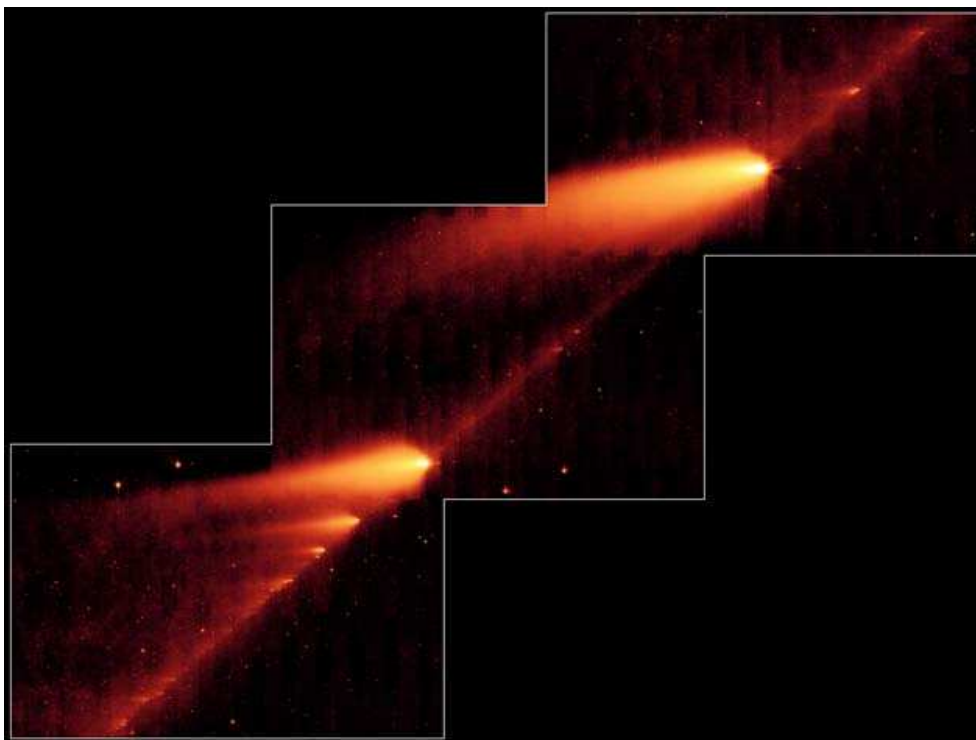


Figure 2.28: Comet 73P/Schwassmann-Wachmann 3: an image showing several fragments. Obtained between the 4 and 6 of May, 2006 by the infrared camera on-board the Spitzer Space Telescope. The brightest fragment at the upper right of the track is fragment C. Bright fragment B is below and left of center. Credit: NASA/JPL-Caltech.

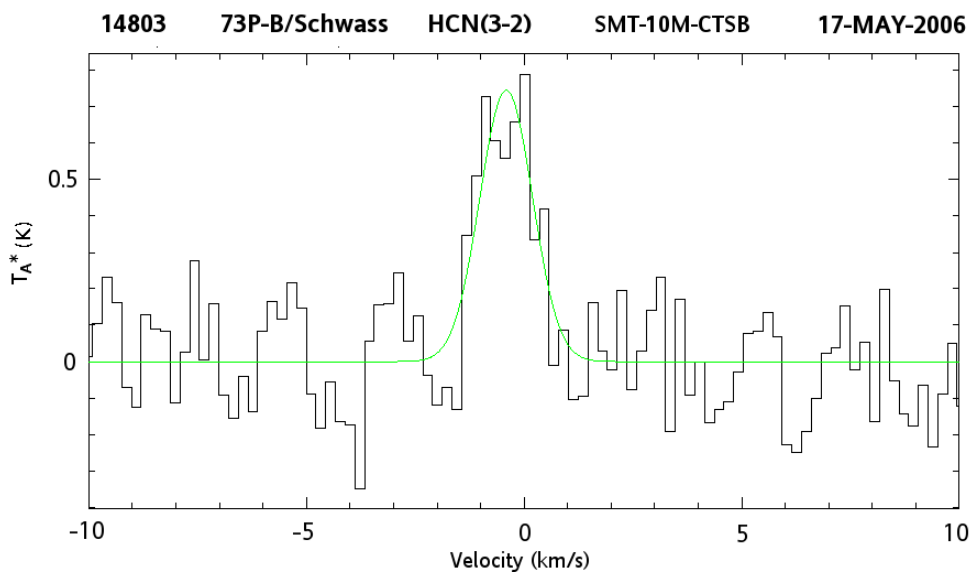


Figure 2.29: HCN(3-2) emission line (in antenna temperature scale [K] vs. velocity [km/s]) of the 73P-B/Schwassmann-Wachmann 3 comet during its closest approach on May 17, 2006 at HHSMT on Mt. Graham, Arizona. The black plot represents the body spectrum and the green one shows a gaussian fit (usually applied to determine the area under the curve).

al., 2006b). Hydrogen cyanide (HCN) has been frequently suggested as a parent for CN, however, the evidence for another parent of CN was found for several comets (see Fray et al., 2005, Woodney et al., 2002).

Since the first detection of hydrogen cyanide in comet C/1973 E1 (Kohoutek) (Huebner et al., 1974), the HCN molecule in the cometary coma has been extensively studied on several other comets, e.g. in comet P/Halley (Depois et al., 1986), comet C/1996 B2 (Hyakutake) (Mumma et al., 1996, Biver et al., 1999), comet C/1995 O1 (Hale-Bopp) (Irvine et al., 1997, Hofstadter et al., 1999, Woodney et al., 2002), comet C/1999 S4 (LINEAR) (Hogerheijde et al., 2004), and recently comet 73P/SW3 (Drahus et al., 2007, Villanueva et al., 2006b).

Theoretical studies of HNC formation in cometary comae have shown that ion-molecule chemistry cannot produce such large abundance of HNC (Rodgers and Charnley, 1998). Evidence for a dust source of HNC came from the observations of Blake et al. (1998). It is clear that more observations will provide a deeper understanding of the origin of cometary HCN. Preferably, HNC and HCN maps should be acquired simultaneously and so follow the heliocentric variation of the HNC/HCN ratio in a number of comets, including both Oort Cloud and Kuiper Belt objects (Rodgers et al., 2003). Mapping the spatial distribution of HCN and HNC (e.g. Charnley et al., 2002, Veal et al., 2002, Blake et al., 1998, Friedel et al., 2005) may also give more clues on their origin and relationship with other molecules in the coma.

Rodgers and Charnley (2002) concludes that the extended source of HNC is also likely related with the observed extended sources of HCN and CN. The high spectral resolution allowed by chirp transform spectrometers for lines at (sub)mm wavelengths provided an important tool for the study of cometary outflows through the HCN(3-2) molecule, being

in fact, a complementary tool for optical imaging. On 12 May 2006, there was a unique opportunity to map (for the first time with a CTS) the HCN molecule distribution in fragments B and C of comet SW3. The observations were carried out during the comet's closest approach to the Earth, which coincide with the outburst activity of fragment B.

A spectral distribution map can be constrained by observing the comet at different Right Ascension (RA) and Declination (Dec) offsets from the comet's central position (Fig. 2.30). For these observations, the comet position was:  $r$  (heliocentric distance) = 1.015 AU,  $\Delta$  (geocentric distance) = 0.07 AU, the comet's elongation angle ( $\phi$ , Sun-Earth-Comet) =  $92^\circ$ , comet's phase angle ( $\beta$ , Sun-Comet-Earth) =  $84^\circ$ , the position angle of the extended radius vector (PsAng) =  $245^\circ$ , and the minus velocity vector (PsAMV) =  $317^\circ$ . Fragment B (Fig. 2.31) was observed between 12:25 and 14:50 UT and fragment C (Fig. 2.32) between 9:17 to 11:40 UT (for further details, see Appendix C). The parameters were obtained from the Jet Propulsion Laboratory molecular spectroscopy data base (<http://spec.jpl.nasa.gov>).

In 2014, the Rosetta mission will encounter comet 67P/Churyumov-Gerasimenko and provide, for the first time, the chance to directly study the global characterization of its nucleus, surface morphology and composition (amongst others). Meanwhile, since there are no direct ways to determine the composition of the nucleus, the estimation of nuclear abundances is relied on gas phase observations of coma molecules. Additionally, numerous chemical processes occur in the coma, and thus accurate chemical models are of importance when using coma observations to derive nuclear ice composition (Charnley et al., 2002). It is clear that more observations are needed to understand which processes were forming the planets and shaping the outer solar system (Gladman, 2005). Especially interesting is mapping over several days in order to track the HCN distribution and variability on short-term, daily, and weekly scales, if possible.

### 2.5.2.2 Mars and other sources

The main observed target during the observation campaign was 73P fragments B and C. Nevertheless, the aim of this test was not only to show the spectrometer high resolution, which is essential for the study of narrow features (e.g., in cometary emission lines), but also to detect relatively broad lines and thus demonstrate the different capabilities of the new CTS. Therefore, some observations of Mars and other molecular clouds were performed. The observing mode was dual beam switching (BSP) which gave flat baselines with good cancellation of the variable sky contribution for a broader bandwidth. In this mode the source is integrated for 4 minutes like when doing normal beam switch; i.e., the telescope is switched between the 'on' and 'off' positions by using a rapidly moving mirror. The on and off positions are chosen to be at the same elevation about 6 arcmin apart and switching can be implemented with a frequency of about 2 Hz. As a result, the final spectrum is obtained by the sum of these two measurements where baseline features cancel out.

One of the interesting molecules in the Martian atmosphere is carbon monoxide (CO). CO is a key molecule for understanding the aeronomical processes and the stability of the Martian atmosphere (Lellouch et al., 1989). Figure 2.33 shows the observed spectrum of the  $^{12}\text{CO}$  J = 2-1 absorption line from the Mars' atmosphere.

As stated earlier, observations of well-known standard sources (Fig. 2.34 and 2.35)

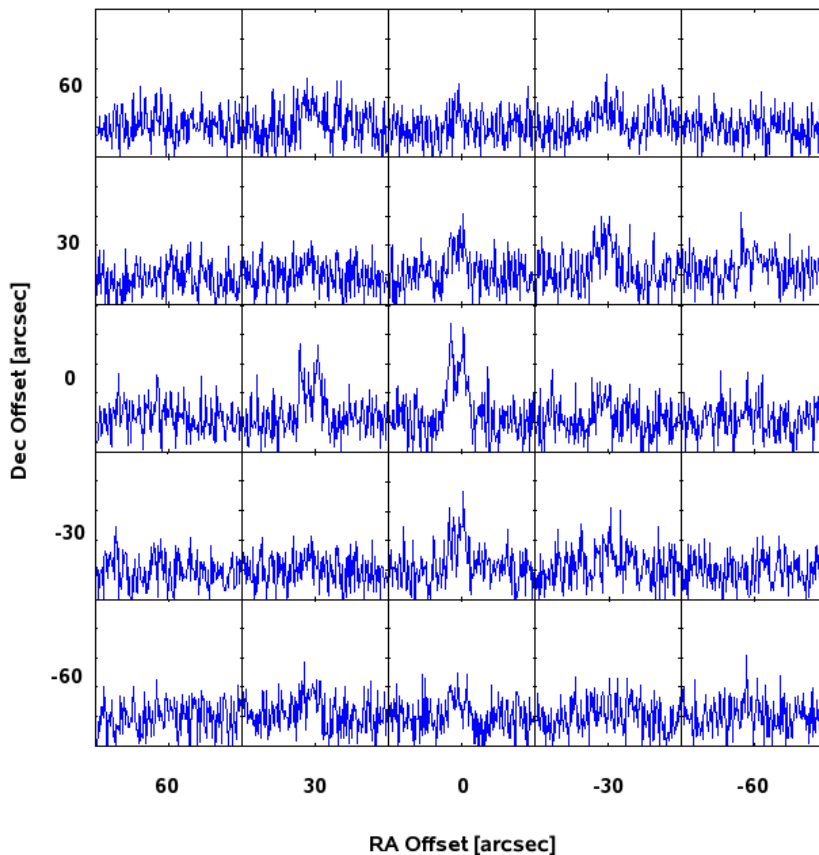


Figure 2.30: Observing the comet at different position in Right Ascension (RA) and Declination (Dec) offsets from the comet's center position (each single sub-plot is represented in antenna temperature scale [K] vs. velocity [km/s]). Spectral map of the HCN(3-2) emission line of the 73P-B/Schwassmann-Wachmann 3 comet on May 12, 2006 at HHSMT on Mt. Graham, Arizona.

called flux calibrators are performed after on-position, e.g. a comet integration (see Mauersberger et al., 1989, Wang et al., 1994). The concept is to obtain the telescope-beam efficiencies, and thus the proper scaling factor, in order to transform the source antenna temperature corrected for atmospheric, ohmic, and all spillover losses (Kutner and Ulich, 1981) into main-beam brightness temperatures (Vila-Vilaró et al., 2003, Bieging et al., 2000).

## 2.6 Analysis and performance

The new CTS provides 100 kHz spectral resolution and 400 MHz bandwidth. This allows observed spectral features from several astronomical objects to be analyzed in high detail. Limitations in bandwidth and resolution are given by parameters as described below. It

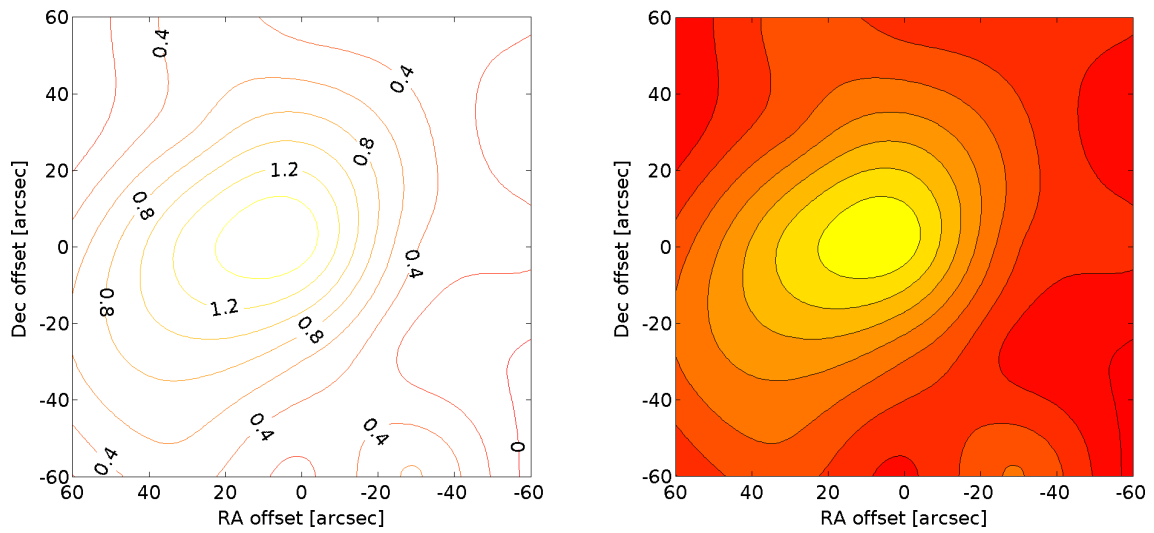


Figure 2.31: HCN  $J = 3 \rightarrow 2$  emission from 73P-B/Schwassmann-Wachmann 3 (fragment B) on 12 May, 2006 at HHSMT on Mt. Graham, Arizona. The observed interval is within 12:25 to 14:50 UT Time. *Left*: contour plot. The peak integrated intensities are in K km/s (using  $T_A^*$ ). *Right*: Colormap.

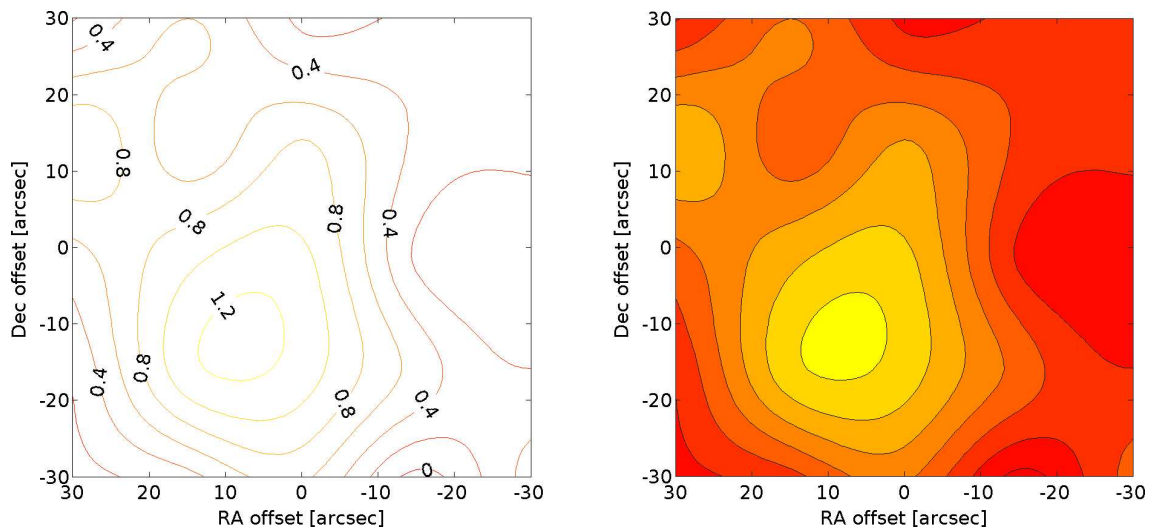


Figure 2.32: HCN  $J = 3 \rightarrow 2$  emission from 73P-C/Schwassmann-Wachmann 3 (fragment C) on 12 May, 2006 at HHSMT on Mt. Graham, Arizona. The observed interval is within 9:17 to 11:40 UT Time. *Left*: contour plot. The peak integrated intensities are in K km/s (using  $T_A^*$ ). *Right*: Colormap.

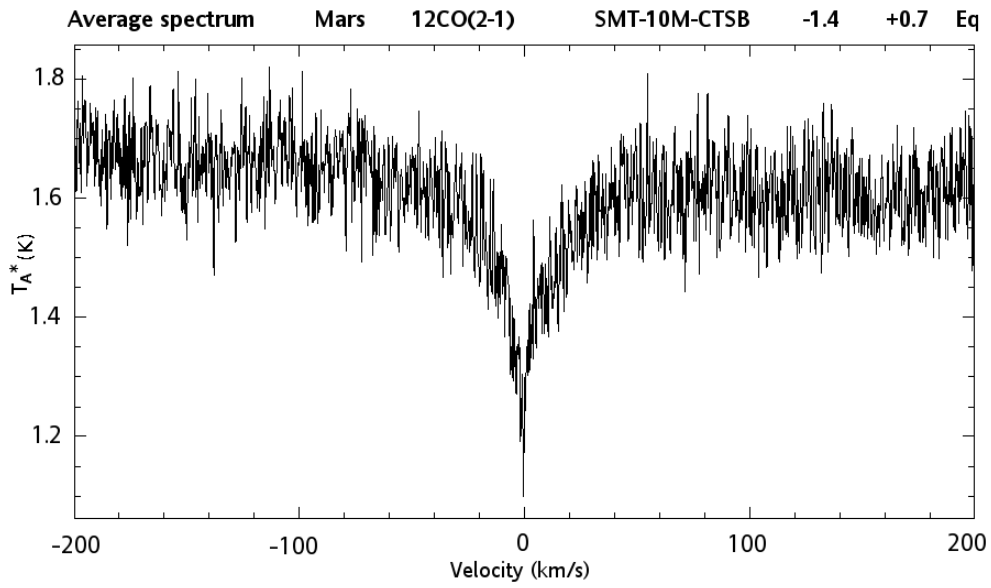


Figure 2.33:  $^{12}\text{CO}$   $J = 2 \rightarrow 1$  absorption line of Mars observed at HHSMT during the 73P/S-W 3 observing run.

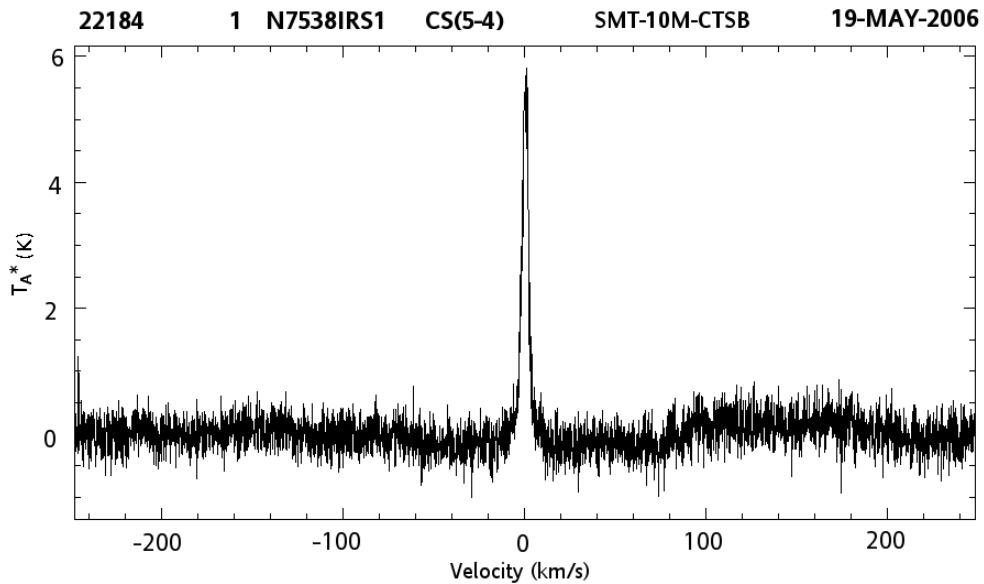


Figure 2.34: Observation of the N7538IRS1 star (used as a standard source). CS  $J = 5 \rightarrow 4$  emission line.

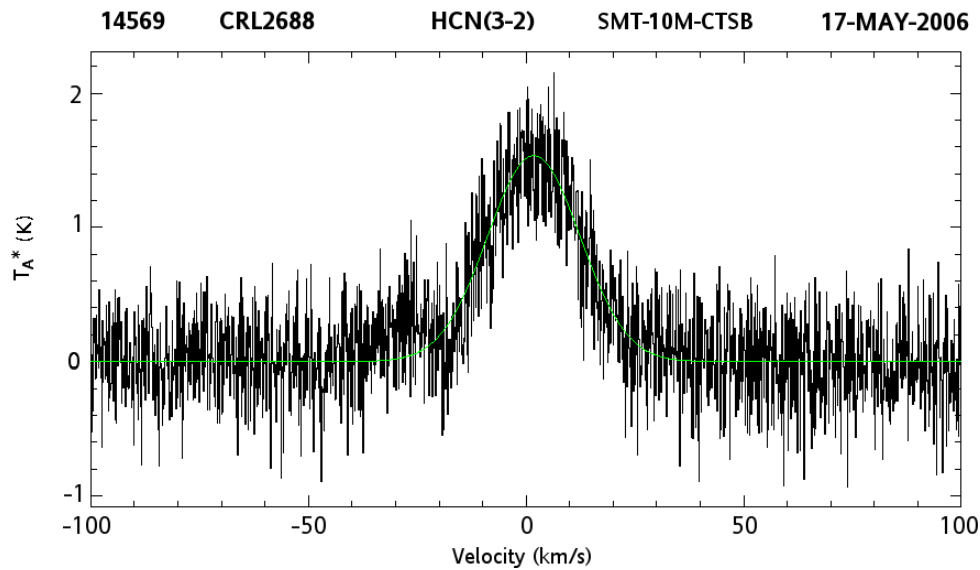


Figure 2.35: HCN  $J = 3 \rightarrow 2$  emission line. Observation of the Egg Nebula, also known as CRL2688 (used as a standard source). The black plot represents the object spectrum, meanwhile the green one displays a gaussian fit (usually applied to determine the area under the curve).

should be also stated here that other limitations have to be taken into account depending on the application of the CTS, respectively on the environment in where the CTS is used.

#### *Bandwidth and spectral resolution*

In case the astronomer pursues to identify several (widely separated) spectral lines from a certain object all at the same spectral band, as much bandwidth as possible would be preferable in a spectrometer. Spectrometers, however, usually offer a larger bandwidth at the cost of spectral resolution. Hence (on astronomical observations) requirements in bandwidth and spectral resolution are basically established by the observer and the phenomena under observation.

Nowadays, the main limitations for broader bandwidth CTSs and higher spectral resolutions lie in the high propagation loss in the  $\text{LiNbO}_3$  SAW device. In other words, the higher the bandwidth, the higher the center frequency of the SAW device, which leads to higher insertion loss of the  $\text{LiNbO}_3$  substrate (or wafer) material. The practical limit in bandwidth of  $\text{LiNbO}_3$  is 800 MHz with a center frequency of 2 GHz (Hartogh, priv. comm.). Alternatively, new research efforts, as the ones developed by a PhD student at MPS in collaboration with PTB (Physikalisch-Technische Bundesanstalt) and the University of Freiburg (Li, 2008), seek better performances by using different materials, e.g. Sapphire ( $\text{Al}_2\text{O}_3$ ).

The current CTS achieves the highest bandwidth so far compared with previous CTS developments. On the other hand, it has approximately 50% less spectral resolution with respect to its predecessor, the SOFIA-GREAT CTS. This is established by the SAW device's dispersion time ( $t_C$ ) of  $10 \mu\text{s}$ . Techniques as the ones developed by Li (2008) will allow, in the near future, SAW devices to achieve 400 MHz bandwidth (or even higher)

and  $20 \mu\text{s}$  dispersion time, and thus improve the frequency resolution up to 50 kHz. As discussed in Section 2.3, the DDS board only needs to be reprogrammed using the new digital properties in order to create a 400-MHz bandwidth chirp signal with  $40 \mu\text{s}$  dispersion time (instead of  $20 \mu\text{s}$ ). Furthermore, the RF section stays the same.

The previous restrictions established by the processing speed of digital units have been overcome by new digital techniques; these apply to the chirp generation (i.e. DDS) as well as the digital preprocessing (i.e. ADC and data-acquisition electronics). For the last 4 years, the DDS technology (as the one required by CTS developments) has been limited to an upper digital-chirp-signal frequency of 450 MHz. It means that further postprocessing methods such as doubling or tripling are latterly required, usually adding undesired spurious. In the case of the SOFIA-GREAT CTS, this problem may be surpassed by the new DDS board (which does not require doubling or tripling techniques for that design). Needless to say, improvements in technology are a matter of time, wherein, higher frequencies electronics might also be taken into account while designing new boards.

### *Gain fluctuations*

Usually, the hot/cold calibration (also called load-switch calibration) is applied in chirp transform spectrometers. Gain fluctuations, as the one produced by fluctuating environmental temperature, contributes to instabilities in the system. Consequently, these instabilities induce a shorter integration time according to the radiometer formula (Eq. 1.11). On the other hand, in case of a temperature-controlled environment, the design of the CTS is less sensitive to temperature variations. Similarly, a possible way to compensate these effects in microwave devices is by using pads with gain stabilization over temperature (Hartogh, priv. comm.). Nonetheless, small gain fluctuations are suggested to be analyzed in future investigations.

### *External energetic radiation*

Not all electronic circuits are suitable for aerospace applications, because they are susceptible to high energy irradiation with particles such as electrons, heavy ions, and protons. This is the case of most electronic devices in the 400-MHz bandwidth CTS. It is clear that in case of future space missions, a design with space-qualified devices (i.e. within space EMC standards) is eventually required.

### *Mass, power consumption, and vibration levels*

Limitations such as in mass, power consumption, and vibration levels are also established by space applications (i.e. in space missions). Actually, advances in technology such as the ones in the cellular-phone industry in RF processing and digital electronics may allow miniaturization of different stages in the CTS. As an example, full-custom ASIC designs enable compact size and thus mass, reduced power, and quiet operation. Usually, the ASIC designs yield to a reduced number of parts, easier assembly, and improved reliability. However, the main disadvantages are translated into higher sensitivity to radiation and an elevated cost.

## 2.7 Outlook

This chapter reviewed the development and complete characterization of a 400-MHz bandwidth and 100-kHz spectral resolution chirp transform spectrometer. The digital techniques used for the chirp signal generation were improved allowing a signal-to-noise-ratio (SNR) up to 50 dB. In addition, test results were obtained in atmospheric science and astronomical observation by integration of the spectrometer in a 142-GHz ozone system and by using the HHSMT observatory.

Considering the demand for broad bandwidth for various wavelengths spectroscopy, future development will concentrate on the following areas: (a) broader bandwidth SAW filters development and (b) high accuracy techniques with the aim of improving the performance of essential stages in the system. It must be stressed that the present sensitivity and resolution of the CTS can considerably widen different aspects studied currently in science. Therefore, it should be considered its inclusion on future space missions through the optimization of power consumption, size and weight.

Finally, the aim is to employ careful design choices, test measurements and advances in technology to ensure that new CTSs achieve a comparable or, which is always the main aim, better performance than previous chirp transform spectrometers (Paganini and Hartogh, 2006).



## 3 Impacts of nonlinearity in heterodyne systems

Vertical concentration profiles can be derived from the observed spectral radiances by fitting a radiative transfer model to the measurements. As these methods compare the observed radiances with the corresponding retrievals, for instance using a  $\chi^2$  minimization, any inconsistency between the model and the measurement will lead to inaccurate results. This is especially true for systematic errors in the measurements that do not match the random error levels. In contrast, when the systematic errors exceed the noise levels, they can be considered as spurious signals which if mistaken for atmospheric radiances, would lead to systematic errors on the derived profile. The instrumental errors can be subdivided into random and systematic errors; two types can be identified in each of these categories: those that affect the absolute values of the spectrum, and those that change the shape of the measured spectrum. The errors that affect the shape of the spectrum introduce altitude-dependent errors on the retrieved profile, whereas the errors on the absolute values of the spectrum directly introduce scaling effects in the retrieved profiles (Kleipool et al., 2000).

This chapter covers five major topics. The first section describes the physical properties of the Earth's atmosphere. Such a background is essential for discussing the errors on the derived profile from the measured spectra in planetary atmospheres. Section 3.2 focuses on a numerical calculation which demonstrates how considerable the effects are in the measured spectra in case of deviation from the heterodyne system's ideal linear dynamic range. In Section 3.3, numerical simulations show how such deviations in the spectra can produce significant changes in the retrieved vertical profile of trace gases. It should be emphasized that although the numerical analysis and simulations are focused on the Earth's atmosphere, such investigation may also apply to the atmospheres of other planets such as Venus and Mars. Section 3.4 mentions other instrumental errors, however, a deeper examination of these factors lies outside the scope of this thesis. Finally, possible implications of systematic errors into the vertical profile retrieval are discussed in Section 3.5.

### 3.1 Ground-based microwave spectroscopy of the Earth's atmosphere

#### 3.1.1 The atmosphere as physical system

The atmosphere consists of a mixture of ideal gases: although molecular nitrogen and molecular oxygen predominate by volume, minor constituents like carbon dioxide, ozone

and water vapor play crucial roles.

The atmosphere is continually illuminated by solar photons at infrared, visible and ultraviolet wavelengths. Some solar photons are scattered back to space by atmospheric gases or reflected back to space by clouds or the Earth's surface; some are absorbed by atmospheric molecules (especially water vapor and ozone) or clouds, leading to heating of parts of the atmosphere; and some reach the Earth's surface and heat it (Andrews, 2000). Also important is carbon dioxide ( $CO_2$ ) which, as the most important infrared absorbing, anthropogenic gas, has come to prominence in connection with the enhanced greenhouse effect. Through an understanding of the scattering, absorption, and emission behavior of atmospheric constituents, microwave remote-sensing techniques can be employed to monitor atmospheric parameters and weather conditions (Ulaby et al., 1981).

#### 3.1.2 Physical properties. Composition and structure

The atmosphere is the layer of gas surrounding a planet. On the Earth, the principal constituents are molecular nitrogen (78%), molecular oxygen (21%) and argon (0.93%). All the other species are much less abundant, i.e. their volume mixing ratio (vmr) is given in part per million (ppm), part per billion (ppb) or parts per trillion (ppt).

The atmospheric pressure and density decrease approximately exponentially with increasing height, as does the water-vapor density, although its variation with height is somewhat irregular and is strongly dependent on time of day, season, geographic location, and atmospheric activity. Applying the ideal gas law relating molecular concentration with pressure, it is shown that 90% of the mass of the atmosphere lies within the first lower 16 km layer, and 99.9% below 50 km. The variation of atmospheric temperature with height exhibits reversions of its gradient, which can be used to subdivide the Earth's atmosphere into a number of atmospheric layers according to their thermal structure. As a guide, Fig. 3.1 describes an average temperature profile (i.e. a 'standard' or 'reference' atmosphere) through the lower layers of the atmosphere according to the NOAA's National Weather Service (<http://www.srh.noaa.gov/jetstream/atmos/atmprofile.htm>).

As mentioned above, the boundaries of each atmospheric layer or shell are defined usually by the change in sign of the temperature gradient with height,  $dT/dz$ , where  $T$  is the atmospheric temperature and  $z$  is the geometrical height. The lowermost layer of the Earth's atmosphere is known as the troposphere, where most of what is called 'weather', e.g. cloud formation and precipitation, takes place. It is heated from below, and the ascending air expands with the decreasing pressure producing a cooling-down process. At its upper boundary, known as the tropopause,  $dT/dz$  changes abruptly to approximately zero.

The next layer above the tropopause is the stratosphere, which extends from the tropopause (12 km) to the stratopause (48 km). It is primarily heated by the absorption of solar UV radiation when ozone molecules are created and photodissociated.

The third layer, extending between the stratopause and the mesopause which altitude varies between 85 km in summer and 100 km during the rest of the season (see Berger and von Zahn, 1999), is the mesosphere. In this layer, the temperature decreases to the lowest value of the atmospheric temperature profile. This value, typically 173 K, occurs at the mesopause and can reach temperatures as low as 120 K (Seele and Hartogh, 1999). Together with the stratosphere, the region between 12 and 100 km is denoted as the middle

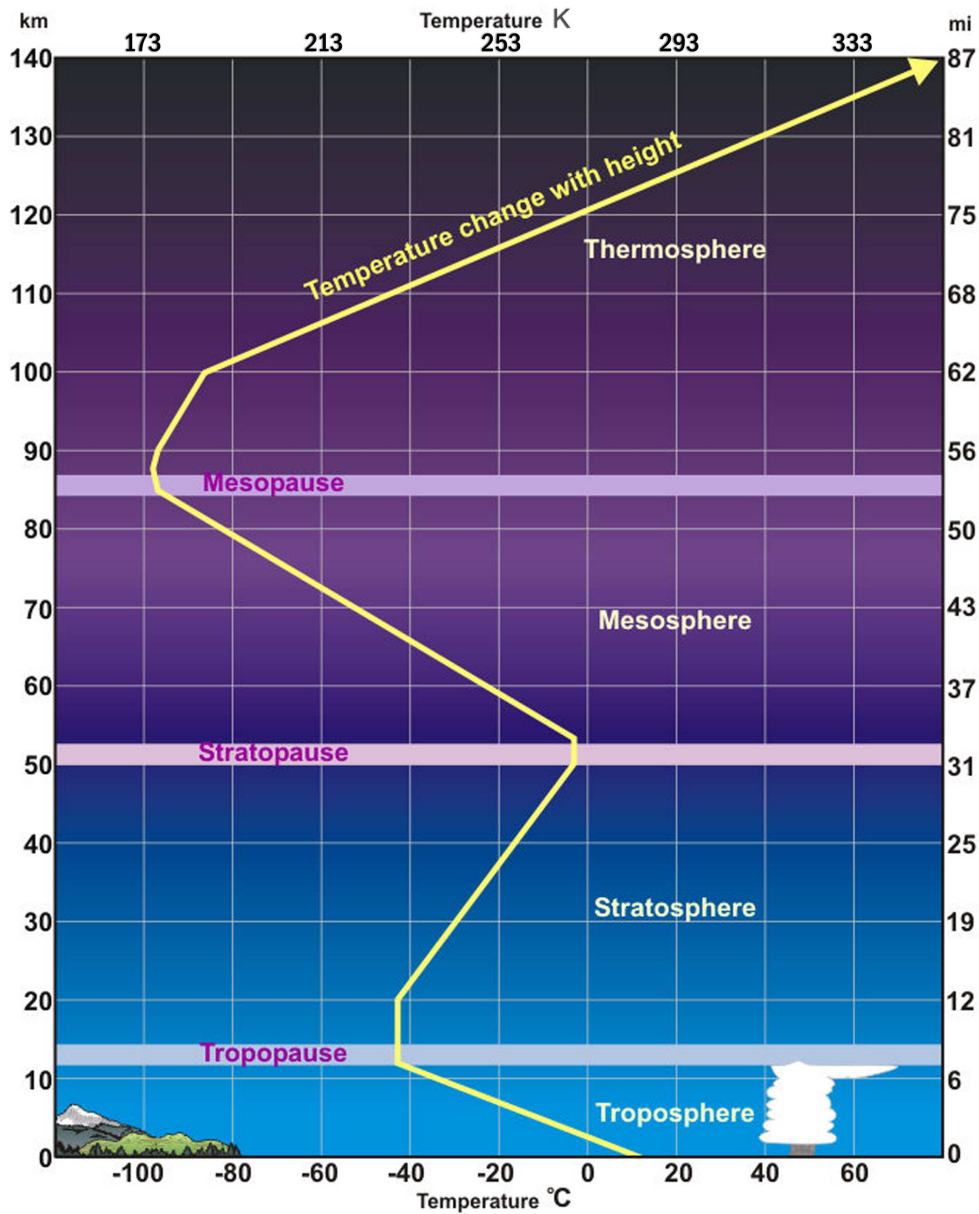


Figure 3.1: Standardized Temperature Profile (the Earth's atmosphere). An average temperature profile through the lower layers of the atmosphere (altitude vs. temperature). Source: NOAA's National Weather Service.

atmosphere and is of particular interest for microwave observations.

Above the mesopause, in the thermosphere, the density becomes very small and the composition changes due to dissociation and molecular fractionation (dependent on the molecular mass) make direct measurements of air temperature impossible.

### 3.1.3 Absorption and emission by gases

The total internal energy  $E$  of an isolated molecule consists of three types of energy states,

$$E = E_e + E_v + E_r, \quad (3.1)$$

where  $E_e$  = electronic energy,

$E_v$  = vibrational energy,

$E_r$  = rotational energy.

These energy states are quantized; they can assume discrete values that are specified by one or more quantum numbers. Radiation is absorbed (or emitted) when a transition takes place from a lower (or higher) energy state to a higher (or lower) energy state. The frequency  $\nu_o$  of absorbed (or emitted) quantum is given by the Bohr's formula,

$$\nu_o = \frac{E_m - E_l}{h}, \quad (3.2)$$

where  $h$  is the Planck's constant and  $E_m$  and  $E_l$  are the internal energies of the higher and lower molecular states, respectively. The transition may involve changes of electronic, vibrational, or rotational energy, or any combination of the three types. Transitions between pure rotational states (same  $E_e$  and  $E_v$  but different  $E_r$ 's) occur in the microwave and far-infrared portions of the spectrum. On the other hand, the large energy differences associated with electronic transitions usually result in complex band system in the visible and ultraviolet parts of the spectrum.

### 3.1.4 The shape of a spectral line

According to the preceding discussion, the absorption (or emission) spectrum of a molecule consists of sharply defined frequency lines corresponding to transitions between sharply defined (quantized) energy levels of the molecule (less than 1 Hz for a rotational transition, caused by natural broadening). Such a spectrum would be characteristic of an isolated, undisturbed, and stationary molecular system. In reality, however, the molecules are in constant motion, interacting and colliding with one another, and colliding with other material objects (such as dust particles). These disturbances cause the energy levels to vary in width. The increase in linewidth is called line broadening. Among the various sources of spectral line broadening (Townes and Schawlow, 1975, Gordy and Cook, 1970), pressure broadening, which arises from collisions between molecules, results in the shortening of the lifetime of the states involved in the transition and therefore the corresponding broadening effect. As this phenomenon is directly proportional to the pressure and therefore the altitude, the width of the line induced by pressure broadening can be used to retrieve the height information.

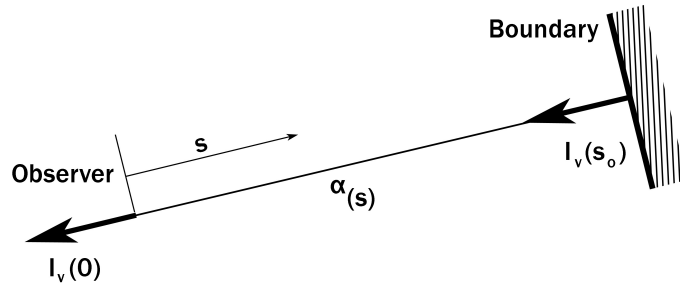


Figure 3.2: Measurement geometry for the passive remote sensing of atmospheres.

### 3.1.5 Theory of radiative transfer

The starting point for any passive remote-sensing application is the equation that describes the flow of radiant energy to be measured by a radiometer. The interaction between radiation and matter is described by two processes: extinction and emission, which theoretically is explained by the radiative transfer developed by Chandrasekhar (1960). And the variation of the intensity of electromagnetic radiation,  $I_\nu(s_0)$ , traversing a medium that absorbs, emits and scatters the radiation remotely measured by an instrument ( $s = 0$ ), e.g. planetary atmospheres, is provided by the radiative transfer equation through:

$$I_\nu(0) = I_\nu(s_0)e^{-\tau(s_0)} + \int_0^{s_0} \alpha B_\nu(T)e^{-\tau(s)} ds. \quad (3.3)$$

Its variation at a point 's' along a line in the direction of propagation is obtained by considering the sources and sinks of the radiation in a volume element along that line (Fig. 3.2), where ' $\alpha$ ' is the absorption coefficient and ' $\tau$ ' is the optical depth and is defined by:

$$\tau(s) = \int_0^{s_0} \alpha(s') ds'. \quad (3.4)$$

As mentioned in Chapter 1, in the (sub)millimeter-wave region under atmospheric conditions, there is  $h\nu \ll kT$ , known as Rayleigh-Jeans law. This allows to approximate the Planck's function in a mathematically simpler way (cf. Section 1.2.1),

$$B_\nu(T) \approx \frac{2\nu^2 kT}{c^2} = \frac{2kT}{\lambda^2}, \quad (3.5)$$

where  $h$  is Planck's constant,  $k$  is Boltzmann's constant,  $T$  is the temperature,  $c$  is the speed of light,  $\lambda$  is the wavelength, and  $\nu$  is the frequency.

Therefore, the brightness temperature [cf. Eq. (1.4)],  $T_B$ , is given as

$$T_B(\nu) = \frac{\lambda^2}{2k} I_\nu. \quad (3.6)$$

This formulation is convenient in millimeter-wave radiometry because the input power measured by a detector (from an incident radiation field) is proportional to this quantity, in degrees Kelvin. Using this last assumption, the radiative transfer equation becomes:

$$T_B(\nu) = T_{B_0}e^{-\tau(s_0)} + \int_0^{s_0} \alpha T(s)e^{-\tau(s)} ds, \quad (3.7)$$

where  $T_B(\nu)$  is the measured brightness temperature and  $T_{B_0}$  is the cosmic background.

### 3.1.6 Inversion technique

The forward model ' $F$ ' describes how the different atmospheric parameters affect the measured spectrum, determined by the physics of the radiative transfer through the atmosphere from the sources of emission to the observer. In general, ' $F$ ' is a non-linear function between the mixing ratio at a specific height and the measured spectrum. But it can be linearized under the assumption that the propagation occurs through an optically thin medium. It is also called the forward model (see Janssen, 1993). For the problem of ground-based remote sensing:

$$y_{(\nu)} = F(x_{(h)}, h) \quad (3.8)$$

where  $y_{(\nu)}$  denotes the measured signal as a function of frequency  $\nu$ , and  $x_{(h)}$  the mixing ratio as function of height,  $h$ .

The general problem of inverse techniques is how to derive information about ' $x$ ' from the measurement of ' $y$ '. Mathematically, this signifies the inverse of ' $F$ '. However, this is an ill-posed problem due to the underlying physics and always present noise on the measurement (Seele, 1999). The inversion problem seeks to determine the best representation of a required parameter providing spectral measurements and any appropriate prior information that may be available (about the atmosphere and the measuring device).

The inverse problem also involves topics related to understanding and describing the information content of the measurement, the relationship between the true state of the system and that retrieved using inverse methods, the error analysis of the overall measuring system and, finally, the optimization of observing systems and validation of results. In other words, the measurements do not provide the actual state of the atmosphere with independent errors, but only the best estimate derived from the measurements and a prior knowledge about the state of the atmosphere. Hence, the Optimal Estimation Method developed by Rodgers (1976) is used in order to analyze all these factors.

## 3.2 Numerical analysis

As explained in Chapter 1, the determination of the antenna temperature ( $T_A$ ) is conducted by means of a calibration measurement method. The precision of such measurement relies amongst others in how accurately the calibration load temperatures (hot and cold loads) are known as a function of frequency and how linearly the heterodyne system works. Hartogh (1989) also suggested the examination on how considerable the effects would become in case there is deviation from the spectrometer's ideal linear dynamic range (Fig. 3.3).

Nonlinearity characteristics are often characterized as either strongly nonlinear or weakly nonlinear. Although these terms have no precise definitions, a good working distinction is that a weakly nonlinear behavior can be described with adequate accuracy by a Taylor series expansion.

Considering that the temperature,  $T$ , is proportional to the measured power,  $P$ , (supplied by the spectrometer), the spectrometer's power gain can be approximated as a power series:

$$P = a_0 + a_1T + a_2T^2 + a_3T^3 + \dots \quad (3.9)$$

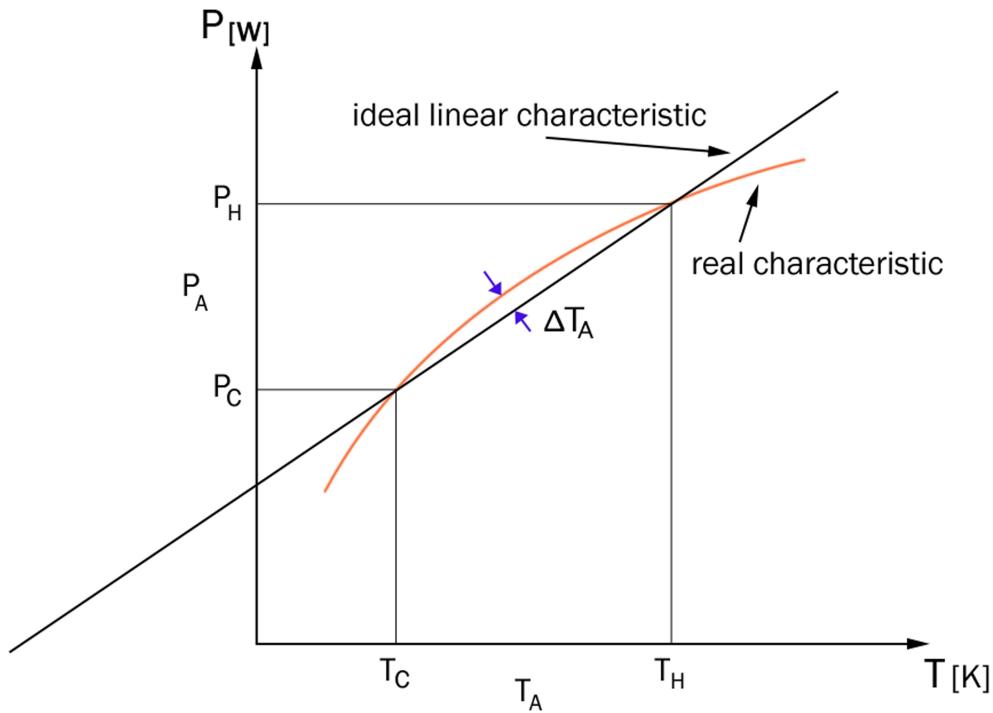


Figure 3.3: Calibration of antenna temperature in case there is a possible nonlinear response.

The measured antenna temperature can be calculated over the following calibration formula (ref. Eq. A.2):

$$T_A = \frac{P_A - P_C}{P_H - P_C}(T_H - T_C) + T_C, \quad (3.10)$$

where  $P_C = T_R + T_C$  and  $P_H = T_R + T_H$ .  $T_R$  is the receiver temperature.

The deviation from  $T_A$  can be calculated as:

$$\Delta T_A = T'_A - T_A, \quad (3.11)$$

in which  $T'_A$  represent the deviation from the ideal linear dynamic range.

Including a quadratic-order deviation from Eq. 3.9, i.e., a weakly nonlinear behavior represented by the second power of  $P = f(T)$ , giving

$$P'_A - P'_C = a_0 + a_1 T + a_2 T^2 - (a_0 + a_1 T_C + a_2 T_C^2) = a_1(T - T_C) + a_2(T^2 - T_C^2), \quad (3.12)$$

$$P'_H - P'_C = a_0 + a_1 T_H + a_2 T_H^2 - (a_0 + a_1 T_C + a_2 T_C^2) = a_1(T_H - T_C) + a_2(T_H^2 - T_C^2). \quad (3.13)$$

Therefore,  $T'_A$  becomes:

$$T'_A = \frac{a_1(T - T_C) + a_2(T^2 - T_C^2)}{a_1(T_H - T_C) + a_2(T_H^2 - T_C^2)}(T_H - T_C) + T_C. \quad (3.14)$$

Following,

$$\Delta T_A = \frac{a_1(T - T_C) + a_2(T^2 - T_C^2)}{a_1(T_H - T_C) + a_2(T_H^2 - T_C^2)}(T_H - T_C) + T_C - T \quad (3.15)$$

$$\Delta T_A = \frac{a_1(T - T_C) + a_2(T^2 - T_C^2)}{a_1 \frac{(T_H - T_C)}{(T_H - T_C)} + a_2 \frac{(T_H^2 - T_C^2)}{(T_H - T_C)}} - (T - T_C), \quad (3.16)$$

where by the property:

$$\frac{a^2 - b^2}{a - b} = a + b, \quad (3.17)$$

obtaining

$$\Delta T_A = \frac{(T - T_C) + \frac{a_2}{a_1}(T^2 - T_C^2)}{1 + \frac{a_2}{a_1}(T_H + T_C)} - (T - T_C) \quad (3.18)$$

and it ends, through some arithmetical steps, in:

$$\Delta T_A = \frac{\frac{a_2}{a_1}(T - T_H)(T - T_C)}{1 + \frac{a_2}{a_1}(T_H + T_C)}. \quad (3.19)$$

It can be noticed that  $\Delta T_A$  is zero for an ideal linear system. This implies  $\frac{a_2}{a_1} = 0$  and, respectively,  $T = T_C$  and  $T = T_H$  (i.e., in the calibration points).

The maximal deviation can be found by differentiation:  $\frac{d\Delta T_A}{dT} = 0$ . As a result, a maximum value of  $T = \frac{1}{2}(T_H + T_C)$  is obtained, which signifies the center between both calibration points.

A qualitative observation is that  $\Delta T_A$  can be considered as a 'Pseudo-Noise' of a measured spectrum. Thus,  $\Delta T_A$  might represent different nonlinearities in the spectrometer's linear dynamic range.

The only unknown is the ratio  $\frac{a_2}{a_1}$  which cannot be estimated. Nevertheless, the deviation from linearity can be measured through the so-called factor 'r':

$$r = \frac{P - P(0)}{P_{lin} - P(0)} \quad (3.20)$$

whereby  $P_{lin}$  would represent the case of an ideal linear characteristic.

Eq. 3.9 can be used to represent:

$$P - P(0) = a_1 T + a_2 T^2 \quad (3.21)$$

and thus

$$P_{lin} - P(0) = a_1' T, \quad (3.22)$$

where  $a_1' = \frac{P_H - P_C}{T_H - T_C}$  represents the system-gain factor.

Again, if quadratic terms are considered through Eq. 3.9:

$$P_H - P_C = a_1(T_H - T_C) + a_2(T_H^2 - T_C^2), \quad (3.23)$$

these lead to

$$a_1' = \frac{a_1(T_H - T_C) + a_2(T_H^2 - T_C^2)}{T_H - T_C} = a_1 + \frac{a_2(T_H^2 - T_C^2)}{T_H - T_C} \quad (3.24)$$

$$= a_1 + a_2(T_H + T_C). \quad (3.25)$$

Therefore, Eq. 3.20 becomes

$$r = \frac{a_1 T + a_2 T^2}{T[a_1 + a_2(T_H + T_C)]} = \frac{a_1 T + a_2 T^2}{a_1 T + a_2 T(T_H + T_C)} = \frac{1 + \frac{a_2}{a_1} T}{1 + \frac{a_2}{a_1}(T_H + T_C)} \quad (3.26)$$

and

$$\frac{a_2}{a_1} = \frac{1 - R}{R(T_H + T_C) - T}, \quad (3.27)$$

where  $R \equiv r_{max}$  in  $T = \frac{1}{2}(T_H + T_C)$ . Hence, the result of including Eq. 3.27 in Eq. 3.19 is:

$$\Delta T_A = \frac{\frac{(1-R)}{R(T_H+T_C)-T}(T - T_H)(T - T_C)}{1 + \frac{(1-R)}{R(T_H+T_C)-T}(T_H + T_C)} = \frac{\frac{(1-R)}{R(T_H+T_C)-T}(T - T_H)(T - T_C)}{\frac{R(T_H+T_C)-T+(1-R)(T_H+T_C)}{R(T_H+T_C)-T}}, \quad (3.28)$$

$$= \frac{(1 - R)(T - T_H)(T - T_C)}{T_H + T_C - T}. \quad (3.29)$$

In here, it can be defined a 'Signal to Pseudo-Noise Ratio' (SPNR) as

$$SPNR = \frac{T_L}{\Delta T_A}, \quad (3.30)$$

where  $T_L = T - T_C$ . Thus,  $T_L$  represents temperature values within the linear dynamic range.

As a rule of thumb, the measured spectral line in microwave wavelengths must be known with a precision of better than 0.1%. Therefore, this suggests that inaccuracies in the measured spectral line may introduce uncertainties in the volume mixing ratio retrieval. However, two conditions can be established in order to minimize such effects: a) a minimum integration time between calibration loads, and b) a  $SPNR > 1000$ .

The following formula can be obtained through some arithmetical steps

$$R = 1 - \frac{T_L(T_H + T_C - T)}{(T - T_H)(T - T_C)SPNR}, \quad (3.31)$$

which yields to calculate the maximal allowed value for R.

Typically, two nonlinear regions can be identified in a spectrometer's linear dynamic range. One is the lower part which describes the inherent noise floor of the CTS, meanwhile the other is the upper part which describes the gain compression. Therefore, smaller values of 'r' should be expected within these two regions. That implies the middle of the linear range of the curve. Depending on the linear characteristics, the linear dynamic range would extend within values of  $r < 1.26$ . Indeed, radiometric measurements, which operate between hot and cold loads, occupy a region in the complete linear dynamic range equal to 7 dB (depending on the advances in technology). Therefore, the larger the linear dynamic range, the better the linearity characteristics of a given system.

It can be demonstrated that considerable errors may appear due to nonlinearity for small values of  $T_L$  and a certain SPNR. For instance, from Eq. 3.31, it can be determined that for  $SPNR > 1000$  and  $T_L = 1$ , the required R should be at least smaller than 1.0036.

The expected deviations produced in the linear dynamic range (i.e.,  $\Delta T_A$ ) can be determined for different values of  $T_L$ . In that case, it is known that  $T = T_L + T_C$ , so replacing in Eq. 3.29:

$$\Delta T_A = \frac{(1 - R)(T_L + T_C - T_H)(T_L + T_C - T_C)}{T_H + T_C - (T_L + T_C)} = \frac{(1 - R)(T_L + T_C - T_H)T_L}{T_H - T_L}. \quad (3.32)$$

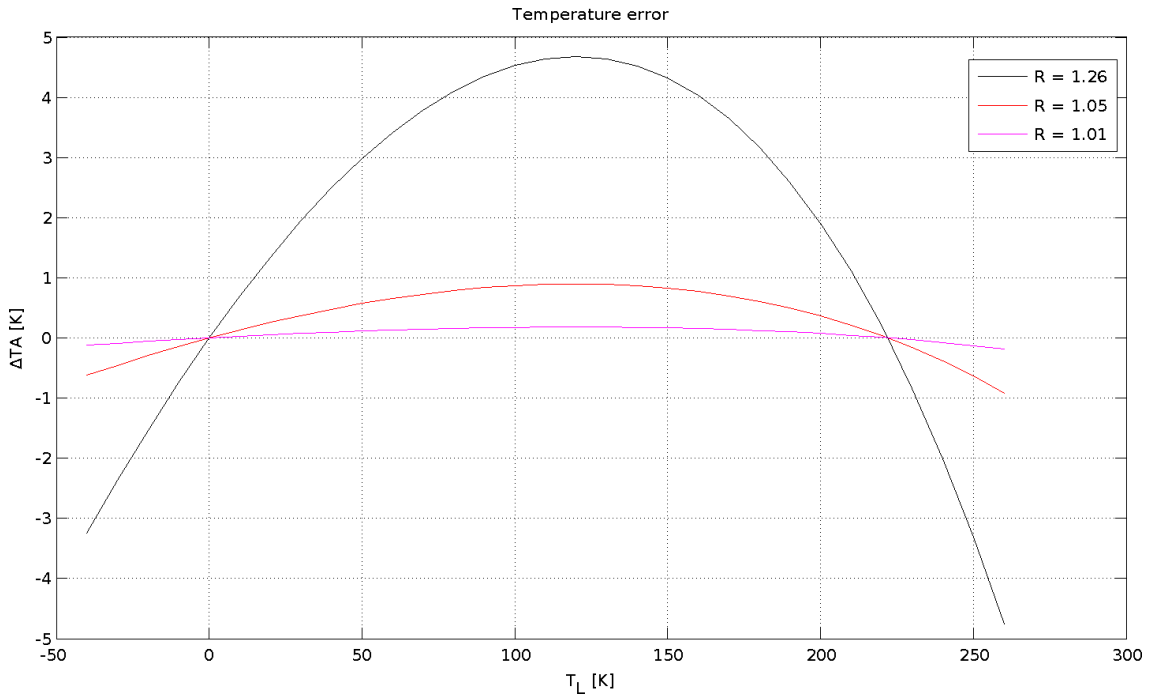


Figure 3.4: Deviations ( $\Delta T_A$ ) for different values of  $T_L$  which might appear in case of three different levels of nonlinearity:  $R$  equal to 1.26, 1.05 and 1.01. The calculations are done for a 142-GHz Ozone Radiometer (Hartogh and Jarchow, 1995).

Following on, Table 3.1 displays  $\Delta T_A$  for different values of  $T_L$  which might appear in case of three different deviation levels from linearity:  $R$  equal to 1.26 (26%), 1.05 (5%) and 1.01 (1%). However, it should be mentioned that the deviation values produced at  $R = 1.26$  might be probably bigger due to higher coefficients (such as  $a_3$ ) as a result of strong compression effects. These calculations are implemented for a 142-GHz ozone radiometer with a receiver temperature  $T_R = 500$  K, a 78 K liquid-nitrogen cold load and a hot load at 300 K, i.e.  $T_C = 578$  K and  $T_H = 800$  K respectively, as the one operated at MPS in Katlenburg-Lindau (Hartogh and Jarchow, 1995). As a conclusion, this study is consistent with Hartogh (1989) suggesting major deviations for higher values of  $R$ , and thus higher erratic behavior. As represented in Fig. 3.4, null deviation should be expected for values close to the calibration load temperatures ( $T_C$  and  $T_H$ ), but on the other hand, large errors in the middle of the deviation curve. In practice, radiometric measurements are intended to be operating where deviations are kept to a minimum, i.e., within the highest linear region of the linear dynamic range.

The current development of heterodyne systems achieves low values of receiver temperatures ( $T_R$ ) thank to advances in technology, such as in the employment of low-noise SIS (Superconductor-Insulator-Superconductor) detectors and InP HEMT amplifiers. Such achievements represent an improvement in the receiver sensitivity of the atmospheric detected signal, but it should be also emphasized that these improvements signify an increase in the sensitivity to errors according to Eq. 3.32. For these reasons, highly accurate methods for nonlinearity detection, i.e. less uncertainty, provide the chance of nonlinear processes investigation and the study of possible suppression of their sources. In such a case, this leads to better data quality which is translated on better reliability of planetary

Table 3.1: Calculated temperature deviations in case of nonlinearity

$T_L$ [K]	$\Delta T_A(R = 1.26)$ [K]	$\Delta T_A(R = 1.05)$ [K]	$\Delta T_A(R = 1.01)$ [K]
-40	-3.24	-0.62	-0.124
-30	-2.37	-0.46	-0.090
-20	-1.53	-0.3	-0.058
-10	-0.74	-0.14	-0.028
-5	-0.37	-0.07	-0.014
-2	-0.15	-0.03	-0.006
-1	-0.07	-0.01	-0.003
0	0	0	0.000
1	0.07	0.01	0.003
2	0.14	0.03	0.005
5	0.35	0.07	0.014
10	0.7	0.13	0.027
20	1.35	0.26	0.051
30	1.94	0.37	0.074
40	2.49	0.48	0.095
50	2.98	0.57	0.114
60	3.42	0.66	0.130
70	3.79	0.73	0.144
80	4.1	0.79	0.156
90	4.35	0.84	0.166
100	4.53	0.87	0.173
120	4.68	0.9	0.178
130	4.64	0.89	0.177
140	4.52	0.87	0.172
150	4.32	0.83	0.164
160	4.03	0.78	0.153
170	3.65	0.7	0.139
180	3.17	0.61	0.121
190	2.59	0.5	0.099
200	1.91	0.37	0.073
210	1.11	0.21	0.042
221	0.1	0.02	0.004
222	0	0	0.000
223	-0.1	-0.02	-0.004
230	-0.84	-0.16	-0.032

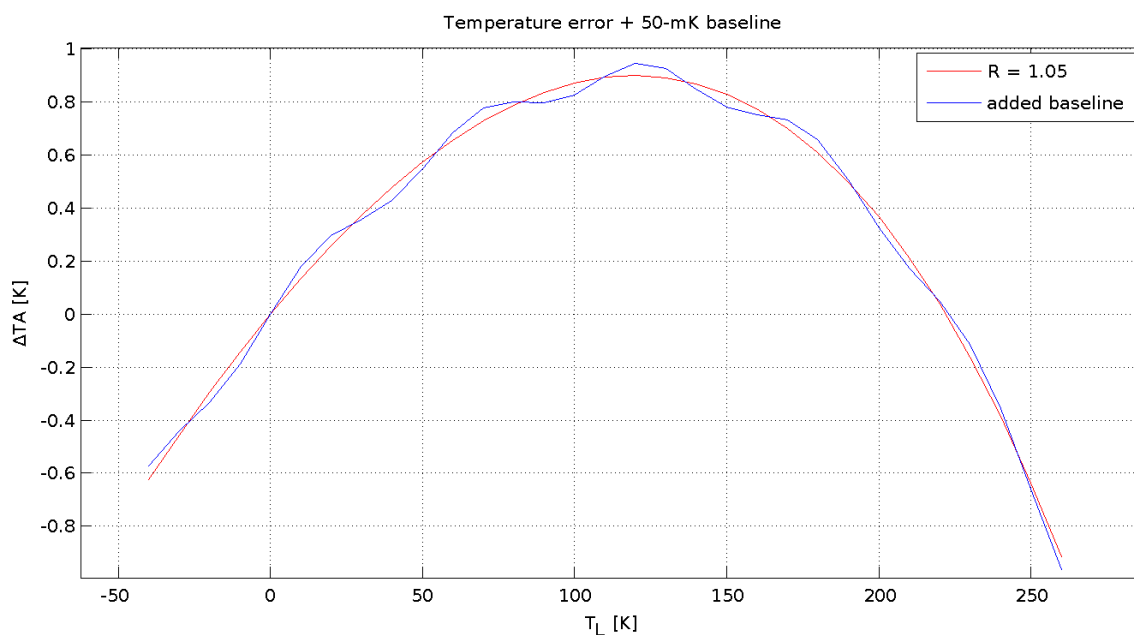


Figure 3.5: Variations produced by a 50-mK standing wave for  $R = 1.05$ .

atmospheric measurements.

Usually, the calibration method does not remove all the instrumental errors from the measurement. In general, standing waves are caused by reflections on two parallel surfaces in the internal transmission path such as in quasi-optical systems or reflections in semirigid IF cabling. An evidence of standing waves are sine-shaped structures superimposed on the measured spectrum. If these standing waves are taken into account, it would denote an increase in the previously calculated deviations. As an example, Fig. 3.5 shows variations produced by a 50-mK standing wave for the case in which  $R = 1.05$ .

### 3.3 Simulations on the Earth's atmosphere

The previous section has presented a numerical calculation which demonstrates how considerable the deviations are from the heterodyne system's (ideal) linear dynamic range. This section focuses on a simulation analysis which attempts to show how such deviations in the spectra may produce significant changes in the retrieved vertical profile (for instance in the Earth's atmosphere).

The following investigation illustrates the effects of line amplitude deviations by producing arbitrary variations in both the line center and wings of a generated synthetic ozone spectrum. The aim is to account for the effects of such deviations in the synthetic spectrum by observing changes in the retrieved vertical profile. In here, the profiles are retrieved by using the Optimal Estimation Method (OEM) of Rodgers (1976) using an existing radiative transfer model (Jarchow and Hartogh, 1995, Jarchow, 1998).

In a real case scenario, an analogy of line center deviations could be established by observing the day-nighttime variation of ozone where there exists an increase of the volume mixing ratio in the mesosphere during nighttime. The diurnal variation of ozone results from the three-body reaction of ozone ( $O_3$ ) from atomic oxygen (O) and molecular oxy-

gen ( $O_2$ ), which is no longer balanced by the reverse process of photodissociation of  $O_3$  into O and  $O_2$  in the nightside atmosphere. This imbalance leads to a diurnal variation of  $O_3$  above ~50-km altitude, where the daytime abundance of O is sufficient to contribute a noticeable increase in the nighttime  $O_3$  abundance (Allen et al., 1984, Connor et al., 1994, Zommerfelds et al., 1989, Sonnemann et al., 2007).

The starting point of the following examples (Figs. 3.6-3.13) is an arbitrary chosen mixing ratio profile of ozone where the synthetic radiance data are generated by a forward calculation model. After applying different degrees of deviations in the line center (Figs. 3.6-3.9) and wings (Figs. 3.10-3.13) of the synthetic ozone spectrum, the ozone's volume mixing ratio is reconstructed by an inversion technique using the OEM (figures are located at the end of this chapter).

As a result, this investigation suggests that deviations in the line center of the ozone's spectral information may produce erratic results in the lower mesosphere and upper stratosphere; meanwhile deviations in the wings determine aberration in the lower stratosphere of the Earth's atmosphere. Therefore, it is clear that small effects of nonlinearity in the spectra, as those created by power amplitude deviations, may lead to erratic results in the retrieved volume mixing ratio. For instance, while detecting some molecular species in the mm- and submm-wavelength range in planetary atmospheres.

As an extension of this analysis, studies such as by Kleipool et al. (2000), de La Noë (1998), Kuntz et al. (1997), Seele (1999) analyze other typical instrumental source of errors for a passive heterodyne system; e.g., image sideband contribution, continuum emission, random noise and standing wave. In practice, these error sources also induce uncertainties in the derived atmospheric information. However, a deeper evaluation of such sources lies outside the scope of this thesis.

## 3.4 Other sources of instrumental error

In the previous section, a series of simulations showed that the volume mixing ratio retrieval may be affected by different instrumental errors; for instance, amplitude shifts in the spectra produced by: standing waves, excessive instrumental noise over the baseline or quadratic components in the calibration line. Nevertheless, these are not the only instrumental uncertainties affecting the radiometric system. Kleipool et al. (2000) described a number of typical uncertainties for a passive heterodyne sounder and their effects on the retrieved ozone vertical profile. Therefore, some of the most common sources of instrumental uncertainties are mentioned in this section.

### 3.4.1 Sky window

The reflectance of the window causes ambient radiation to be directed into the receiver input, this results in standing waves that manifest themselves as spectral disturbances on the measurement. If it is a fast function, it can be seen as a ripple on the measurement; when it is a slow function, it can result in a baseline tilt (Keen et al., 1995). These standing waves are substantially reduced by a path-length modulator, mounted directly behind the switching mirror, which reduces the effects of standing waves by continuous alteration of

the total path length through the receiver (Kleipool et al., 2000). However, small standing waves can still occur (see Kuntz et al., 1997).

#### 3.4.2 Reference loads

The calibration loads, made of ferrite-load foam, are not perfect blackbodies; for instance, the additional reflections created on the liquid nitrogen interface and dew formation and frost on the load itself. Therefore, the loads reflect part of the ambient radiation into the receiver input, resulting in an underestimated gain. The associated uncertainties cause scaling errors on the absolute values of the measured spectrum.

#### 3.4.3 Single sideband filter

The separation of the image response of the mixer is usually performed by a Martin-Puplett Interferometer (MPI), which separates the sidebands. The unwanted sideband is absorbed in a sideband termination load, being cooled to 80 K in a dewar (Hartogh and Jarchow, 1995). The filter is needed to suppress emission from the image sideband, which would otherwise contaminate the measurement. Nevertheless, a small contribution of this image sideband can be introduced to the measurements while measuring strong emissions, e.g., ozone. Depending on the shape of the signal in the image band the contribution to the spectrum results in a systematic frequency-dependent baseline.

### 3.5 Discussion

The specific retrieval algorithm, used to derive vertical profiles from emission spectra (measured by a microwave system), is sensitive to instrumental noise and errors. Clearly, random noise on the spectrum increases the error bars on the retrieved profile and reduces the vertical resolution, whereas systematic errors in the line strength lead to scaling errors on the profile or even completely wrong profiles in case of baseline ripples. If the errors are overestimated not all the information can be retrieved from the measurement; if the error is underestimated, noise can be considered as spectral features and would contribute spurious signals to the retrieved profile (Kleipool et al., 2000).

Even though many systematic errors are corrected by the calibration algorithm, scaling uncertainties can be expected to arise from: the sky windows, whose transmission is an unknown function of the temperature, or even the reflectivity of the cold load and the single sideband filter. These phenomena can produce small undesired effects such as standing waves, baseline tilt or baseline ripples. An extensive study of the information content of ground-based microwave measurements has been presented by Brillet (1989). Some of these effects have been taken into account as extensions of retrieval methods like the Optimal Estimation Method (OEM) or the Constrained Linear Inversion (CLI) giving successful results (see Kuntz et al., 1997, Seele, 1999). However, such extensions do not include the effect of possible amplitude deviations of the power spectral density, for instance due to nonlinearity as demonstrated in Section 3.2.

Presently, detectors in heterodyne spectroscopy (e.g., SIS technology) increasingly involve lower radiometric noises. As a result, all other instrumental uncertainties must

be reduced below this noise level in order to keep the overall system's precision. Not surprisingly, this implies that state-of-the-art detectors not only are more sensitive to atmospheric signals (due to low radiometric noise), but also to erratic behavior which thus denotes major deviations from a true brightness temperature value (see Eq. 3.32).

As a conclusion, it is demonstrated the need to detect nonlinear effects with very low uncertainty (i.e.,  $< 0.1\%$ ) in order to identify and eliminate any possible kind of instrumental error sources. On the worst-case scenario, if systematic errors produced by nonlinearity can be detected but not eliminated, they should be included additionally as measurement errors in the retrieval algorithm.

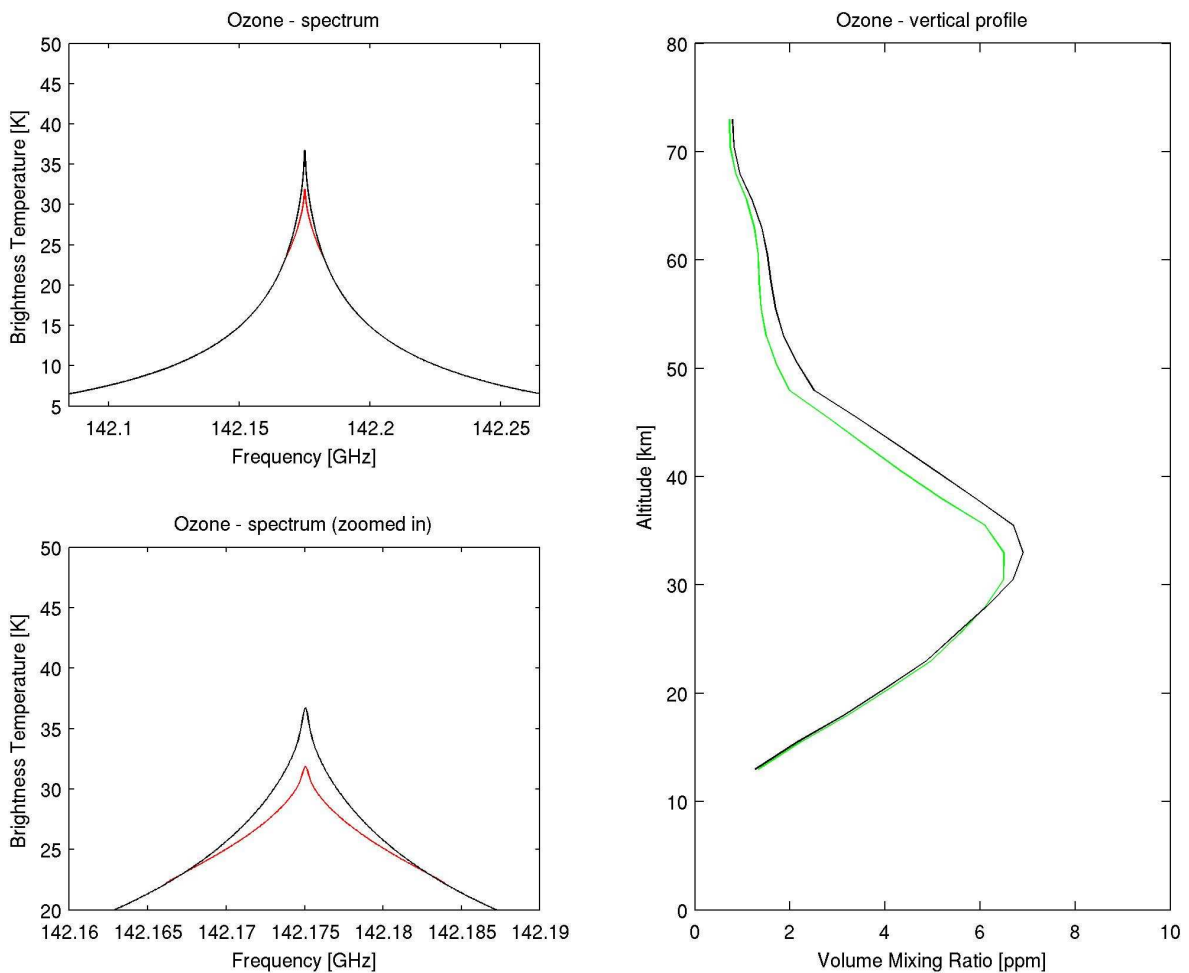


Figure 3.6: Effects of small deviations in the spectral intensity of a synthetic spectrum. Left top panel: synthetic spectrum (black) and a subtracting 5-K spectral intensity deviation over the line center (red). Left bottom panel: zoomed-in plot of the synthetic spectrum (black) and applied deviation of the spectral intensity (red). The right panel shows the retrieved profile obtained from inverting the synthetic original data (black) and the results after adding intensity deviations in the spectrum (green).

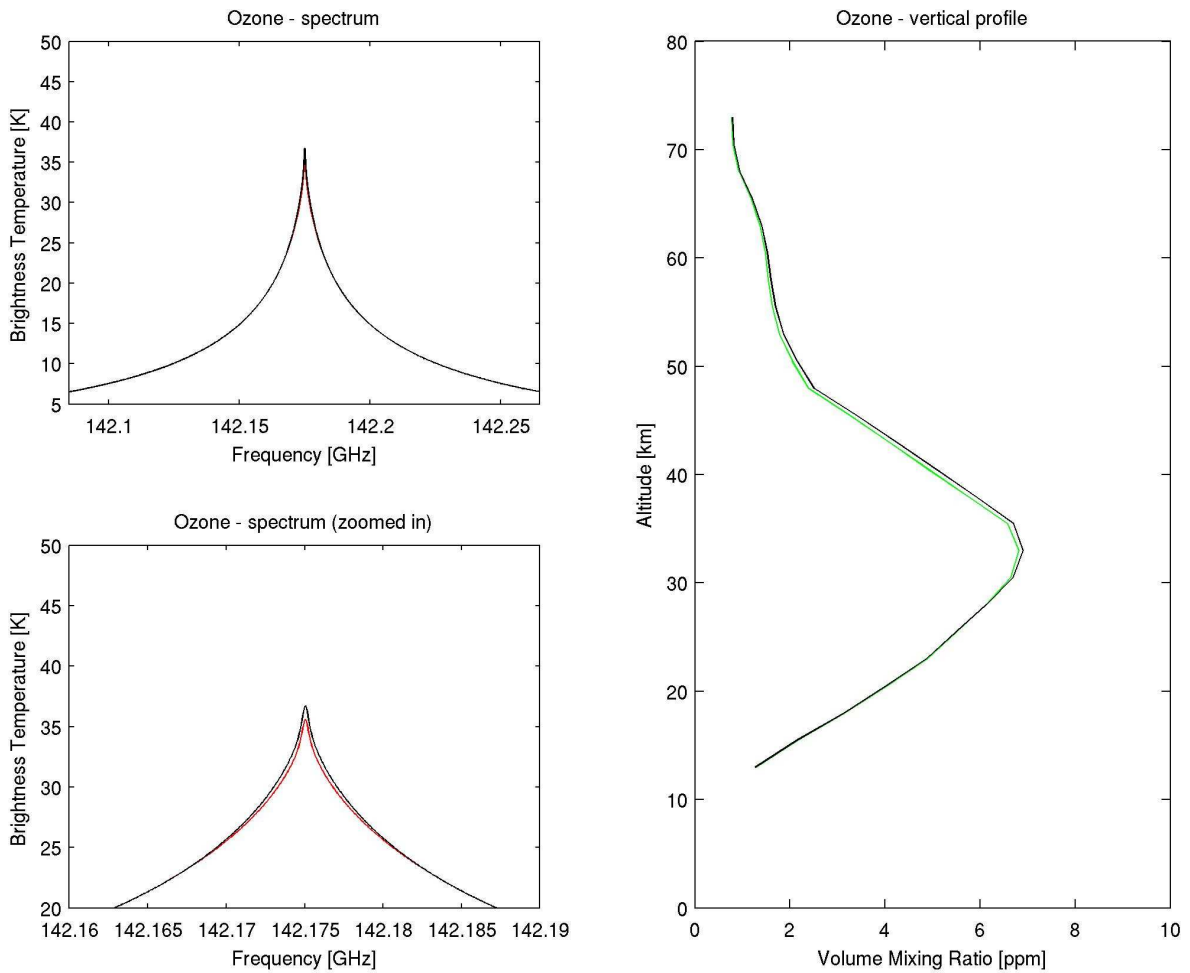


Figure 3.7: Effects of small deviations in the spectral intensity of a synthetic spectrum. Left top panel: synthetic spectrum (black) and a subtracting 1.5-K spectral intensity deviation over the line center (red). Left bottom panel: zoomed-in plot of the synthetic spectrum (black) and applied deviation of the spectral intensity (red). The right panel shows the retrieved profile obtained from inverting the synthetic original data (black) and the results after adding intensity deviations in the spectrum (green).

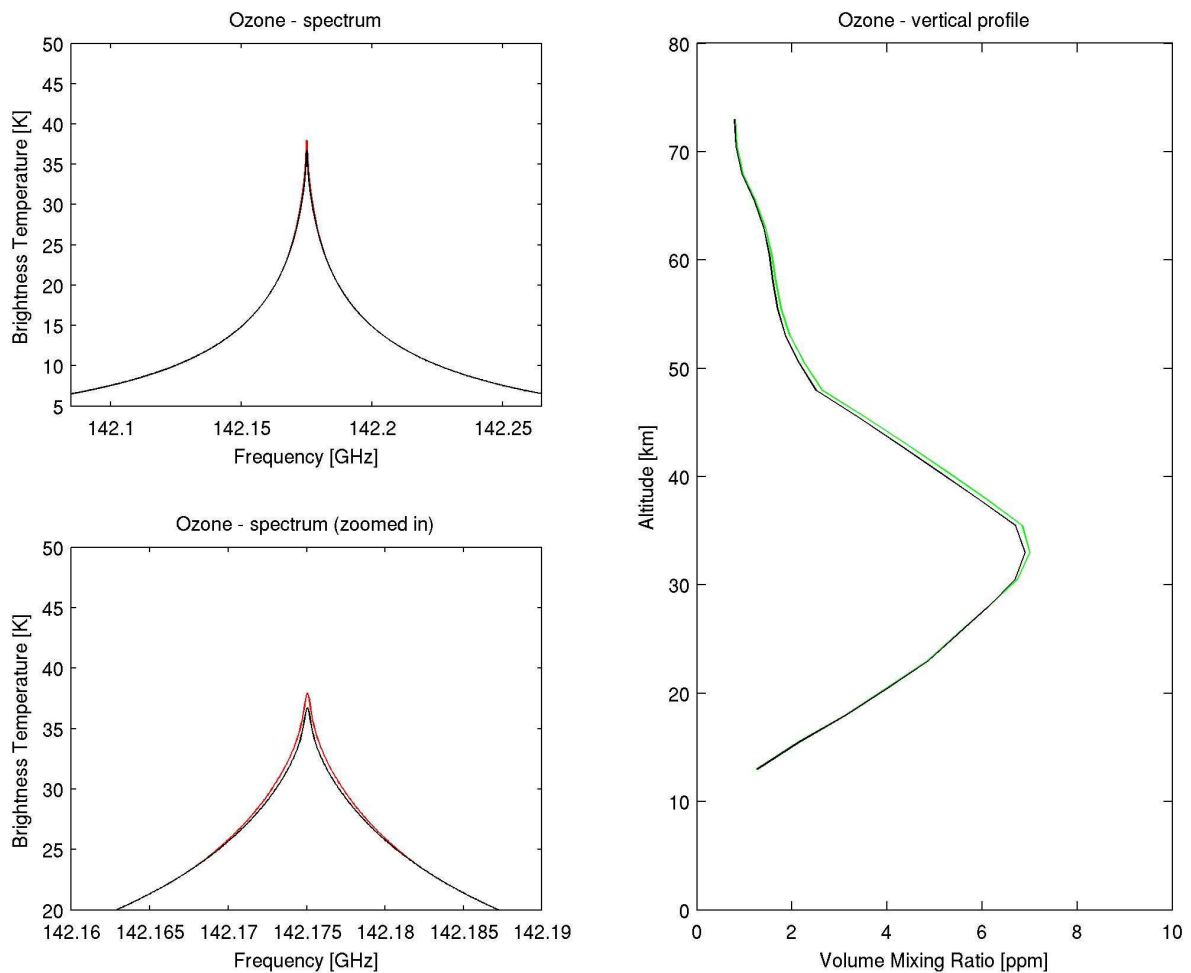


Figure 3.8: Effects of small deviations in the spectral intensity of a synthetic spectrum. Left top panel: synthetic spectrum (black) and an adding 1.5-K spectral intensity deviation over the line center (red). Left bottom panel: zoomed-in plot of the synthetic spectrum (black) and applied deviation of the spectral intensity (red). The right panel shows the retrieved profile obtained from inverting the synthetic original data (black) and the results after adding intensity deviations in the spectrum (green).

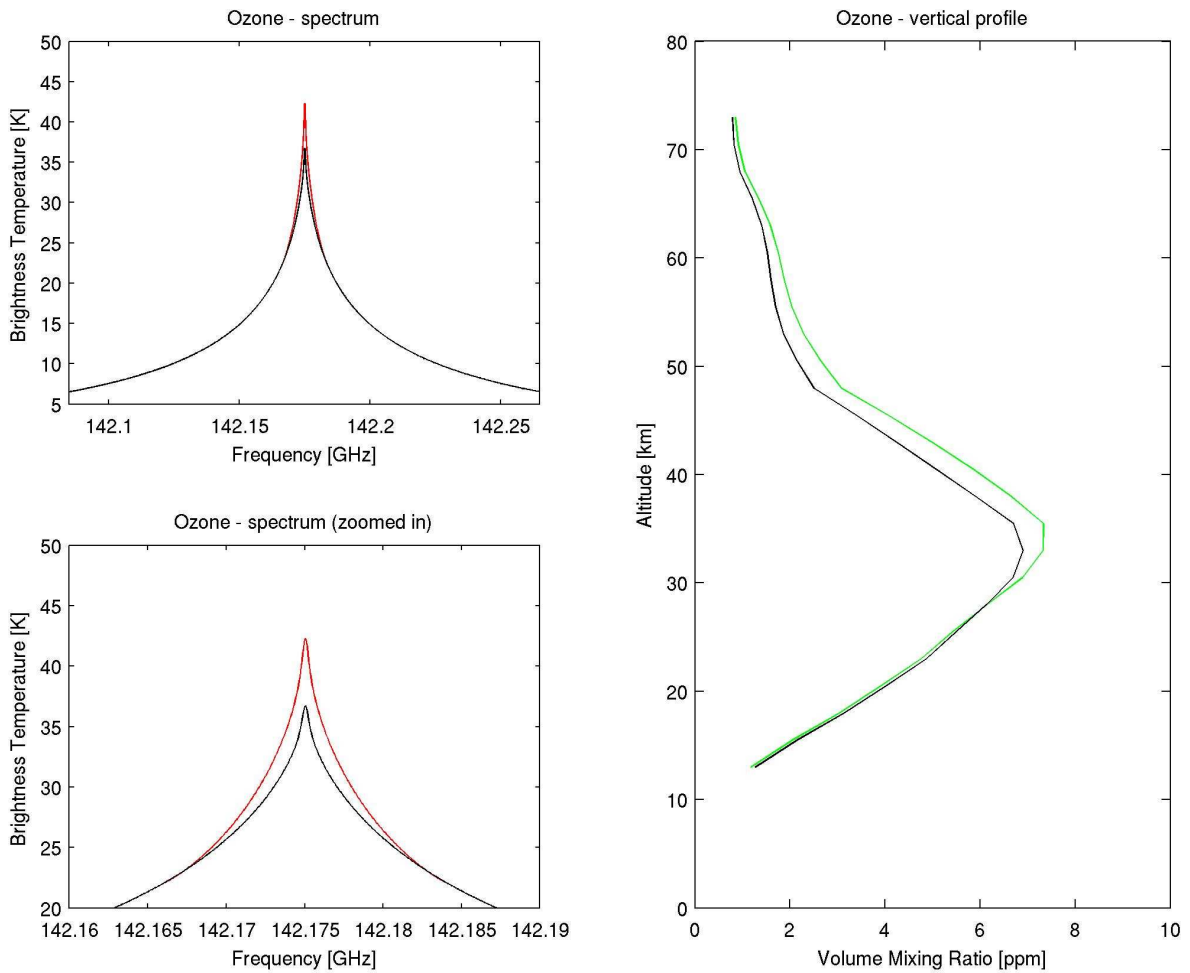


Figure 3.9: Effects of small deviations in the spectral intensity of a synthetic spectrum. Left top panel: synthetic spectrum (black) and an adding 5-K spectral intensity deviation over the line center (red). Left bottom panel: zoomed-in plot of the synthetic spectrum (black) and applied deviation of the spectral intensity (red). The right panel shows the retrieved profile obtained from inverting the synthetic original data (black) and the results after adding intensity deviations in the spectrum (green).

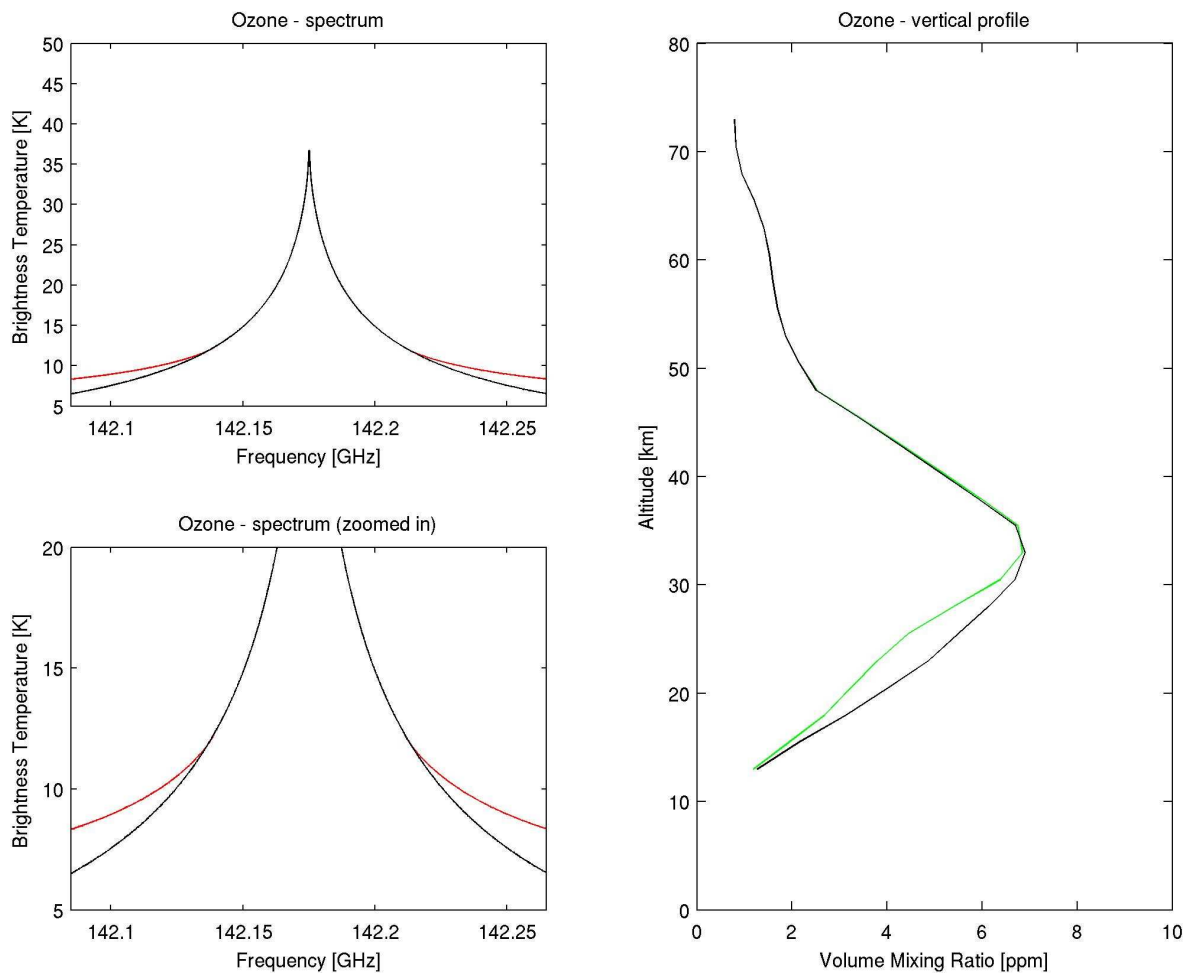


Figure 3.10: Effects of small deviations in the spectral intensity of a synthetic spectrum. Left top panel: synthetic spectrum (black) and an adding 1.9-K spectral intensity deviation over the wings (red). Left bottom panel: zoomed-in plot of the synthetic spectrum (black) and applied deviation of the spectral intensity (red). The right panel shows the retrieved profile obtained from inverting the synthetic original data (black) and the results after adding intensity deviations in the spectrum (green).

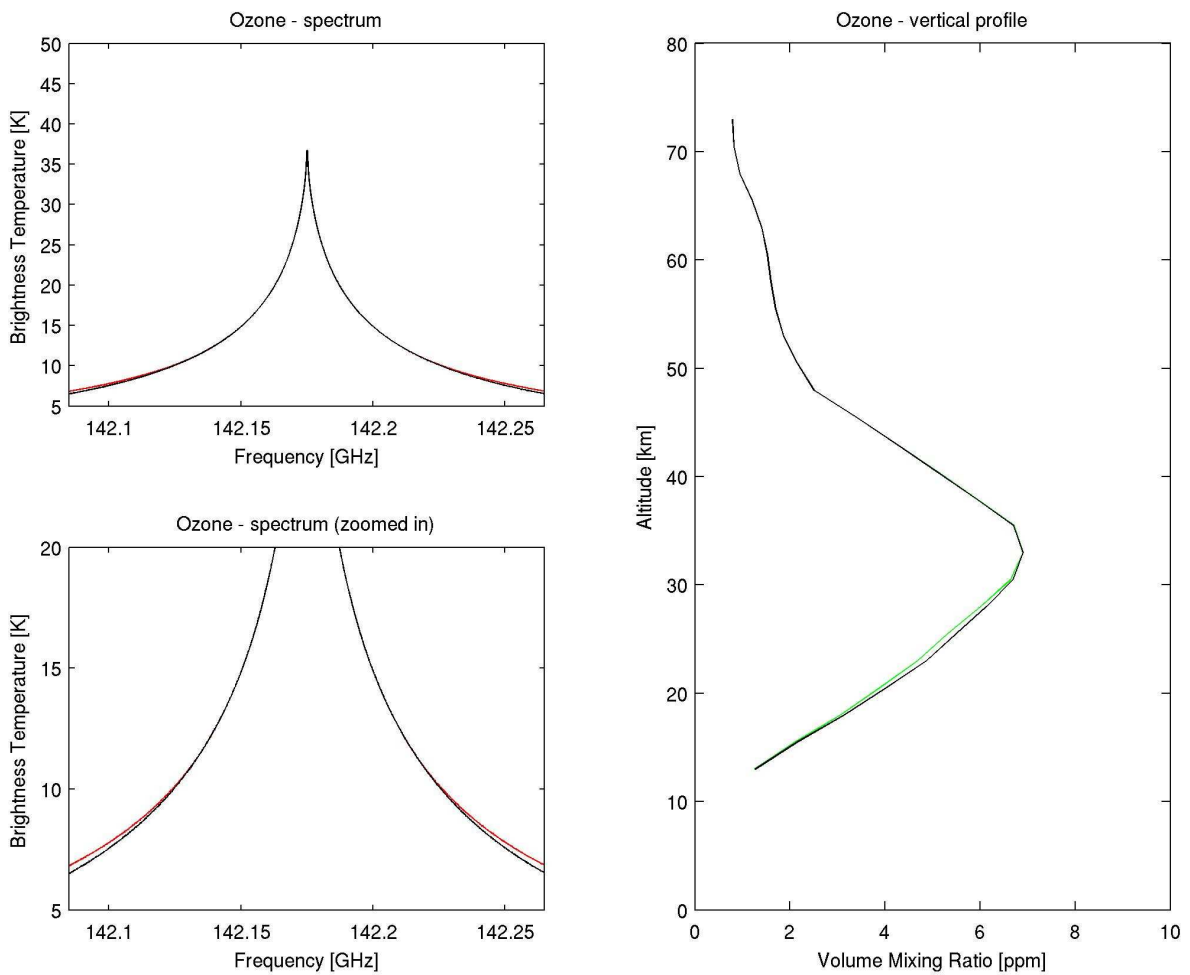


Figure 3.11: Effects of small deviations in the spectral intensity of a synthetic spectrum. Left top panel: synthetic spectrum (black) and a subtracting 0.4-K spectral intensity deviation over the wings (red). Left bottom panel: zoomed-in plot of the synthetic spectrum (black) and applied deviation of the spectral intensity (red). The right panel shows the retrieved profile obtained from inverting the synthetic original data (black) and the results after adding intensity deviations in the spectrum (green).

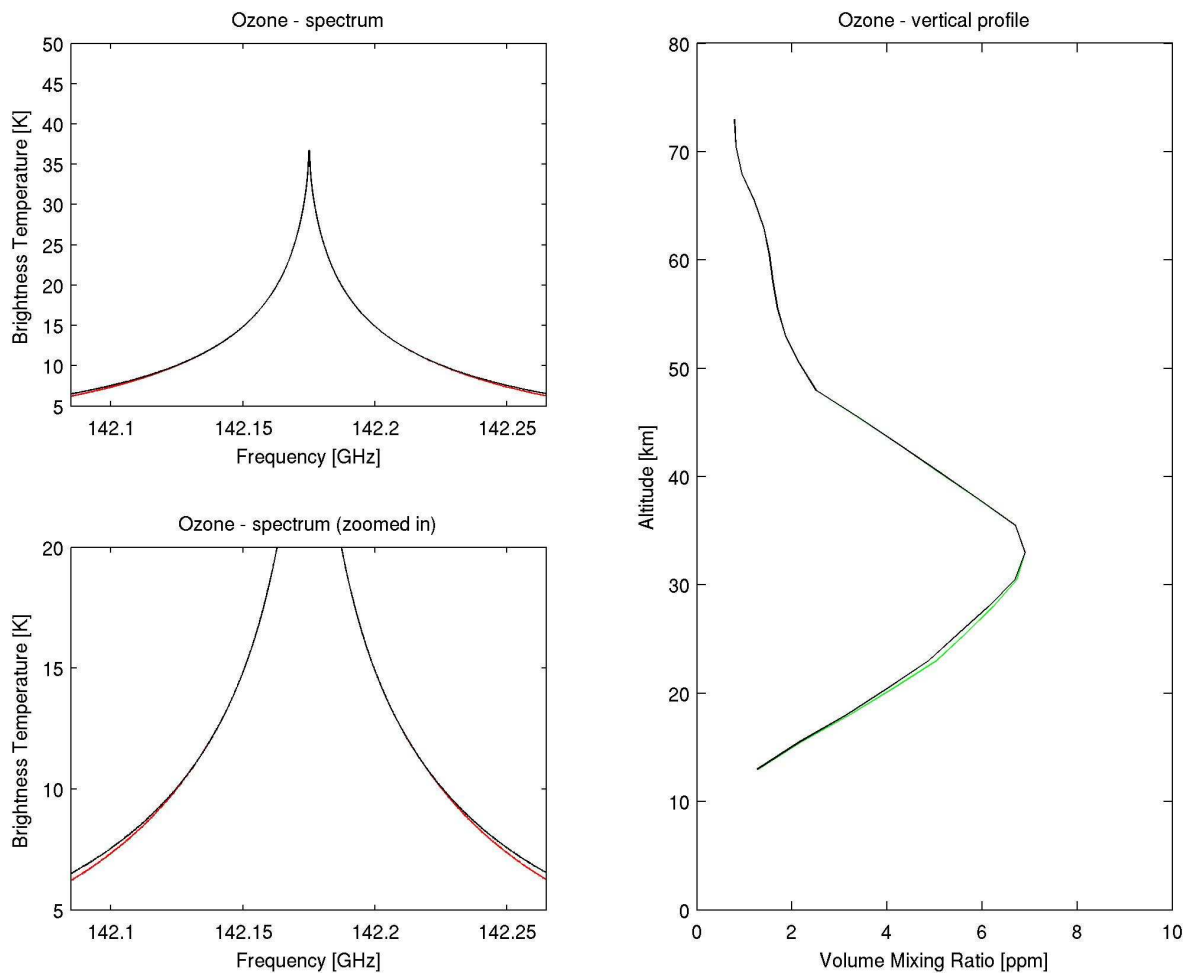


Figure 3.12: Effects of small deviations in the spectral intensity of a synthetic spectrum. Left top panel: synthetic spectrum (black) and a subtracting 0.4-K spectral intensity deviation over the wings (red). Left bottom panel: zoomed-in plot of the synthetic spectrum (black) and applied deviation of the spectral intensity (red). The right panel shows the retrieved profile obtained from inverting the synthetic original data (black) and the results after adding intensity deviations in the spectrum (green).

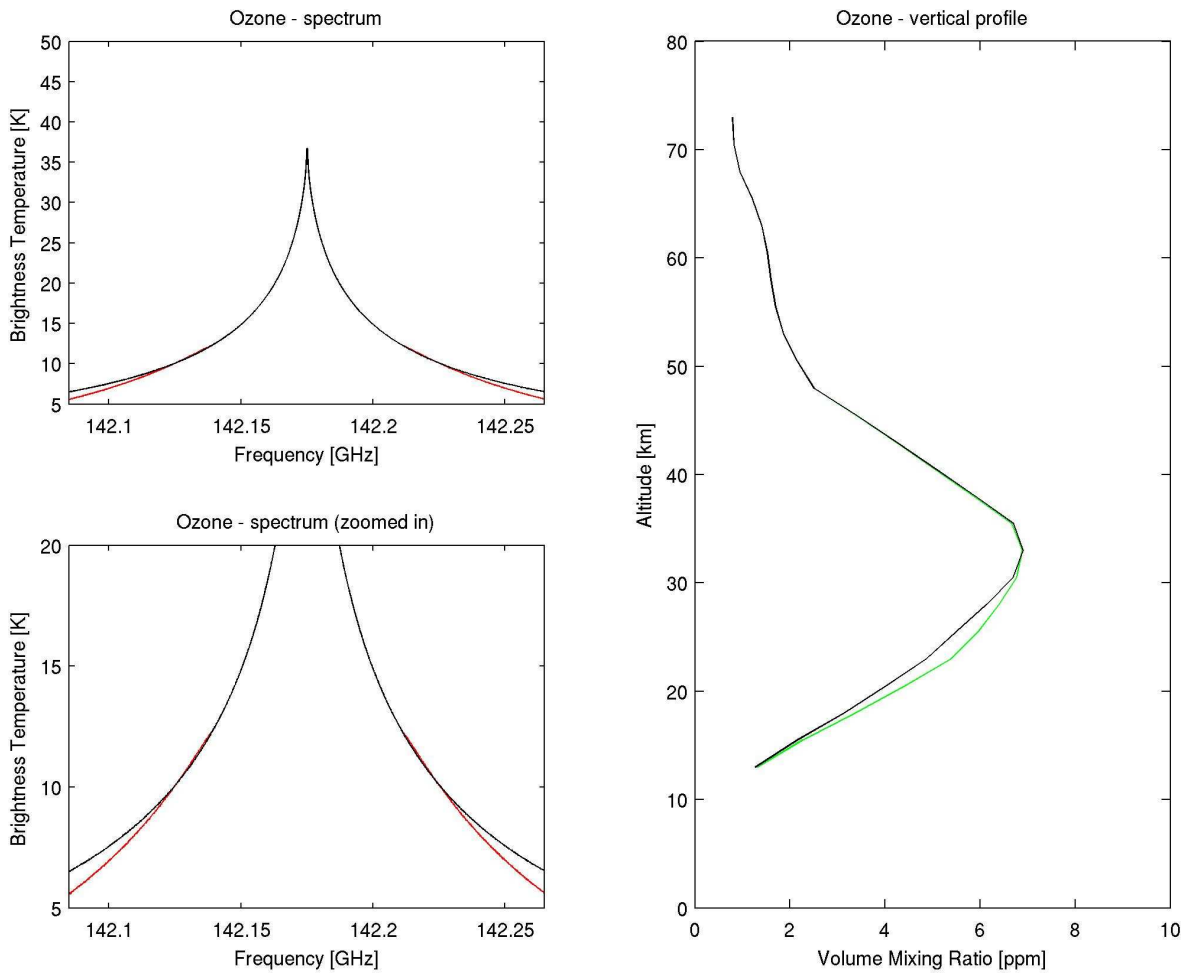


Figure 3.13: Effects of small deviations in the spectral intensity of a synthetic spectrum. Left top panel: synthetic spectrum (black) and subtracting 1.2-K spectral intensity deviation applied in the wings (red). Left bottom panel: zoomed-in plot of the synthetic spectrum (black) and applied deviation of the spectral intensity (red). The right panel shows the retrieved profile obtained from inverting the synthetic original data (black) and the results after adding intensity deviations in the spectrum (green).

## 4 On the high accuracy of measured spectra

The previous chapter demonstrates the importance of how accurately the spectral line is detected. Consequently, it was observed from the numerical analysis that small deviations produced by nonlinearity (e.g., in the microwave devices which compose the heterodyne instrument) could produce erratic values in the observed spectra. Furthermore, simulations demonstrated that such deviations would also lead to incorrect values in the retrieved vertical profile of planetary atmospheres. This chapter focuses on the development of low-uncertainty measurement techniques which facilitate the analysis of linearity along the microwave devices' dynamic range. In Section 4.1, important concepts involving microwave linearity are introduced. In Section 4.2, experimental tests in atmospheric observations show the effects produced by nonlinear behavior in a backend instrument. Section 4.3 describes two novel linearity measurement experiments and their results. Finally, the importance of these experiments for the development of future spectrometers is discussed in Section 4.4.

### 4.1 Linearity

Linearity is the behavior in which the output signal strength varies in direct proportion to the input signal power across a specified operating range of a device. As theoretically expected, a perfect linear device does not introduce any kind of signal distortion, which for practical cases, e.g. due to gain fluctuation, might not always be true.

Some active devices, such as microwave amplifiers, are typically considered to be perfectly linear within well-defined operating ranges. It means that a 1 dB increase in the input results in exactly 1 dB increase in the output power level. As previously stated, this theoretical assumption of linearity is only an approximation in practice, and thus, if such an assumption is overlooked, these devices may be responsible for phenomena which degrade the overall system performance.

On the one hand, nonlinearity in solid-state devices is well known, but on the other hand, little is mentioned about nonlinearity in passive components which are expected to be linear under virtually all conditions. For instance passive components, such as resistors, capacitors and inductors, may evidence nonlinear responses on the extremes of their operating regimes (e.g., as a consequence of high frequencies, voltages, or currents). Even RF connectors create intermodulation distortion at high power or frequency levels, where distortion is caused by the nonlinear resistance of the contacts between dissimilar metals in their construction. Occasionally, nonlinearity may be referred as *quasilinear*-

ity in case these nonlinearities are weak enough to contribute to the deterioration of the system performance. Such concept does not imply that the nonlinearities themselves are negligible, they may produce other kinds of inconveniences (Maas, 2003).

In some devices, nonlinearity is considered to be an adverse effect; however, other components like frequency multipliers exploit the nonlinearities in their circuit's elements. Not surprisingly, in these devices is usually preferred to maximize (in some sense) such effect of nonlinearity, and even to minimize the effects of linearity.

The power-level (or amplitude) nonlinearity should not be confused with the frequency manipulation created in non-linear devices. As an example, the function of an RF mixer (a typical non-linear device) is to translate an input signal with a given frequency into a higher (or lower) frequency. However, if such mixer is said to provide linear operation over a specified operating range, this implies that the output amplitude response will directly follow the input signal strength.

In certain specific applications, it is important how closely the output of a linear device follows the input signal, the so-called direct proportion. This is required by systems which consider linearity as a key function due to high precision while detecting specific signals. In this case, such requirement is demonstrated by mentioning that the received signals are of exceedingly low power, and so the heterodyne systems have to provide both large gains and a highly linear response. Consequently, the measurement of such linearity characteristics requires low uncertainty where the demand of high accuracy usually outreaches those ones on standard measurement applications.

## 4.2 Intercomparisons

In the previous Chapter (see Section 3.3), it was theoretically demonstrated how small deviations on the power density of the spectra (e.g., produced by nonlinearity) may produce significant changes in the retrieved vertical profile of trace gases. However, in practice, small nonlinearities are difficult to evidence on a singular backend instrument during its normal operation (because there is no way to separately determine whether an instrument's response is nonlinear). A way to verify its linear operation could be conducted by comparison with other spectrometers, which may be based on the same or another operation principle.

As mentioned in Chapter 1, the observed atmospheric signal by the heterodyne frontend can be split up and, therefore, analyzed by several spectrometers. For such purpose, intercomparison tests have been performed over the last two years in order to analyze the performance and possible improvement of CTSs. These experiments are implemented on a 142-GHz ozone radiometer with a receiver temperature  $T_R = 500$  K, a 78 K liquid-nitrogen cold load and a hot load at 300 K, i.e.  $T_C = 578$  K and  $T_H = 800$  K respectively. In this case, two CTSs' responses are compared: a 220-MHz bandwidth SOFIA-GREAT CTS and the 400-MHz-bandwidth CTS (Paganini and Hartogh, 2006) by detecting the 142.175-GHz rotational transition of ozone (which is integrated over several days) at MPS (51.39° N, 10.13° E). Therefore, the concept is to observe and compare the operational performance of both spectrometers and evaluate their improvements after different experimentations. Since both spectrometers have the same IF input frequency (i.e., 2.1 GHz), the signal just needs to be split by means of a power splitter in the required frequency

range. In Fig. 4.1, differences can be seen between the two CTS-backend systems on four different dates during November 2006.

On a similar experiment, Müller et al. (2006) reported on the comparison of measurements using Fast Fourier Transform Spectrometers and Acousto-Optical Spectrometers on groundbased observations. Müller et al. (2006) also confirmed discrepancies amongst the spectrometers while detecting the same trace gas in parallel. However, this report has been limited to suggest that such deviations are produced by unwanted frequency components added during the down-conversion mixing process in the frontend.

Summarizing, such differences amongst spectrometers' responses would lead to discrepant results while analyzing the data and, therefore, unlikely physical hypotheses. Generally, these effects are overlooked during observations since the data from only one particular spectrometer are taken into account neglecting the information provided by the others. As stated earlier, such differences are believed to be introduced by nonlinearities in the heterodyne system. Thus, the need to detect, study and eliminate these effects when possible.

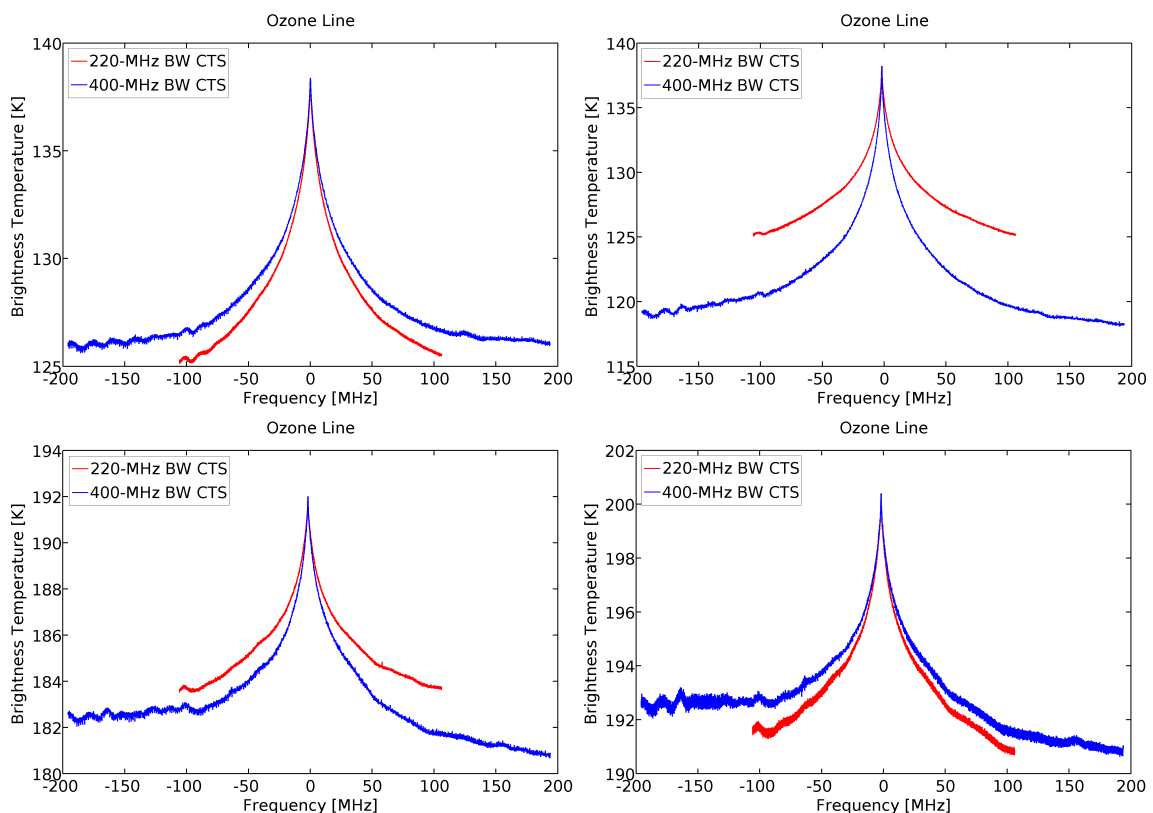


Figure 4.1: Nonlinear behavior observed during intercomparison tests during September–November 2006. Ozone spectra detected by a 220-MHz bandwidth SOFIA-GREAT CTS and a 400-MHz-bandwidth CTS using the 142-GHz ozone radiometer at MPS in Katlenburg-Lindau, Germany.

### 4.3 Linearity measurements

In order to precisely measure the temperature of certain detected signal sources, such as rotational transitions in planetary or cometary atmospheres, a microwave radiometer relies on the power linearity of microwave components which compose the heterodyne system (see Reinhardt et al., 1995, Murk et al., 2005). However, the reliability on these devices could be affected by nonlinear behavior.

The measurement of linearity in devices is performed by observing how linearly the device's output tracks power-level changes in the device's input when producing power-attenuation steps over an injected noise signal. On a typical linear device, the changes in the output should exactly follow the variation in the input signal. This power-level variation is generated by the so-called repeatable step attenuator which produces a range of attenuation steps (Holland and Howes, 2002). As previously discussed in Section 2.4.5, linearity is usually measured in terms of a deviation from an ideal straight line. Wherein the deviation from this straight line is typically obtained by a least-squares fit of the data.

The research on microwave measurements of nonlinearity can be separated at least in two branches: first, the characterization of microwave devices, such as amplifiers and mixers, by means of mathematical models; and second, the measurement instrument itself, i.e., the experimental test setup. In the first case, if the behavior is weakly nonlinear, it is possible to perform nonlinear analysis and modeling of RF devices by power-series or by Volterra-series expansions (for details, see Bedrosian and Rice, 1971, Borremans et al., 2007). The last allows a more detailed and accurate characterization of device characteristics by describing each nonlinearity by a power series representation to reproduce simple components. Moreover, to gain insight into nonlinear behavior, some theoretical techniques involving combined multisines have been applied to locate the main nonlinear components both for weakly and strongly nonlinear behavior (Borremans et al., 2007). Nevertheless, measurements of each relevant parameter (i.e., the kernels of the Volterra-series) can be time consuming and thus exceeding measurement capabilities. Some other approaches involving other kind of mathematical models are used to describe amplitude and phase nonlinearities. Based on these, comparison with experimental results by different methods such as single-tone, two-tone, three-tone and noise loading tests have been performed by Heiter (1973), Reinhardt et al. (1995), Berceci and Marozsák (2006). In related fields, other measurements which address the importance of accuracy in microwave systems, such as attenuation standards (see Widarta et al., 2003, Iida et al., 2006) or microwave devices (see Holland and Howes, 2002), have also been developed. This study focuses mainly in the second field, i.e. the experimental test setup to detect nonlinear behavior.

Traditional methods for linearity measurements, in similar applications, are known to hardly achieve accuracy better than 1 to 2% due to uncertainties introduced in the test setup. Based on these, similar techniques were applied in order to measure regions where the instrument behaved linearly (see Section 2.4.5). In the CTS, such ranges were attained by injecting a noise source at the input and, by producing variable 1-dB step attenuation in a 60-dB dynamic range, procure deviations of  $\pm 0.1$  and  $\pm 1$  dB after performing a linear fit of the spectrometer's response (Paganini and Hartogh, 2006, Villanueva et al., 2006a). Nevertheless, the 1 to 2% uncertainties forbid to determine whether these differences in the power spectral density are a consequence of nonlinearity.

As a rule of thumb, while studying nonlinearities, the experiment setup should mimic the real operational conditions over which the device under test (DUT) is usually endeavored; for instance, while selecting a type of excitation signal.

Previously in Chapter 3, a numerical method demonstrated the significance of possible small nonlinearities affecting heterodyne systems and, thereafter, probable divergences from the proper values were quantized. Upon these and the sum that deviations on the measured power spectral density exist (see Section 4.2), there arises the question on how accurately a linearity estimation method could be implemented. Here is the breakpoint where, like as also mentioned in the previous chapter, an uncertainty below 0.1% in the measurement setup is mostly required. In order to do that, there exist three important constraints: the experimental setup should measure a) over the whole frequency range in which the device is intended to operate; b) with low uncertainty (preferably, less than 0.1%); and c) by feeding a noise-like input over a wide dynamic range (at least, more than 40 dB).

### 4.3.1 A 3-dimensional analysis method

As stated earlier, a traditional method to calculate linearity of a certain device under test (e.g. amplifiers or mixers) was conducted by using a noise source and step attenuator (Section 2.4.5). Motivated by the discussion above, in this section a novel 3D analysis is presented in order to identify nonlinearities in microwave devices (see Paganini et al., 2007).

The measurement test setup, defined in the following description, is composed by a 3.5-GHz bandwidth noise source (+5 dBm power level output) as stimulus signal; three programmable high-repeatability step attenuators (SAtt), two RSP Rhode & Schwarz (SAtt 1 and 3, see Table 4.1) plus one Agilent 11713A (SAtt 2, see Table 4.2); and a Rhode & Schwarz (hereafter R&S) FSP30 spectrum analyzer (Table 4.3) which can measure the absolute power density at an adjustable center frequency and bandwidth (Bertocco and Sona, 2004). These devices were commanded via GPIB interfaces in order to achieve fast, accurate and automatic measurements (Fig. 4.2).

Following on, a 3-dimensional plot can be obtained thanks to the possibility to change central frequencies and bandwidths in the spectrum analyzer. This plot is composed by three variables: a) input power level, b) output power level, and c) frequency domain in the frequency domain. The idea is to measure the power density at subsequent, small frequency intervals (e.g. a 200-MHz frequency interval in a total of 3.5 GHz). Its advantage relies on the fact that spurious/non-linear regions can be separately determined. Usually, a power meter measures power levels on the complete frequency range, i.e. without discriminating frequency regions. Hence, this method offers the chance to extend and complement the identification of nonlinearities not possibly observed in simple 2D plots.

In principle, this method involves a differential approach to improve the accuracy of the linearity measurement. Two step attenuators are used in order to determine the linear dynamic range of the DUT. This method steps the first step attenuator (SAtt 1) in a 60-dB range from 0 to 60 in 1-dB steps, during each of these single steps a second step attenuator (SAtt 2) steps from 0 to 1 dB; i.e., twice the data for each step coming from SAtt 1. Behind the DUT, a third step attenuator (SAtt 3) produces 1-dB step changes from 60 to 0 dB. The last ensures that the spectrum analyzer operates over almost the same measuring range in

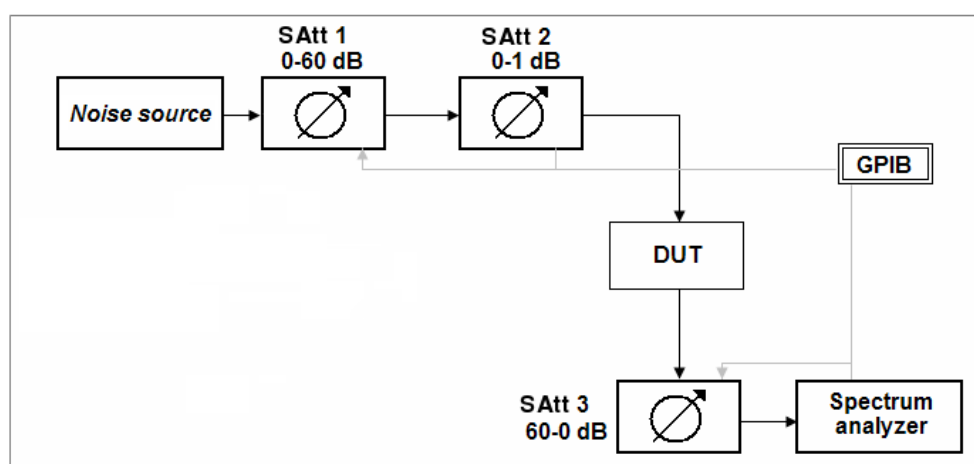


Figure 4.2: 3-dimensional measurement test setup. This method steps the first step attenuator (SAtt 1) in a 60-dB range from 0 to 60 in 1dB-steps, during each of this single steps a second step attenuator (SAtt 2) steps from 0 to 1 dB, and thus obtaining twice the data for each step coming from SAtt 1. Behind the DUT, a third step attenuator (SAtt 3) produces 1dB-step changes from 60 to 0 dB.

Table 4.1: Specifications for the R&S RSP step attenuators

Frequency range	0 to 2.7 GHz
Attenuation range	0 to 139.9 dB
Smallest step (from 1 dB)	0.1 dB
Characteristic impedance	50 $\Omega$
Attenuation error $f \leq 2$ GHz	$\leq \pm (0.15 \text{ dB} + 1\% \text{ of setting})$
Power-handling capacity	1 W
Lifetime	$10^7$ switching operations

order to minimize its uncertainties. While the step size of even the best step attenuators scatters from step to step over their dynamic range, which indicates the main reason of the 1-2% uncertainty and so applies to SAtt 1 and 3, the step size of SAtt 2 is assumed to stay constant over at least several thousand steps. Therefore, this clearly indicates that changes in the measured level ratio must be caused by nonlinearities of the DUT.

Table 4.2: Specifications for the Agilent 11713A (+84904K)

Frequency range	0 to 26.5 GHz
Attenuation range	0 to 11 dB
Smallest step	1 dB
Insertion loss at 0 dB	0.8 dB + 0.04 dB/GHz
Characteristic impedance	50 $\Omega$
Attenuation error $f \leq 2$ GHz	$\leq \pm 0.16$ dB
Repeatability life	0.03 dB
Power-handling capacity	1 W
Lifetime	$5 \times 10^6$ switching operations

Table 4.3: Specifications for the R&amp;S FSP30 spectrum analyzer

Frequency range	9 kHz (20 Hz) to 30 GHz
RF Performance	1-dB-compression point 0 dBm
Measurement uncertainty	0.5 dB total level uncertainty up to 3.6 GHz < 0.2 dB linearity error down to -70 dB
Measurement speed	2.5 ms sweep time in frequency domain 1 $\mu$ s sweep time in time domain up to 70 remote measurements/s via GPIB
Input impedance	50 $\Omega$

Table 4.4: Methods comparison: measurement-uncertainty calculation

Power range	-60 to -50 dBm	-50 to -10 dBm	-10 to 0 dBm
3D differential method	1.5%	0.3%	1%
Traditional method	9%	2.2%	3%

In order to compare the performance of these methods, Fig. 4.3 depicts the total standard uncertainty (type A) according to ISO standards (see Bich et al., 2006, Glesser, 1998) over the whole dynamic range of the test setups. In this example, two cases are compared: a) the traditional method and b) the novel 3D analysis. As a result, an improvement in accuracy can be observed by comparing both uncertainty values (from the traditional method and the new approach). Moreover, table 4.4 indicates an accuracy of better than 1%, for the 3D method, in a 40 dB range.

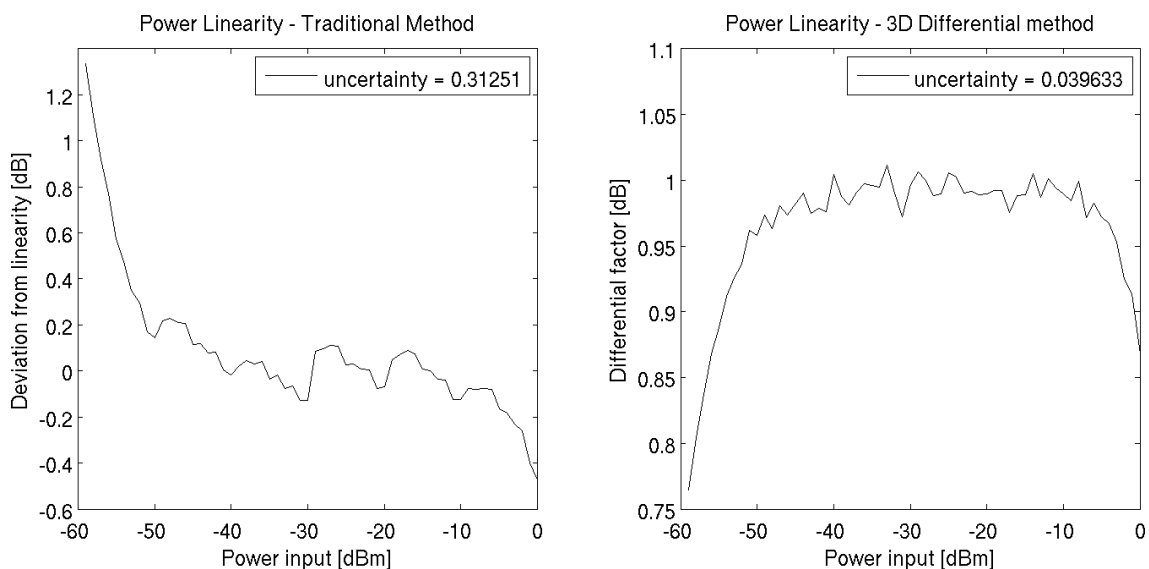


Figure 4.3: Methods comparison by calculating the standard uncertainty over the whole dynamic range of the test setups. *Left*: Traditional method. *Right*: 3D differential method.

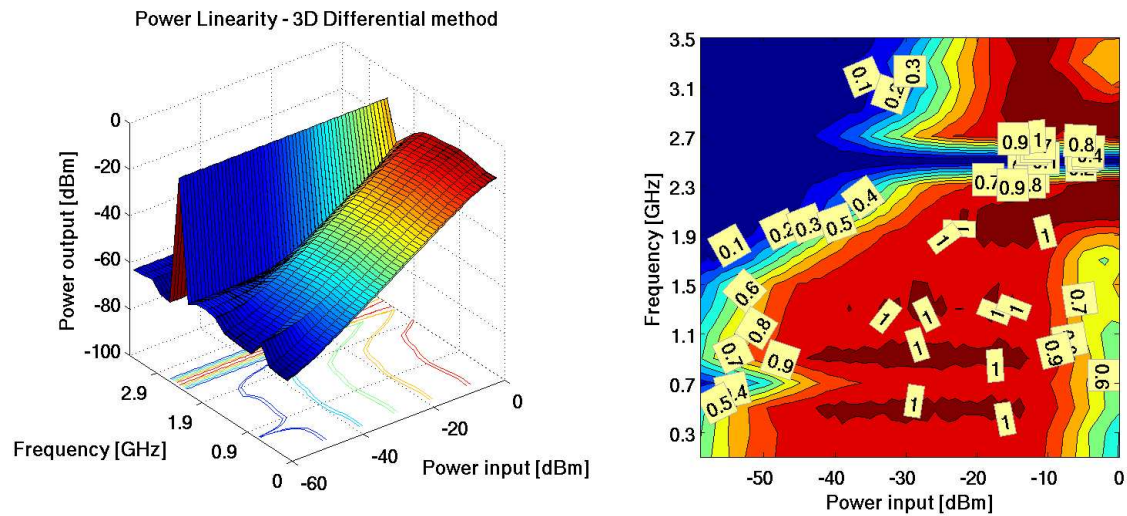


Figure 4.4: The 3D analysis was applied to an RF ZFM-4212 mixer where an external 2.5-GHz LO signal was injected. *Left*: the answer given by the IF port of the mixer. *Right*: the applied differential method can be seen as a contour plot where values close to '1' indicate linear behavior.

#### 4.3.1.1 Examples

Different microwave devices were tested using the 3D analysis method. For instance, Fig. 4.4 shows an RF ZFM-4212 mixer in which an external 2.5-GHz (+7 dBm) LO signal was injected. The answer given by the IF port of the mixer can be observed on the left plot. On the other hand, the applied differential method is plotted as a contour plot on the right side where values close to '1' indicate linear behavior. Following, the examination shows further examples of RF mixers (see Figs. 4.4-4.6) and RF amplifiers (in Figs. 4.7-4.8). For further details about the DUT's characteristics, the reader is referred to Appendix D.

#### 4.3.1.2 Improvements provided by this method

This method facilitates the analysis of the linearity response on microwave devices, such as complete RF stages in the CTS. For instance, Fig. 4.9 shows the 3D analysis before the down-conversion mixing stage where the atmospheric signal is mixed with the chirp signal. Thereafter, if nonlinearity has been identified over specific frequency regions, the idea is to study possible mechanisms to minimize the non-required behavior.

Usually, a typical mixer's response implies two nonlinear regions. In fact, these regions can be observed in the left plot of Fig. 4.4. Firstly, at low power input levels where the nonlinearity is produced by the inherent noise of the device; and secondly, at higher levels as a result of the 1-dB compression point. At 2.5 GHz, the feed-through in the IF port entails another source of nonlinearity (the feed through is specifically the forward signal leakage to the IF port, in this case, as a consequence of a low LO-IF isolation characteristic); however, the IF port is not intended to operate in this range (normally, the IF-port response is below this frequency). Surprisingly, a kind of intermodulation product, observed in lower frequencies ( $\sim 0.7$  GHz), suggests nonlinear responses for small power input levels at the RF port (up to -40 dBm). It should be stressed that such anomaly (not

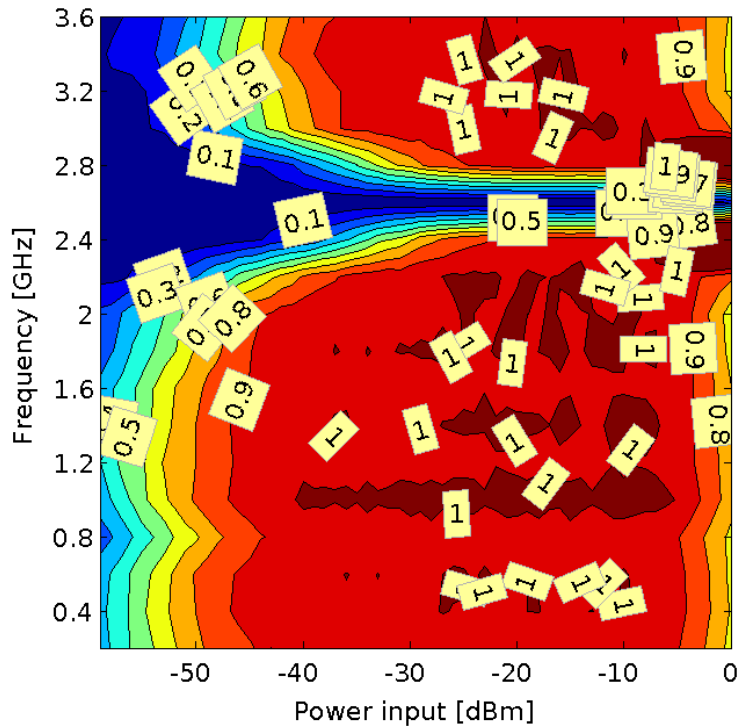


Figure 4.5: 3D analysis method applied to an RF ZFM-15 mixer. The differential method is displayed a contour plot (values close to '1' indicate linear behavior).

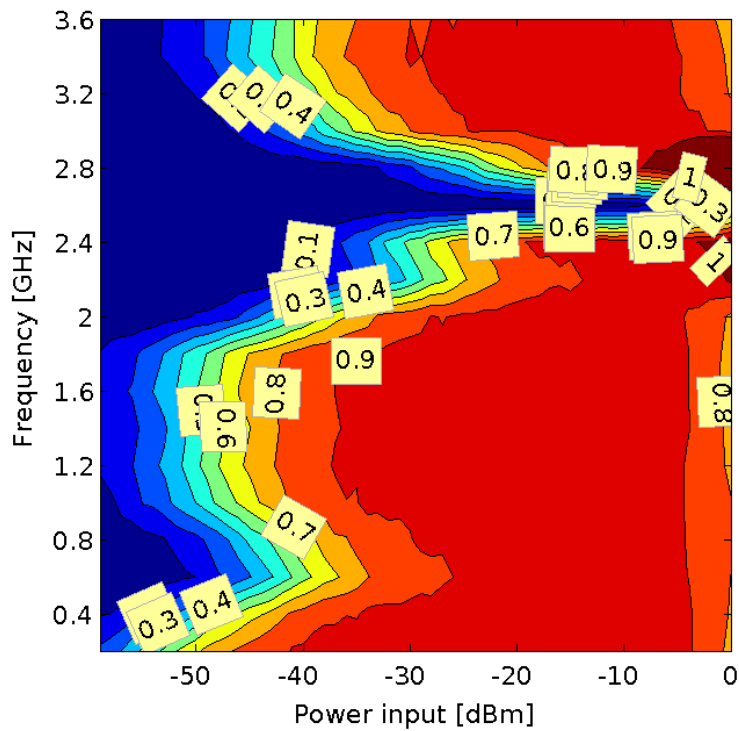


Figure 4.6: 3D analysis method applied to an RF MCA-35LH mixer. The differential method is displayed a contour plot (values close to '1' indicate linear behavior).

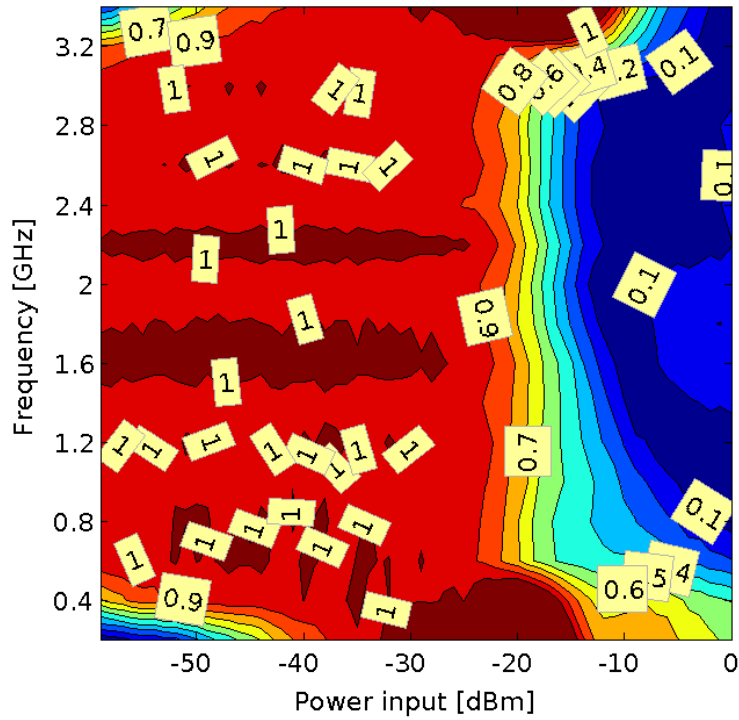


Figure 4.7: 3D analysis method applied to an RF ABA-53563 amplifier. The differential method is displayed a contour plot (values close to '1' indicate linear behavior).

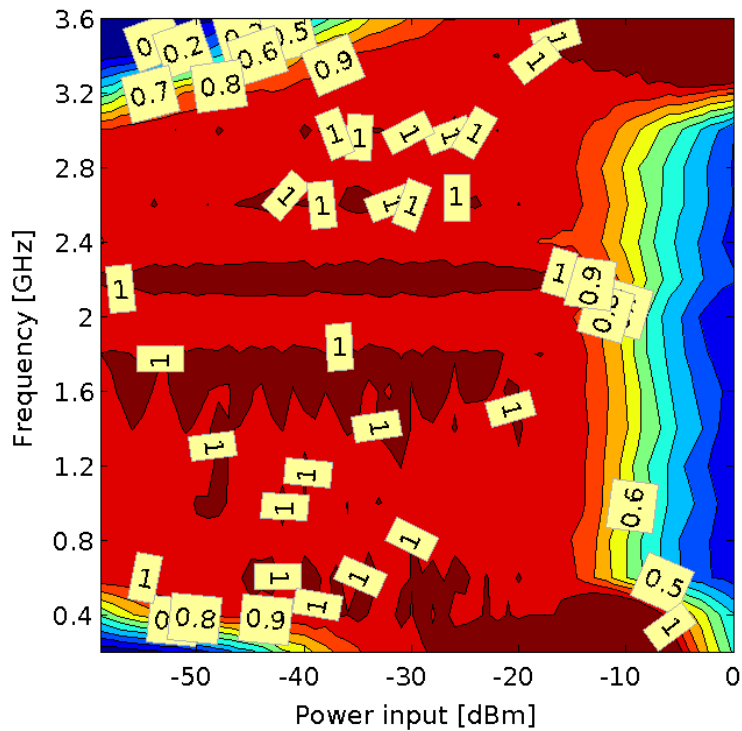


Figure 4.8: 3D analysis method applied to an RF MGA-82563 amplifier. The differential method is displayed a contour plot (values close to '1' indicate linear behavior).

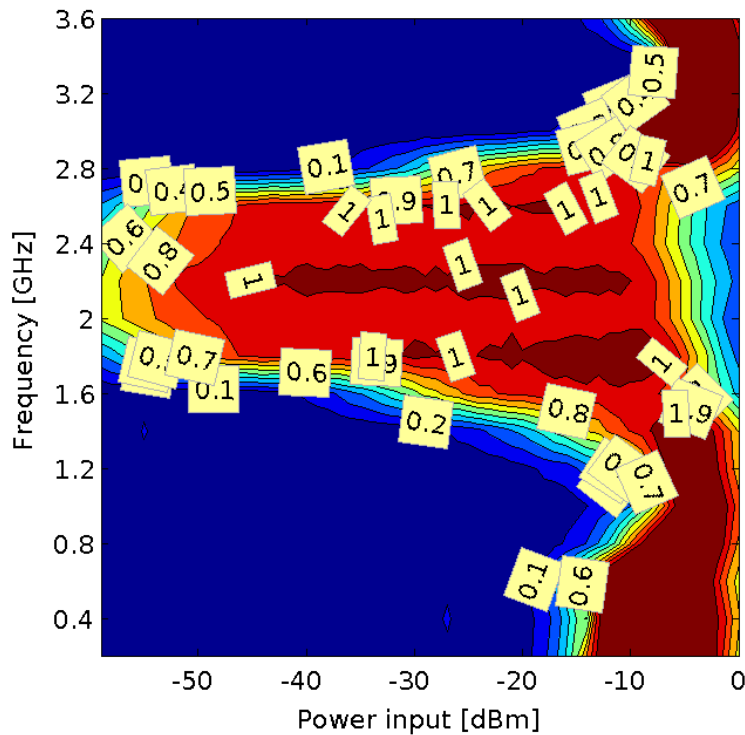


Figure 4.9: 3D analysis method applied to the spectrometer's input stage (input frequency range: 1.9-2.3 GHz) before the down-conversion stage. The differential method is displayed a contour plot (values close to '1' indicate linear behavior).

identified before) may lower the spectrometer's performance since the measured weak atmospheric signals usually lie within this region.

The further investigation aimed to determine whether this behavior on the mixer's response was also affecting the measured signal in the spectrometer system. In order to answer the previously stated, the 3-dimensional analysis was applied in the main mixing stage of the 400-MHz-bandwidth CTS, i.e., where a ZFM-4212 mixer was installed (Fig. 4.10). As mentioned before, the task of this stage is to down-convert the input signal (1.9-2.3 GHz) by modulating it with a chirp signal of 0.8 GHz bandwidth into the 0.6-1.4 GHz frequency range (Paganini and Hartogh, 2006). As a result, unexpected nonlinearity was detected affecting the 0.8-1.2 GHz range. The detection of this problem, not distinguishable before with traditional techniques, allowed its minimization by both reducing the power level of the chirp signal acting as LO and slightly increasing the amplification gain of the atmospheric input signal (see Paganini et al., 2007). Next, Fig. 4.11 shows the achieved improvements in the  $O_3$  spectra detected in the ozone radiometer. To summarize, the differences among the two spectrometers have been minimized on the lower left wing, however, some discrepancies are still observed on the right side.

### 4.3.2 A novel high-accuracy method

In the last section, a first approach was described using a 3D analysis method. Even though the 3D analysis is a potential tool providing frequency-selective measurements to

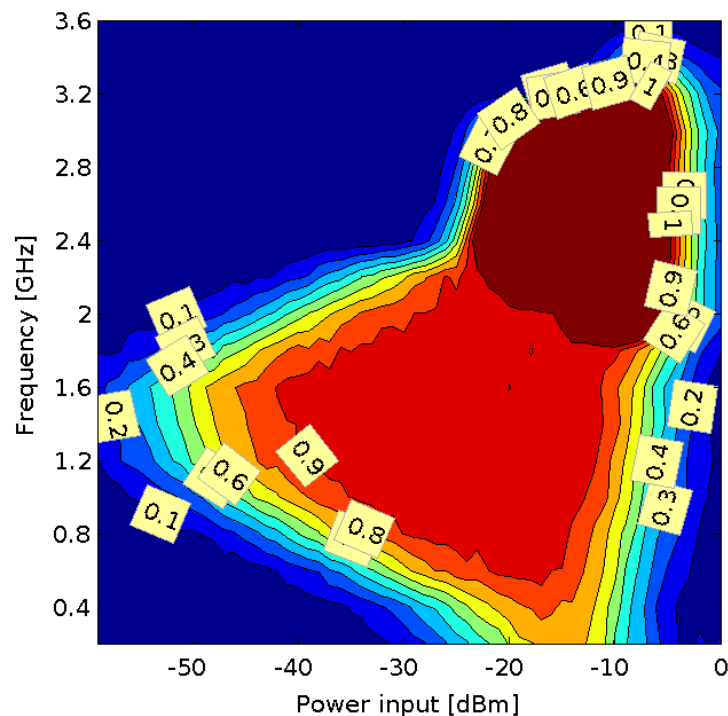


Figure 4.10: 3D analysis over a mixing stage in the 400-MHz bandwidth CTS using the ZFM-4212 mixer. The differential method is displayed a contour plot (values close to '1' indicate linear behavior).

search particularly abnormal behaviors in microwave devices, its stability is still not good enough to detect nonlinearities below the 0.1% limit in a 60 dB range. In the following, an improved experiment, based also on a differential approach, is developed under such constraint.

According to Fig. 4.12, the measurement of linear response in the DUT is implemented by a noise source (with +5 dBm power-level output and a maximum operating frequency of 3.5 GHz), which provides the excitation noise signal, and three programmable high-repeatability step attenuators, namely, two Agilent 11713A (SAtt 1 and 2) plus one RSP R&S (SAtt 3). Additionally, a R&S NRP power meter with NRP-Z21 sensors is used as detector to measure the power output. The advantages of such detector are translated into high speed, low measurement uncertainty and high-precision measurements (see Table 4.5). The detector's integration time is 300 ms for each step, whereby the gain of the complete setup needs to be stable over this timescale, and the whole measurement run takes 10 minutes to be completed.

In this test setup, SAtt 1 is generating 1-dB steps in a total range from 0 to 60 dB, meanwhile on each single step from SAtt1, SAtt 2 produce a nominal attenuation step from 0 to 1 dB which signifies the base for the differential approach. Even though the power meter has a 60-dB dynamic range (according to its specifications), it was found that its lowest uncertainty was obtained for measured values exceeding -30 dBm. Consequently, SAtt 3 ensures that the detector measures over such power range.

The overall test-setup accuracy was noticed to be affected by instabilities of the second

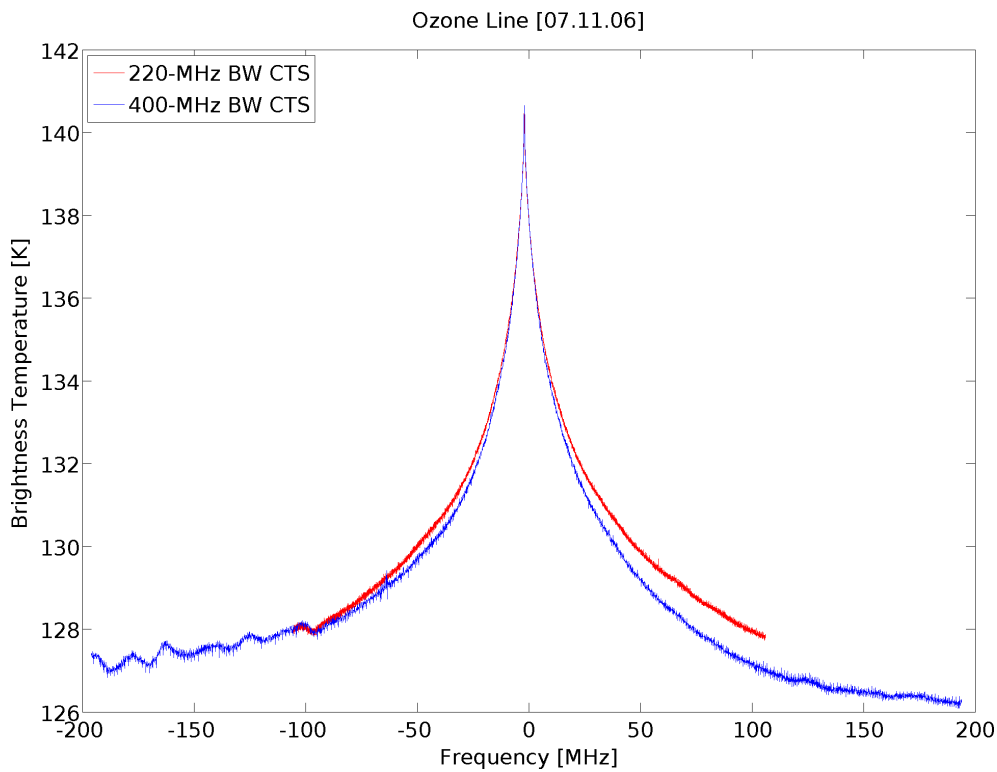


Figure 4.11: Achieved improvements in the O<sub>3</sub> spectra, detected in the ozone radiometer, after using the 3D analysis method. The differences among the two spectrometers have been minimized on the lower left wing; however, some discrepancies are still observed on the right side.

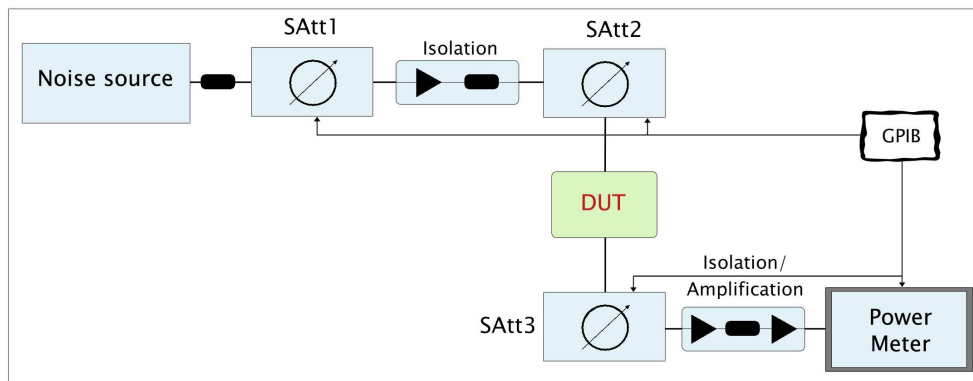


Figure 4.12: High-accuracy method using the differential approach: a) Noise source (+5 dBm power-level output, in a frequency up to 3.5 GHz). b) Three programmable high-repeatability step attenuators (SAtt), two Agilent 11713A (SAtt 1 and 2) plus one RSP R&S (SAtt 3), provide the attenuation steps. c) A R&S NRP power meter with NRP-Z21 sensors are used as detector. GPIB interfaces are used to command these devices.

step attenuator, i.e., the one in charge of performing the differential step of 1 dB. For this experiment, the Agilent 11713A showed a better stability compared with the RSP R&S step attenuator.

Table 4.5: Specifications for the R&amp;S NRP-Z21 power meter (20 °C to 25 °C)

Frequency range	10 MHz to 18 GHz
Level range	-67 dBm to +23 dBm
Measurement uncertainty	1.5% (0.58 dB absolute, 0.022 dB relative)
Measurement speed	1500 measurements/s (buffered mode)
Input impedance	50 $\Omega$

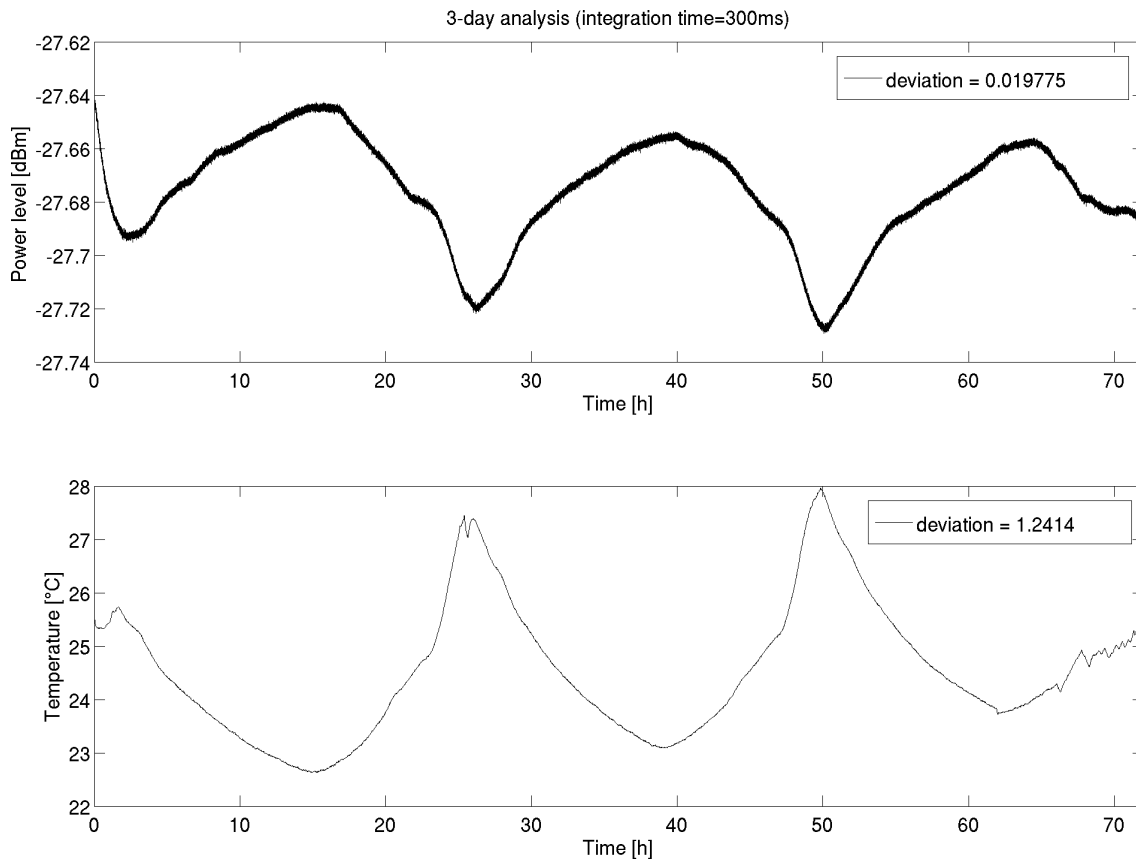


Figure 4.13: Temperature variations on a 3-day-long analysis under laboratory conditions at MPS.

#### 4.3.2.1 Gain fluctuations

Possible gain fluctuation produced by temperature variations are of especial importance. They were studied on a 3-day-long analysis test under laboratory conditions at MPS (Fig. 4.13). As a result, it was observed a gain-fluctuation dependence with temperature, however, the divergence over the 10-minute measurement were kept to an acceptable minimum. Despite of this, because of the high sensibility of this test setup, the temperature variations are monitored and evaluated on every measurement (using a PT100 sensor).

For uncertainty reduction and better performance, a zeroing of the power meter is performed at the start of each measurement. In order to do that, the complete test setup is programmed in a high impedance state; i.e., the step attenuators are set with a high resistive value in order to avoid the influence of the noise source. Apart from keeping the thermal balance, this has the advantage that the noise superimposed on the test signal can

be detected on zeroing and, thus, does not impair the measurement results.

Special care has to be taken that the measurements are not affected by secondary effects produced in the test-setup chain, such as reflections or saturation levels in the amplification stages. This is done by both keeping connections as short as possible and strategically adding high isolation on critical locations which also ensures that the effects of mismatch, produced by differences in the match while switching the step attenuators, are minimized. Microwave-leakage effects on the chain are also avoided by using coaxial, semi-rigid cables (Sucoflex technology) qualified for high precision systems up to 18 GHz frequency, routine inspection and cleaning, and by keeping cable lengths as short as possible.

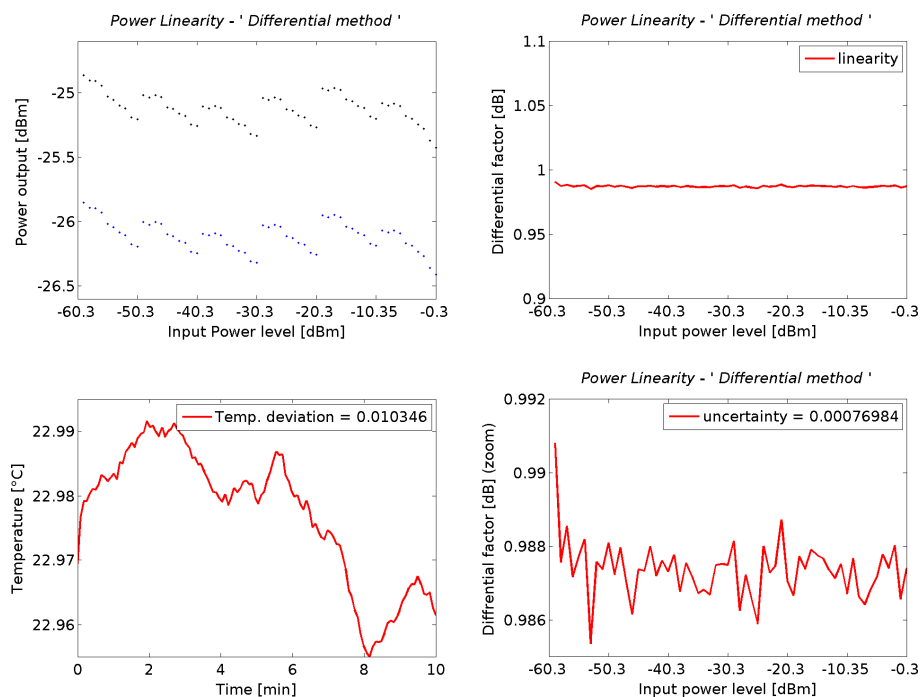


Figure 4.14: The test setup achieves a total level testing range from  $-60.3$  dBm to  $-0.3$  dBm, i.e. a 60-dB dynamic range applied to the DUT, and an optimal standard uncertainty equal to  $0.00077$  dB (0.02%). *Upper left:* power-level output vs. power-level input of the DUT (black and blue plots represent the differential 1-dB step). *Bottom left:* sensed temperature. *Upper and down right (zoomed):* calculated differential factor.

The test setup provides a total input-power level range from  $-60.3$  dBm to  $-0.3$  dBm, i.e. a 60-dB dynamic range applied to the DUT, with an optimal standard uncertainty equal to  $0.00077$  dB (0.02%) as displayed in Fig. 4.14. Therefore, the objective behind this method is to compare the response provided by a DUT (such as an active device) and observe deviations from the 'ideal' linear behavior provided by the test setup. In other words, since it is clear that this test setup has a high linearity over the 60-dB dynamic range, deviations from such ideal linearity are assumed to be produced by the DUT.

#### 4.3.2.2 Measurement results

Several microwave devices were tested using this method in order to check and study possible nonlinear behavior not detected before by traditional procedures. Responses provided by four different broadband RF amplifiers are observed in Figs. 4.15-4.18, meanwhile the answers given by three typically used RF mixers are in Figs. 4.19-4.21.

Each figure is subdivided in four plots: in the upper left is the power-level output vs. power-level input of the DUT (the black and blue plots represent the differential 1-dB step); on the right, upper and lower (zoomed), it can be seen the calculated differential factor; and on the lower left is the sensed temperature during the 10-min measurement duration. Two colored lines are shown on the right side plots, the red line (tagged 'linearity') indicates the 'ideal' linearity (with 0.02% uncertainty) given by the test setup as that calculated in Fig. 4.14; on the other hand, the blue line (tagged 'DUT') represents the differential factor calculated from the DUT's response. Accordingly, it is possible to determine how nonlinear the DUT's response is by comparing both lines (red and blue lines), and thus, derive conclusions on its linear behavior and overall efficiency.

While observing these figures, it can be established that the amount of tested microwave devices achieving a high-linear response is limited. For instance, the ABA-54564 and ABA-53564 broadband amplifiers show a good response on the middle power-level input ranges, in opposite to low and high power regions. Furthermore, some strange behaviors are noticed in Fig. 4.15 and Fig. 4.18. On the first one, an ABA-51564 broadband amplifier, it is observed a kind of dip at -20.3 dBm; whereas on the other one, the MSA-0735 amplifier's linear response never equals that of the 'ideal' linearity level. Although interesting, it is beyond the scope of this work to study the physical reasons behind these phenomena (a theoretical study of nonlinear behavior in microwave devices can be found in Maas, 2003). Following, the answers provided by mixers are relatively linear evidencing small oscillation over the ideal response.

Hence, through this method, it is possible to identify and distinguish regions where a highly linear amplitude response is expected on microwave devices or even detect defective devices indicated by atypical responses.

#### 4.3.2.3 Methodology applied to CTSs

Linearity of better than 0.1% can be singularly achieved by some microwave devices in very well-defined power regions. Consequently, the concept behind this method is to, after each device was singularly revised, apply this high-accuracy tool to active and passive devices (such as mixers), or RF stages comprising the CTS and confirm whether the linearity requirement is accomplished. Therefore, singular components are especially selected from several devices of the same type, provided that the best linear response is attained for their required functional purpose. If properly chosen, a complete arrangement conformed by several microwave devices might also attain such linearity requirement thanks to this method. In case of jittering (e.g. in mixers), the components are selected such that the overall response keeps as linear as possible within the high-accuracy requirement.

As previously mentioned, the CTS is composed by an analog part (see Section 2.3) containing several microwave devices, yet some crucial regions are of especial importance. In here, it is generally desired that such regions provide an amplitude response as

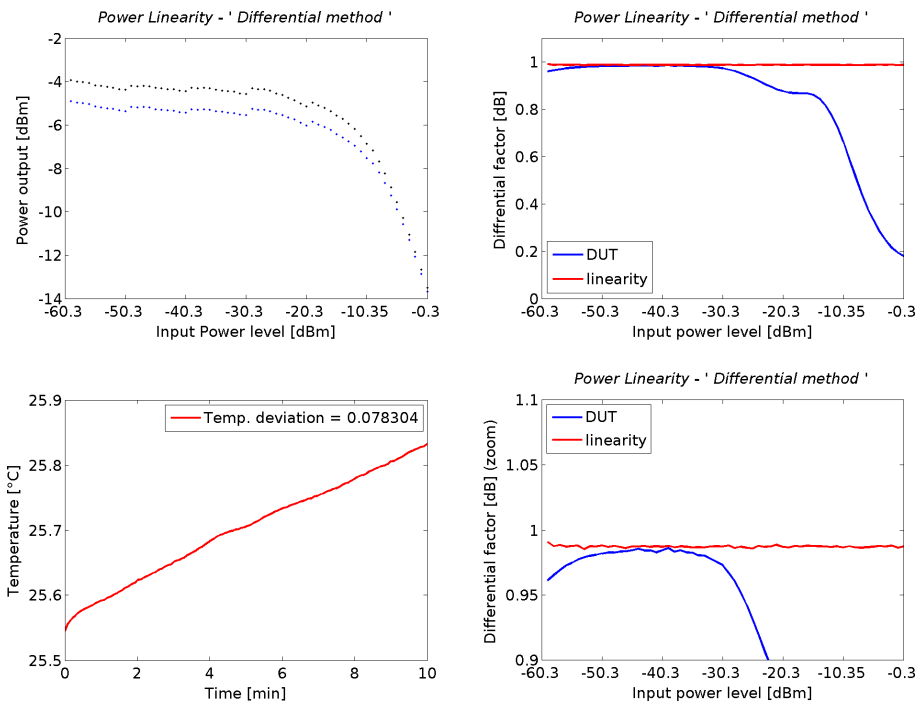


Figure 4.15: High-accuracy method applied to an RF ABA-51563 amplifier. *Upper left:* power-level output vs. power-level input of the DUT (black and blue plots represent the differential 1-dB step). *Bottom left:* sensed temperature. *Upper and down right (zoomed):* calculated differential factor.

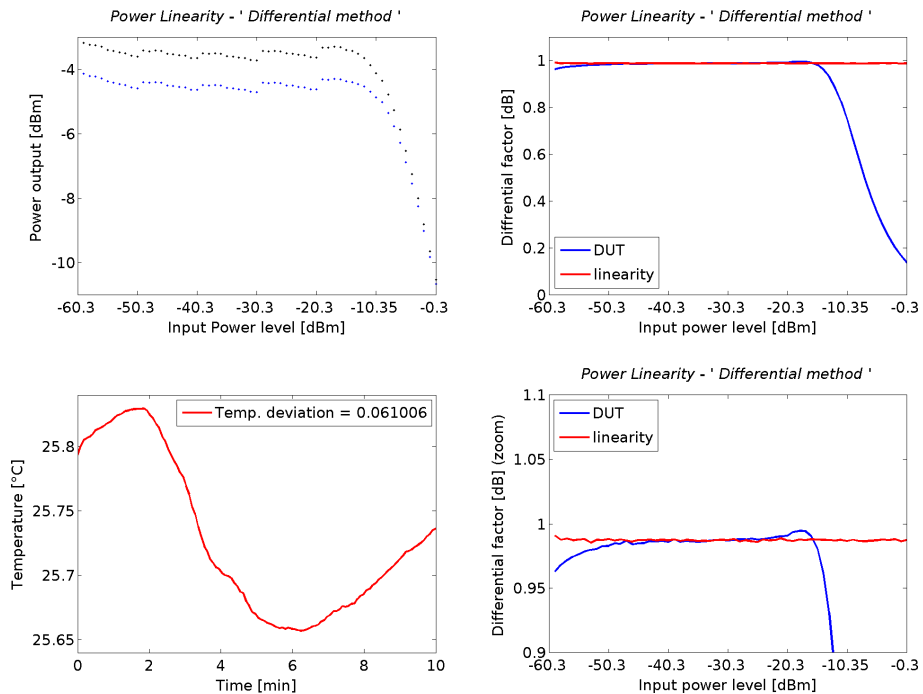


Figure 4.16: High-accuracy method applied to an RF ABA-53563 amplifier. *Upper left:* power-level output vs. power-level input of the DUT (black and blue plots represent the differential 1-dB step). *Bottom left:* sensed temperature. *Upper and down right (zoomed):* calculated differential factor.

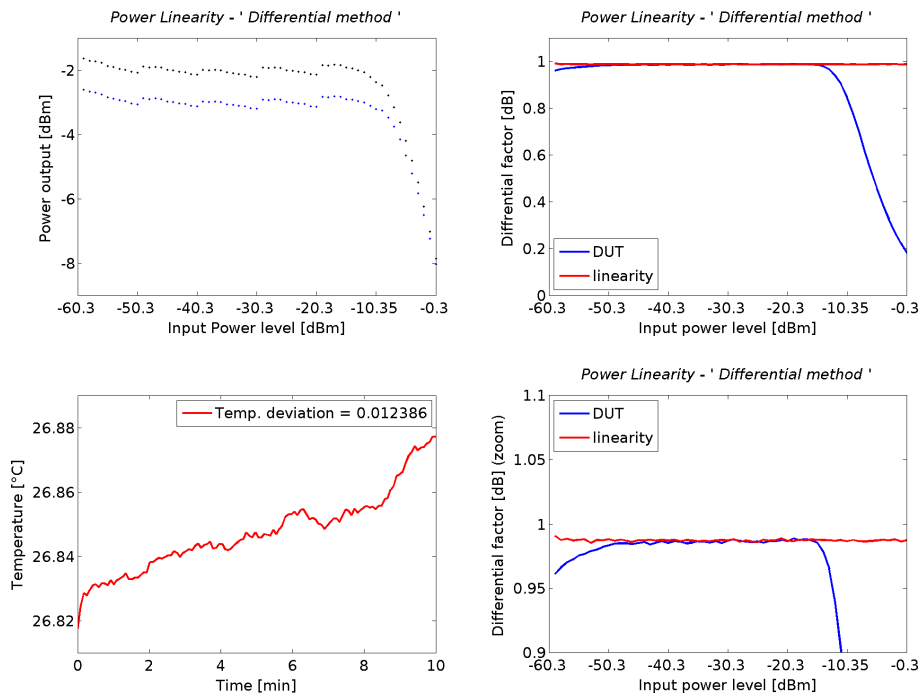


Figure 4.17: High-accuracy method applied to an RF ABA-54563 amplifier. *Upper left:* power-level output vs. power-level input of the DUT (black and blue plots represent the differential 1-dB step). *Bottom left:* sensed temperature. *Upper and down right (zoomed):* calculated differential factor.

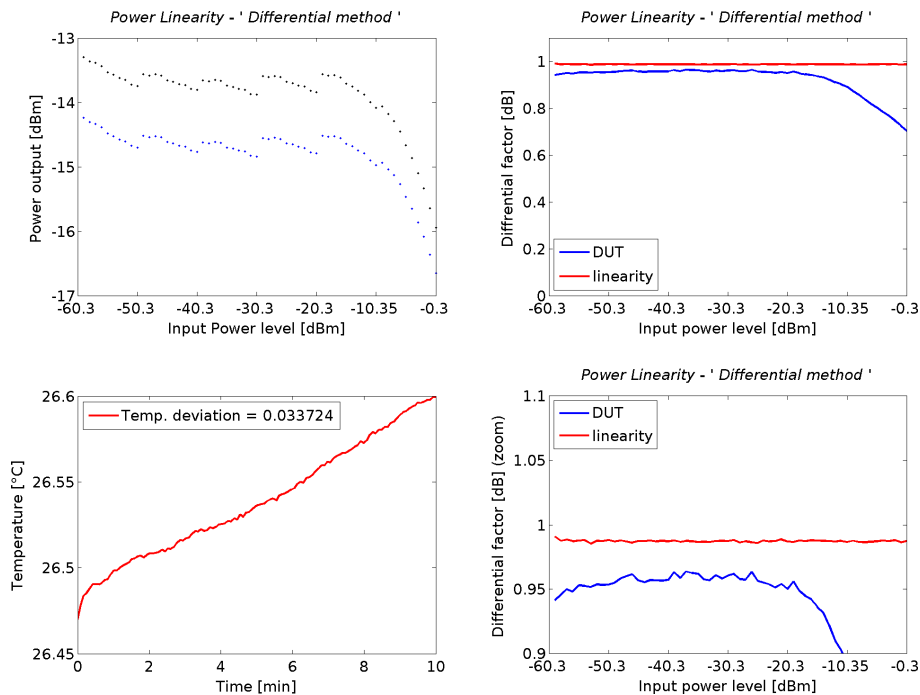


Figure 4.18: High-accuracy method applied to an RF MSA-0735 amplifier. *Upper left:* power-level output vs. power-level input of the DUT (black and blue plots represent the differential 1-dB step). *Bottom left:* sensed temperature. *Upper and down right (zoomed):* calculated differential factor.

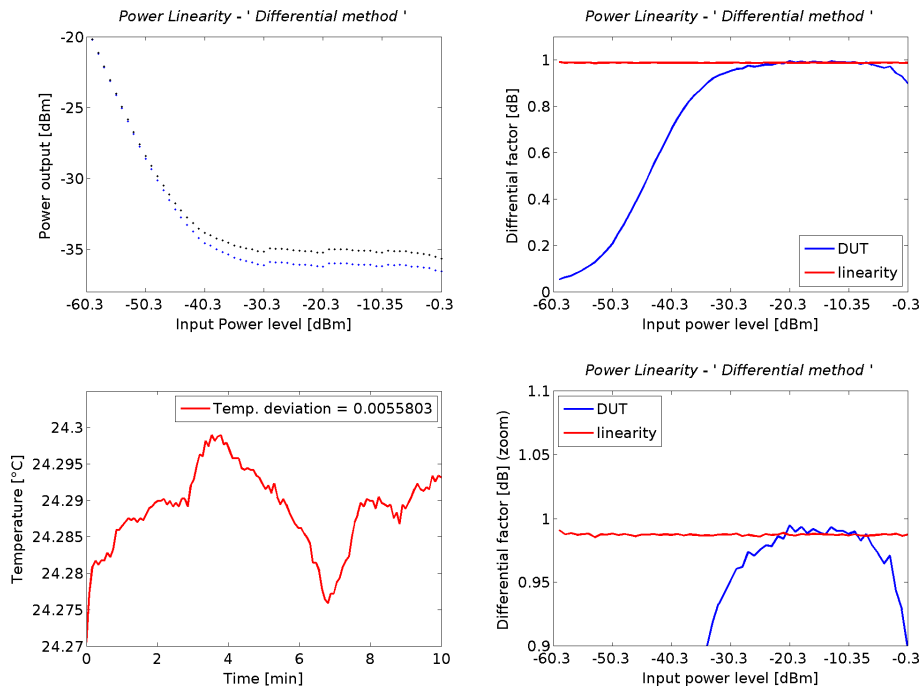


Figure 4.19: High-accuracy method applied to an RF MCA-35LH mixer. *Upper left:* power-level output vs. power-level input of the DUT (black and blue plots represent the differential 1-dB step). *Bottom left:* sensed temperature. *Upper and down right (zoomed):* calculated differential factor.

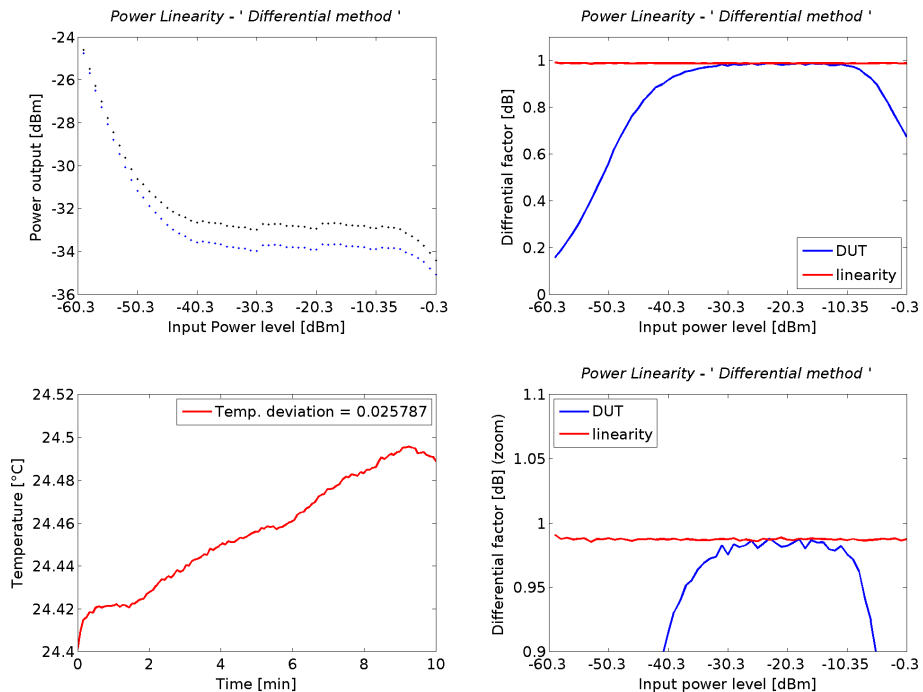


Figure 4.20: High-accuracy method applied to an RF ZFM-4212 mixer. *Upper left:* power-level output vs. power-level input of the DUT (black and blue plots represent the differential 1-dB step). *Bottom left:* sensed temperature. *Upper and down right (zoomed):* calculated differential factor.

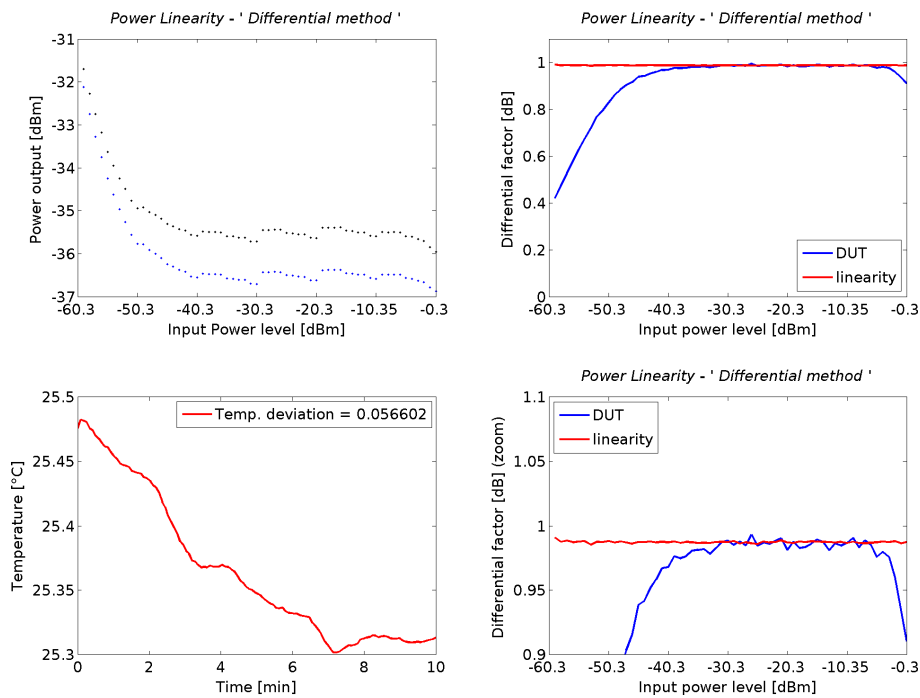


Figure 4.21: High-accuracy method applied to an RF ZFM-15 mixer. *Upper left*: power-level output vs. power-level input of the DUT (black and blue plots represent the differential 1-dB step). *Bottom left*: sensed temperature. *Upper and down right (zoomed)*: calculated differential factor.

linear as possible, in particular the ones after the mixing process where the incoming atmospheric signal is down-converted by mixing it with the chirp signal. These regions are highlighted in Fig. 4.22 and are named as 'zones'. As a result, different zones were tested as a means to find out whether the linearity of singular components was preserved in case that other devices are placed together while assembling RF stages in the CTS (Figs. 4.23 and 4.24). Additionally, these figures suggest that a proper linearity is achieved for an input power level equal to -30 dBm.

This methodology is, therefore, a crucial issue when designing spectrometers with the purpose of finding the best arrangement (for instance, using a component in a certain examined stage which behaves more linearly than others). However, the more assembled components, the more complicated this task becomes. This suggests that the joint complexity turns to be larger; e.g., because of different power level ranges, compression and saturation points, and noise-floor limits constrained by the components' requirements. In spite of that, this may lead to a compromise situation in which the associated linearity is kept as close as possible to an optimal value demarked by the 'ideal' linearity (the red line).

#### 4.3.2.4 Improvements

The low uncertainty of this method provides a unique opportunity to carefully select components which efficiently attain the expected responses focusing mainly in the linearity issue. Thanks to its high accuracy, certain peculiarities were noticed in some broadband

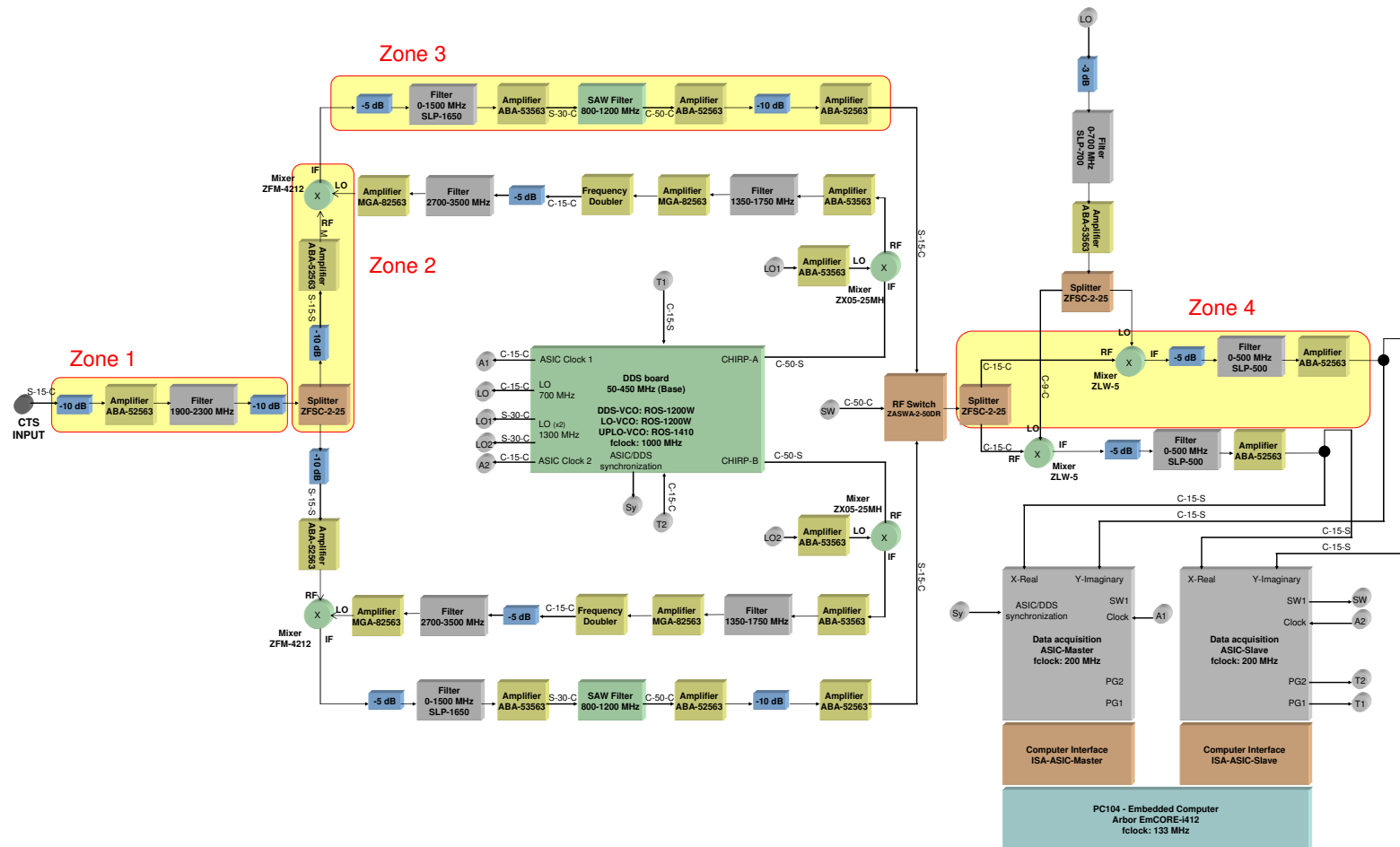


Figure 4.22: Scheme of the CTS displaying the analog and digital parts. Some crucial regions are of especial importance on the RF part, in particular those after the mixing process where the incoming atmospheric signal is down-converted by mixing it with the chirp. These different regions are marked as 'zones'.

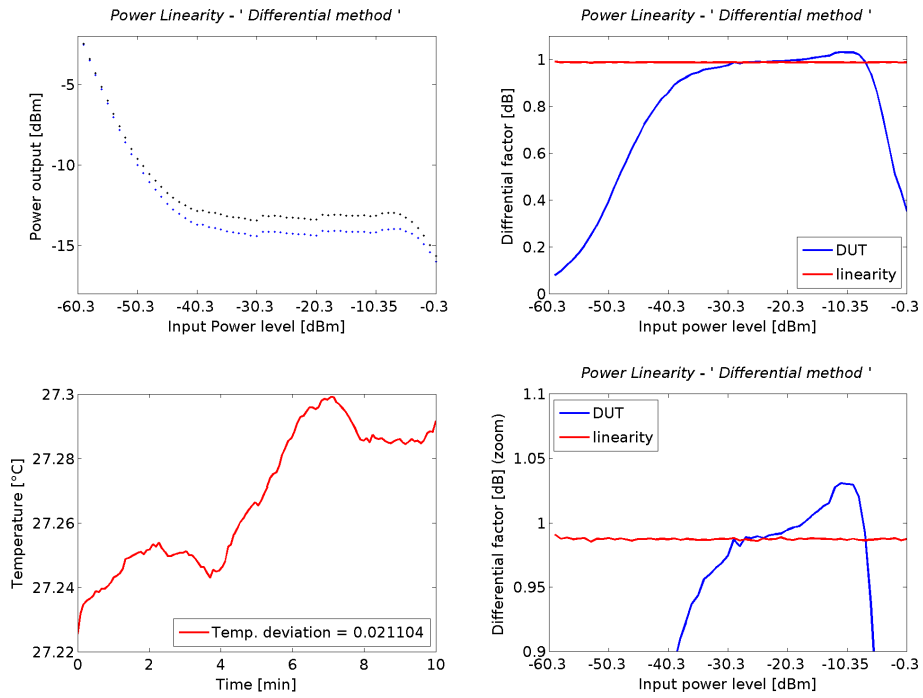


Figure 4.23: High-accuracy method applied over zones 1, 2 and part of 3.

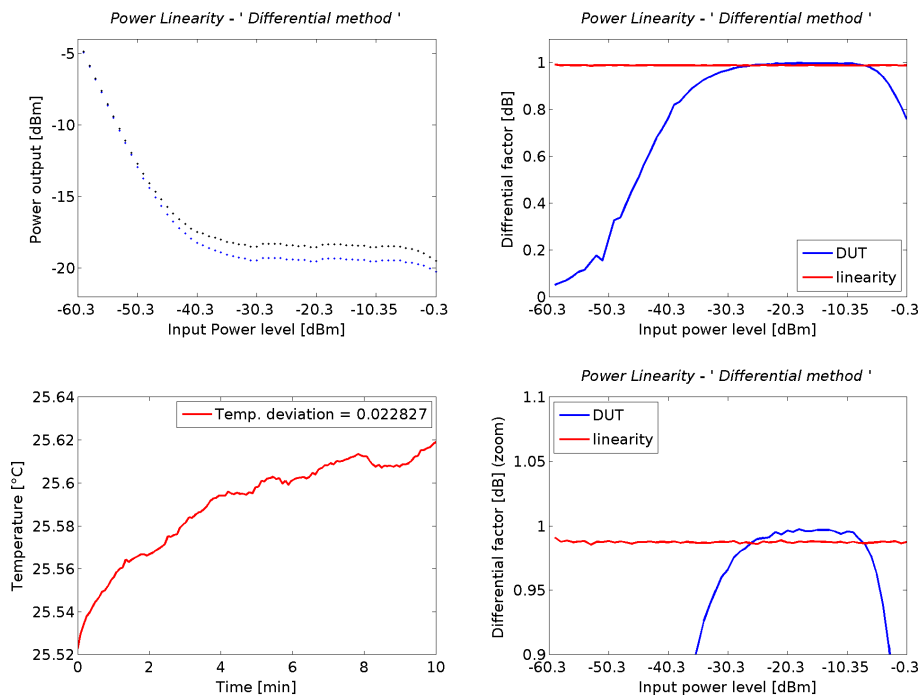


Figure 4.24: High-accuracy method applied over zone 4.

amplifiers, e.g. the ABA51563 and MSA-0735. As previously observed by the 3D analysis, degradation was confirmed in the linearity characteristic at low mixer's input levels above the inherent noise-floor limit.

Through a better and more precise understanding in the behavior of microwave devices, it was possible to exactly define the correspondent input power-level ranges which were best for an optimal linear response in the 400-MHz bandwidth CTS. In that case, possible elements which essentially contributed to the overall system noise (because of added spurious produced in nonlinear regions) might have been avoided. Likely, it was feasible to compare the linearity response of certain zones in both branches of the CTS, wherein differences amongst them might have indicated not only a damaged component, but also unexpected error sources produced by human errors such as incorrectly labeled amplifiers.

For the main mixing stage (i.e. where the incoming atmospheric signal is down-converted), three different RF mixers were evaluated to account for their responses. Even though the MCA-35LH and ZFM-4212 RF mixers are the most suitable ones according to specifications provided by the manufacturer, it is suggested the RF ZFM-15 mixer since the observed response, by both analysis methods, evidenced a better performance.

According to the analysis performed in the different 'zones', a relative good linearity was achieved for input power levels from -30 dBm (low limit) up to -10 dBm (high limit). During this investigation, however, lower values for the low limit were not possible. Consequently, it is suggested further investigation, or probably a different design, to accomplish lower values.

Afterwards, a comparison test was performed between the 400-MHz bandwidth CTS and the SOFIA-GREAT CTS in the ozone radiometer (Fig. 4.25). Owing to a better tuning and design effort, the achieved improvement is translated into smaller deviations in the responses of both spectrometers.

## 4.4 The importance for future developments

In this Chapter, two novel experimental setups were described. These methods are suitable for the detection and analysis of possible nonlinear behavior in singular microwave devices or even an arrangement of them, such as RF stages in a CTS. Based on a differential approach, these novel methods eliminate uncertainties introduced in the test-setup chain, such as step attenuators, noise sources and detector instabilities, which set the facility to investigate the device under test.

It is clear that the observation of linearity in microwave devices using both methods, i.e. the frequency-discrimination capability of the 3D-analysis method plus the low uncertainty (less than 0.1%) offered by the latter high-accuracy method, provide an effective analysis in the identification of nonlinear processes. Their limitations may lie in the upper frequency limits established by the components conforming the experimental setup, such as the noise source, in case of analysis in upcoming spectrometer developments involving higher frequency regimes.

The chance to selectively test single component devices in the CTS with high accuracy and detail proved to be a significant improvement during design of chirp transform spectrometers. Where, by means of a better knowledge in the response of microwave de-

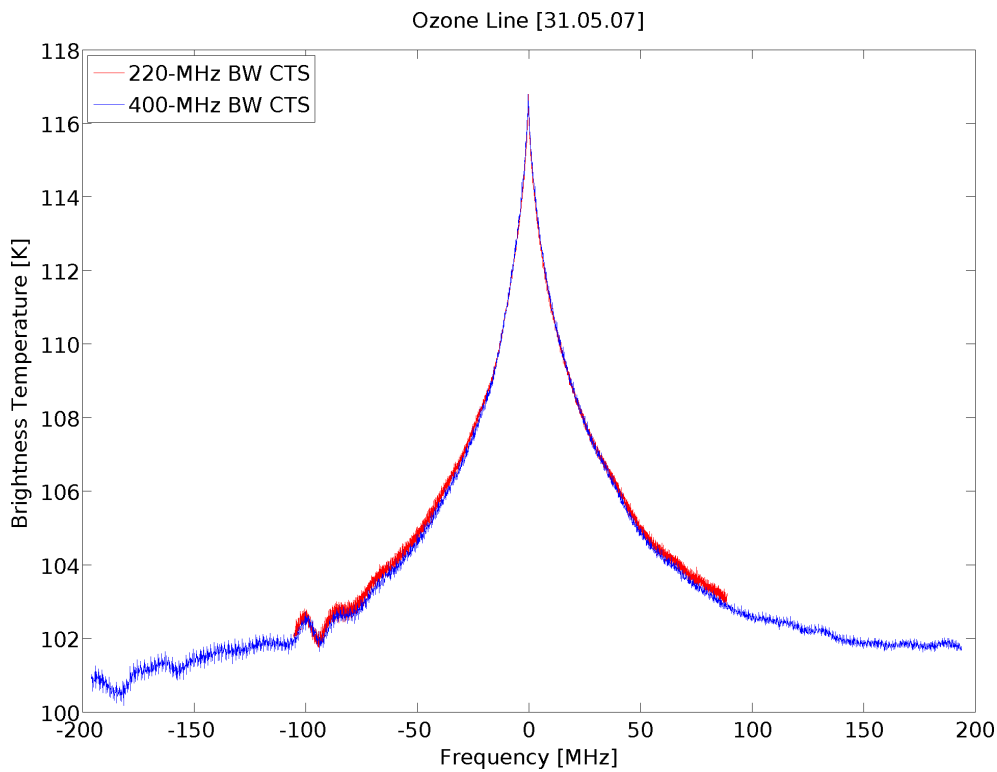


Figure 4.25: In May 2007, the 400-MHz-BW CTS and the SOFIA-GREAT CTS were tested together in the Ozone Radiometer in order to observe any progress. The achieved improvement is smaller deviation in the responses of both spectrometers.

vices, it is possible to rearrange RF stages in order to get the most out of them in terms of linearity. In other words, it is feasible to avoid degradation in the linearity characteristic produced by unexpected error sources not possible to distinguish before (due to the low sensitivity of traditional methods).

To summarize, thanks to a better design allowed by these methods, experimental results in the ozone-radiometer test facility at MPS asserted the improvements in the 400-MHz-BW CTS's response. Therefore, it is confirmed that the overall deviations introduced by nonlinearity in RF stages have been decreased and thus the performance of the backend instrument has been improved.

## 5 Concluding remarks

In this dissertation, the complete description, development and characterization of a new 400-MHz bandwidth chirp transform spectrometer (CTS) with 100 kHz spectral resolution were explained. The newly developed 400-MHz bandwidth CTS has the advantage of broader bandwidth analysis. Moreover, the novel techniques applied to digitally create the chirp signal and the new mixing concept (where the chirp signal is frequency up-converted using RF mixers and later doubled in the RF stage) achieved an 800-MHz bandwidth plus an improvement in the signal-to-noise ratio (SNR) up to 50 dB.

The CTS was applied in atmospheric science by detecting the 142.175-GHz rotational transition of ozone in the Earth's atmosphere. In addition, results were shown from astronomical observations at the HHSMT performed during the observing run of the 73P/Schwassmann-Wachmann 3 comet in May 2006, when it had its closest approach to the Earth.

The effects arising in spectra, from deviations in the spectrometer's ideal linear dynamic range, were accounted for using numerical calculations. In addition, simulations showed how such deviations in the spectra might produce significant changes in the retrieved vertical profile of trace gases. It was stressed that, although the numerical analysis and simulations were focused on the Earth's atmosphere, such an investigation may also apply to the atmospheres of other planets, such as Venus and Mars. The specific retrieval algorithm, used to derive vertical profiles from emission spectra (measured by a microwave system), is sensitive to instrumental noise and errors. It is clear the importance of a high power spectral density accuracy, since the calibration process considers the receiver as a *linear* system. Consequently, systematic errors in the line strength lead to scaling errors on the profile. If such errors are overestimated not all the information can be retrieved from the measurement; if those errors are underestimated, noise may be misinterpreted as spectral features and would contribute spurious signals to the retrieved profile. Even though many systematic errors are corrected by the calibration algorithm, scaling uncertainties can be expected to arise from different sources such as the sky windows, or even the reflectivity of the cold load or the single sideband filter. These phenomena can produce small undesired effects such as standing waves, baseline tilt or baseline ripples. The effects of possible amplitude deviations in the power spectral density, for instance due to nonlinearity, were demonstrated in Section 3.3. As a result, this investigation suggested that deviations at the line center of the ozone's spectral information may produce erratic results in the lower mesosphere and upper stratosphere; meanwhile deviations in the wings indicated aberration in the lower stratosphere of the Earth's atmosphere. Therefore, small effects of nonlinearity in the spectra, as those created by power amplitude deviations, may lead to erratic results in the retrieved volume mixing ratio; for instance, while detecting some molecular species in the mm- and submm-wavelength

range in planetary atmospheres.

The current development of new detectors in heterodyne spectroscopy (e.g., SIS technology) increasingly involves lower radiometric noise which means that all other instrumental uncertainties must be reduced below this noise level in order to keep the overall system's precision. Not surprisingly, this implies that state-of-the-art detectors not only are more sensitive to atmospheric signals (due to low radiometric noise), but also to erratic behavior which thus denotes major deviations from a true brightness temperature value. These facts lead to the need for detecting nonlinear effects with low uncertainty (e.g., less than 0.1%) in order to identify and eliminate any possible kind of instrumental error sources in backend systems.

As stated earlier, nonlinearities may exist in the complete heterodyne system, i.e., the frontend and backend. After providing examples where nonlinearity was evidenced in the measured spectra of heterodyne systems, two novel experiments were developed in order to analyze the nonlinear behavior of the backend spectrometer. Even though the examination of instabilities in the frontend system lies outside the scope of this study, it is strongly suggested in future investigations to account for possible experimental methods in order to analyze the frontend part as well. In the case of backends, these two methods were suitable for detection and analysis of possible nonlinear behavior in singular microwave devices or even an arrangement of them, such as RF stages in a CTS. Based on a differential approach, these novel experiments eliminated uncertainties introduced in the test-setup chain; such as step attenuators, noise sources and detector instabilities; which set the facility to investigate the device under test. It was stated that the observation of linearity in microwave devices using the frequency-discrimination capability of the 3D-tool method plus the low uncertainty (less than 0.1%) provided by the latter high-accuracy method complemented each other and thus provided an effective solution in the identification of nonlinear processes.

The chance to selectively test single component devices in the CTS with high accuracy and detail proved to be a significant improvement during design of chirp transform spectrometers. By means of a better knowledge about the response of microwave devices, it was possible to rearrange RF stages in order to get the most out of them in terms of linearity. In other words, it was feasible to avoid degradation in the linearity characteristic produced by unexpected error sources possibly not distinguished before (due to the low sensitivity of traditional methods).

The limitations of these methods lie primarily in the upper frequency limit imposed by the design of both experiments. This is currently 3.5 GHz and was suitable to fully explore the spectrometer in this thesis. Furthermore, these experiments will also be useful for a full analysis of future spectrometers provided they exhibit a frequency of less than 3.5 GHz (i.e. in the upper frequency regime of their internal components). In future spectrometer designs where the frequency exceeds 3.5 GHz, these experiments are still useful for providing a partial analysis, however, new experiments will need to be developed in order to explore frequencies beyond this limit.

Last but not least, experimental results in the ozone-radiometer test facility at MPS asserted the improvements in the 400-MHz-BW CTS response. In here, it was confirmed that the overall deviations introduced by nonlinearity in the spectrometer had been decreased and thus the performance of the backend instrument had been improved.

# A Receiver calibration

According to Chapter 1, a calibration process is needed in order to establish the relation between the observed noise power and its corresponding temperature. Considering the receiver as a *linear* power measuring device, one can resolve both the antenna temperature,  $T_A$ , and receiver temperature,  $T_R$ , in the following manner.

## A.1 Determination of the antenna temperature, $T_A$

As previously mentioned, the calibration process can be implemented by observing two blackbody emitters at two different temperatures, the so-called hot  $T_H$  and cold  $T_C$  matched resistive loads. Recalling Fig. 1.2, which displays the linear response of the receiver, it follows the relation:

$$\frac{T_A - T_C}{T_H - T_C} = \frac{P_A - P_C}{P_H - P_C}, \quad (\text{A.1})$$

which yields  $T_A$ , defined as

$$T_A = \frac{P_A - P_C}{P_H - P_C}(T_H - T_C) + T_C, \quad (\text{A.2})$$

where  $P_A$  is the power density of the observed object (atmosphere/sky),  $P_H$  is the power density of the hot load,  $P_C$  is the power density of the cold load (represented in counts/cycle),

## A.2 Determination of the receiver temperature, $T_R$

In the absence of an input signal (or external noise source), the receiver system produces an output signal corresponding to its internal noise temperature. This internal noise temperature is originated by the components of the receiver which radiate at their own temperature. The net sum of these temperatures forms the receiver temperature  $T_R$ . Therefore,  $T_R$  can be deduced from Eq. A.2 by considering  $P_A = 0$ , so that:

$$T_R = \frac{0 - P_C}{P_H - P_C}(T_H - T_C) + T_C \quad (\text{A.3})$$

$$= \frac{(-1)}{\frac{P_H}{P_C} - 1}(T_H - T_C) + T_C \quad (\text{A.4})$$

$$= \frac{(-1)}{y - 1}(T_H - T_C) + T_C, \quad (\text{A.5})$$

where  $y = \frac{P_H}{P_C}$  is the so-called 'y-factor'.

It follows

$$T_R = \frac{-T_H + T_C + yT_C - T_C}{y - 1}. \quad (\text{A.6})$$

Thus, the antenna temperature, as observed in Fig. 1.2, is defined as

$$|T_R| = \frac{T_H - yT_C}{y - 1}. \quad (\text{A.7})$$

According to Rohlfis and Wilson (2004),  $T_R$  is similarly deduced by considering the receiver output while observing the matched resistive loads at temperatures  $T_H$  (hot) and  $T_C$  (cold) as:

$$P_H = (T_H + T_R)G, \quad (\text{A.8})$$

$$P_C = (T_C + T_R)G, \quad (\text{A.9})$$

where  $G$  is the internal gain of the receiver system.

Following, the y-factor is

$$y = \frac{P_H}{P_C} = \frac{T_H + T_R}{T_C + T_R}. \quad (\text{A.10})$$

Arithmetically,

$$yT_R + yT_C = T_H + T_R \quad (\text{A.11})$$

$$yT_R - T_R = T_H - yT_C \quad (\text{A.12})$$

$$T_R(y - 1) = T_H - yT_C, \quad (\text{A.13})$$

which finally leads to:

$$T_R = \frac{T_H - yT_C}{y - 1}, \quad (\text{A.14})$$

as derived in Eq. A.7.

## **B Circuit diagrams**

This Appendix is devoted to detailed diagrams involved in the development of the 400-MHz bandwidth CTS. Namely, Fig. B.1 contains the complete system diagram of the current CTS. Furthermore, Table B.1 provides important characteristics of RF components composing this spectrometer.

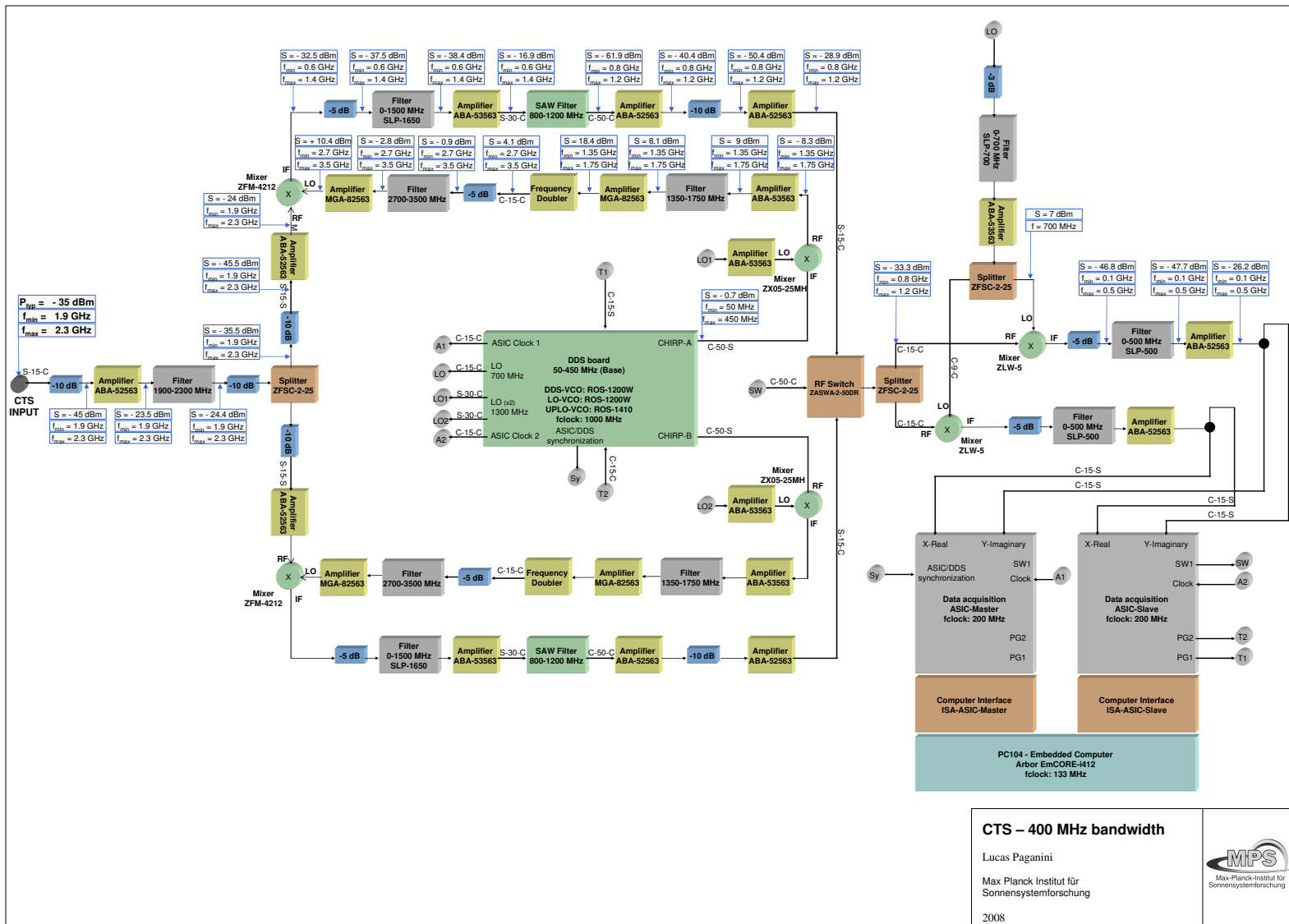


Figure B.1: System diagram of the 400-MHz BW CTS.

Table B.1: RF components in the 400-MHz BW CTS

Component	BW [GHz]	$f_{LO/RF}$ [MHz]	$f_{IF}$ [MHz]	Gain [dB]	Conversion Loss [dB]	P1dB [dBm]	Manufacturer
ABA-52563	DC–3.5	-	-	21.5	3.3	9.8	Agilent
ABA-53563	DC–3.5	-	-	21.5	3.5	12.7	Agilent
MGA-82563	0.1–6	-	-	13.2	2.2	17.3	HP
HMC187MS8 (Frequency Doubler), $InputDriveLevel = 10-20$ dBm	0.85–2	-	-	-	15 dB	-	Hittite
Bandpass Filter	1.35–1.75	-	-	-	0.9	-	MPS
Bandpass Filter	1.9–2.3	-	-	-	0.9	-	MPS
Bandpass Filter	2.7–3.5	-	-	-	1.9	-	MPS
SLP Filters	DC–1.65	-	-	-	0.9	13	Mini-Circuits
ZFSC-2-2500	0.01–2.5	-	-	-	1.4	-	Mini-Circuits
SAW (max inp -10 dBm)	0.8–1.2	-	-	-	45	-	-
ZASWA-2-50DR	DC–5	-	-	-	3	0	Mini-Circuits
ZLW-5 (LO Power +7 dBm)	-	5–1500	10–600	-	8.5	1	Mini-Circuits
ZFM-15 (LO Power +10 dBm)	-	10–3000	10–800	-	8.5	5	Mini-Circuits
ZFM-4212 (LO Power +7 dBm)	-	2000–4200	DC–13000	-	8.5	1	Mini-Circuits
ZX05-25MH (LO Power +13 dBm)	-	5–2500	5–1500	-	9.8	9	Mini-Circuits



## C Observations and data reduction

In this Appendix, some details are provided about the observation campaign of 73P on May, 2006 and its data reduction. For further details about astronomical observations and calibration, the reader is referred to Rohlfs and Wilson (2004), Kutner and Ulich (1981), Mauersberger et al. (1989), Wang et al. (1994) and the Arizona Radio Observatory's documentation (<http://kp12m.as.arizona.edu/documentation.htm>).

### C.1 Calibration and telescope efficiency

In the millimeter and submillimeter wavelength range, the atmosphere has a large influence and can change rapidly, and thus corrections must be frequently performed. That means calibration of antenna temperature ( $T_A^*$ ) to source brightness temperature as measured by the main diffraction beam of the telescope ( $T_{mb}$ ). Here, telescope efficiencies are normally calculated using a measurement of the continuum brightness of a planet (for  $\eta_{mb}$ ) or the Moon (for  $\eta_{fss}$ ).  $T_{mb}$  is defined as

$$T_{mb} = \frac{\eta_l}{\eta_{mb}} T_A^*, \quad (\text{C.1})$$

where  $\eta_l$  is the forward efficiency ( $\eta_l \cong 0.94$ ). The main beam efficiency  $\eta_{mb}$  is defined as:

$$\eta_{mb} = \eta_m^* \eta_l \eta_{fss}, \quad (\text{C.2})$$

where  $\eta_{fss}$  is the forward scattering and spillover efficiency, and  $\eta_m^*$  is the corrected main beam efficiency and is given by

$$\eta_m^* = \frac{T_R^*}{(T_R - T_{bg}) \eta_{cmb}}, \quad (\text{C.3})$$

Definitions:

$T_R \equiv$  Source radiation temperature.

$T_{bg} \equiv$  Brightness temperature of the cosmic background radiation (2.8 K).

$T_R^* \equiv$  Observed source antenna temperature corrected for atmospheric attenuation, radiative loss, and rearward and forward scattering and spillover:

$$T_R^* = \frac{T_A^*}{\eta_{fss}}. \quad (\text{C.4})$$

$\eta_{cmb} \equiv$  Source coupling between a disk source like the planets and a Gaussian telescope beam, which is given by:

$$\eta_{cmb} = 1 - \exp \left[ -\ln(2) \left( \frac{\theta_s}{\theta_b} \right)^2 \right], \quad (\text{C.5})$$

where  $\theta_s$  is the source size and  $\theta_b$  the beam size.

Table C.1: Some useful physical constants and quantities

Symbol	Quantity	Value
$c$	Velocity of light	$2.998 \times 10^8 \text{ m s}^{-1}$
$h$	Planck's constant	$6.626 \times 10^{-34} \text{ J s}$
$k$	Boltzmann's constant	$1.380 \times 10^{-23} \text{ J K}^{-1}$
$\sigma$	Stefan's constant	$5.660 \times 10^{-8} \text{ W m}^{-2} \text{ K}^{-4}$
$e$	Electronic charge	$1.602 \times 10^{-19} \text{ Coulomb}$
$AU$ (Astronomical Unit)	Earth to Sun	$149.6 \times 10^6 \text{ km}$
$R_M$	Earth to Moon	$384,000 \text{ km}$
$R_E$	Earth radius	$6371 \text{ km}$
$R_\odot$	Solar radius	$696,000 \text{ km}$
$L_\odot$	Solar luminosity	$3.83 \times 10^{26} \text{ W}$
$M_\odot$	Solar mass	$1.989 \times 10^{30} \text{ kg}$
$\pi$		$3.14159$
$e$	Base of natural logs	$2.71828$

Table C.2: Operator's log file. Map of the HCN(3-2) emission line of 73P-B

Scan	Source	LST	UT	RA [h : m : s]	Dec [° ' '' ]	Az [° ]	El [° ]	$\Delta$ Az [° ]	$\Delta$ El [° ]	Mode	Freq [GHz]
1039	73P-B/Schw	08:06:00 PM	12:05:00 PM	20:03:39.10	37:44:31.90	359.5	84.9	7	-5	PS	265.89
1040	73P-B/Schw	08:16:00 PM	12:15:00 PM	20:03:52.30	37:43:44.20	339.5	84.4	7	-5	PS	265.89
1041	73P-B/Schw	08:26:00 PM	12:25:00 PM	20:04:05.20	37:42:57.30	324.7	83.4	7	-5	PSM	265.89
1042	73P-B/Schw	08:32:00 PM	12:31:00 PM	20:04:14.50	37:42:23.40	316.7	82.4	7	-5	PSM	265.89
1043	73P-B/Schw	08:39:00 PM	12:38:00 PM	20:04:24.00	37:41:48.60	310.6	81.3	7	-5	PSM	265.89
1044	73P-B/Schw	08:46:00 PM	12:45:00 PM	20:04:32.90	37:41:16.10	306.3	80.2	7	-5	PSM	265.89
1045	73P-B/Schw	08:53:00 PM	12:52:00 PM	20:04:41.90	37:40:42.80	302.9	79	7	-5	PSM	265.89
1046	73P-B/Schw	08:59:00 PM	12:58:00 PM	20:04:50.30	37:40:12.00	300.4	77.9	7	-5	PSM	265.89
1047	73P-B/Schw	09:05:00 PM	01:04:00 PM	20:04:59.00	37:39:39.70	298.3	76.8	7	-5	PSM	265.89
1048	73P-B/Schw	09:11:00 PM	01:10:00 PM	20:05:07.10	37:39:09.50	296.8	75.7	7	-5	PSM	265.89
1049	73P-B/Schw	09:17:00 PM	01:16:00 PM	20:05:15.60	37:38:37.70	295.5	74.5	7	-5	PSM	265.89
1050	73P-B/Schw	09:23:00 PM	01:22:00 PM	20:05:23.60	37:38:08.00	294.4	73.4	7	-5	PSM	265.89
1051	73P-B/Schw	09:30:00 PM	01:28:00 PM	20:05:32.00	37:37:36.50	293.6	72.2	7	-5	PSM	265.89
1052	73P-B/Schw	09:35:00 PM	01:34:00 PM	20:05:39.80	37:37:07.20	292.9	71.1	7	-5	PSM	265.89
1053	73P-B/Schw	09:41:00 PM	01:40:00 PM	20:05:48.10	37:36:36.00	292.3	69.9	7	-5	PSM	265.89
1054	73P-B/Schw	09:47:00 PM	01:46:00 PM	20:05:55.80	37:36:06.80	291.9	68.8	7	-5	PSM	265.89
1055	73P-B/Schw	09:54:00 PM	01:53:00 PM	20:06:05.80	37:35:29.00	291.4	67.4	7	-5	PSM	265.89
1056	73P-B/Schw	10:00:00 PM	01:59:00 PM	20:06:13.50	37:35:00.00	291.2	66.3	7	-5	PSM	265.89
1057	73P-B/Schw	10:06:00 PM	02:05:00 PM	20:06:21.60	37:34:29.20	291	65.2	7	-5	PSM	265.89
1058	73P-B/Schw	10:12:00 PM	02:10:00 PM	20:06:29.20	37:34:00.20	290.8	64.1	7	-5	PSM	265.89
1059	73P-B/Schw	10:17:00 PM	02:16:00 PM	20:06:37.20	37:33:29.60	290.7	63	7	-5	PSM	265.89
1060	73P-B/Schw	10:23:00 PM	02:22:00 PM	20:06:44.80	37:33:00.80	290.7	61.9	7	-5	PSM	265.89
1061	73P-B/Schw	10:29:00 PM	02:28:00 PM	20:06:52.70	37:32:30.30	290.7	60.8	7	-5	PSM	265.89
1062	73P-B/Schw	10:34:00 PM	02:33:00 PM	20:07:00.20	37:32:01.70	290.7	59.7	7	-5	PSM	265.89
1063	73P-B/Schw	10:40:00 PM	02:39:00 PM	20:07:08.10	37:31:31.10	290.7	58.6	7	-5	PSM	265.89
1064	73P-B/Schw	10:46:00 PM	02:44:00 PM	20:07:15.50	37:31:02.70	290.8	57.5	7	-5	PSM	265.89
1065	73P-B/Schw	10:51:00 PM	02:50:00 PM	20:07:23.40	37:30:32.20	290.9	56.4	7	-5	PSM	265.89

Table C.3: Operator's log file. Map of the HCN(3-2) emission line of 73P-C

Scan	Source	LST	UT	RA [h : m : s]	Dec [° ' '' ]	Az [° ]	El [° ]	$\Delta$ Az [° ]	$\Delta$ El [° ]	Mode	Freq [GHz]
1005	73P-C/Schw	05:04:00 PM	09:03:00 AM	20:46:03.60	26:38:54.90	82.7	41.9	5	-2	PS	265.89
1006	73P-C/Schw	05:11:00 PM	09:10:00 AM	20:46:11.00	26:38:15.20	83.4	43.3	5	-2	PS	265.89
1007	73P-C/Schw	05:18:00 PM	09:17:00 AM	20:46:18.70	26:37:34.60	84.2	44.8	5	-2	PSM	265.89
1007	73P-C/Schw	05:20:00 PM	09:19:00 AM	20:46:20.90	26:37:23.00	84.5	45.2	5	-2	PSM	265.89
1008	73P-C/Schw	05:25:00 PM	09:25:00 AM	20:46:26.60	26:36:52.70	85.1	46.3	5	-2	PSM	265.89
1009	73P-C/Schw	05:31:00 PM	09:30:00 AM	20:46:32.70	26:36:20.20	85.8	47.4	5	-2	PSM	265.89
1010	73P-C/Schw	05:36:00 PM	09:36:00 AM	20:46:38.40	26:35:49.90	86.4	48.5	5	-2	PSM	265.89
1011	73P-C/Schw	05:42:00 PM	09:41:00 AM	20:46:44.50	26:35:17.30	87.1	49.7	5	-2	PSM	265.89
1012	73P-C/Schw	05:47:00 PM	09:47:00 AM	20:46:50.20	26:34:46.60	87.7	50.8	5	-2	PSM	265.89
1013	73P-C/Schw	05:53:00 PM	09:52:00 AM	20:46:56.40	26:34:13.70	88.5	52	5	-2	PSM	265.89
1014	73P-C/Schw	05:58:00 PM	09:58:00 AM	20:47:02.10	26:33:42.80	89.1	53.1	5	-2	PSM	265.89
1015	73P-C/Schw	06:04:00 PM	10:03:00 AM	20:47:08.30	26:33:09.60	89.9	54.3	5	-2	PSM	265.89
1016	73P-C/Schw	06:09:00 PM	10:09:00 AM	20:47:14.10	26:32:38.40	90.6	55.4	5	-2	PSM	265.89
1017	73P-C/Schw	06:15:00 PM	10:15:00 AM	20:47:20.30	26:32:05.10	91.5	56.6	5	-2	PSM	265.89
1018	73P-C/Schw	06:21:00 PM	10:20:00 AM	20:47:26.10	26:31:33.70	92.3	57.7	5	-2	PSM	265.89
1019	73P-C/Schw	06:27:00 PM	10:26:00 AM	20:47:32.30	26:31:00.00	93.1	58.9	5	-2	PSM	265.89
1019	73P-C/Schw	06:31:00 PM	10:31:00 AM	20:47:37.30	26:30:33.00	93.9	59.9	5	-2	PSM	265.89
1020	73P-C/Schw	06:37:00 PM	10:36:00 AM	20:47:43.10	26:30:01.20	94.8	61	5	-2	PSM	265.89
1021	73P-C/Schw	06:43:00 PM	10:42:00 AM	20:47:49.40	26:29:27.20	95.8	62.2	5	-2	PSM	265.89
1022	73P-C/Schw	06:48:00 PM	10:47:00 AM	20:47:55.30	26:28:55.10	96.7	63.3	5	-2	PSM	265.89
1023	73P-C/Schw	06:54:00 PM	10:53:00 AM	20:48:01.60	26:28:20.60	97.9	64.5	5	-2	PSM	265.89
1024	73P-C/Schw	07:00:00 PM	10:59:00 AM	20:48:07.50	26:27:48.20	99	65.7	5	-2	PSM	265.89
1025	73P-C/Schw	07:06:00 PM	11:05:00 AM	20:48:13.90	26:27:13.20	100.3	66.9	5	-2	PSM	265.89
1026	73P-C/Schw	07:11:00 PM	11:10:00 AM	20:48:19.90	26:26:40.30	101.6	68.1	5	-2	PSM	265.89
1027	73P-C/Schw	07:17:00 PM	11:17:00 AM	20:48:26.40	26:26:04.90	103.1	69.3	5	-2	PSM	265.89
1028	73P-C/Schw	07:23:00 PM	11:22:00 AM	20:48:32.40	26:25:31.60	104.6	70.4	5	-2	PSM	265.89
1029	73P-C/Schw	07:29:00 PM	11:28:00 AM	20:48:38.90	26:24:55.70	106.4	71.7	5	-2	PSM	265.89
1030	73P-C/Schw	07:35:00 PM	11:34:00 AM	20:48:45.10	26:24:21.70	108.4	72.8	5	-2	PSM	265.89
1031	73P-C/Schw	07:41:00 PM	11:40:00 AM	20:48:51.70	26:23:45.30	110.7	74	5	-2	PSM	265.89

## D Details of devices under test

The following tables contain some useful information about the devices under test which were used in the 3D-analysis and high-accuracy methods. These include, in case of amplifiers: the operating frequency, power gain, power gain flatness, noise figure, output power at 1-dB gain compression, output third order intercept point, device voltage and current, and the manufacturer. In case of mixers: LO/RF operating frequency, IF operating frequency, output power at 1-dB gain compression, conversion loss, LO-RF isolation, LO-IF isolation, and finally, the manufacturer:

Table D.1: Devices under test: Amplifiers

	Symbol	Unit	ABA-51563	ABA-52563	ABA-53563	ABA-54563	MSA-0735	MGA-82563
Operating Frequency	$f$	GHz	DC ~ 3.5	DC ~ 3.5	DC ~ 3.5	DC ~ 3.4	DC ~ 2.4	0.1–6
Power Gain ( $ S_{21} ^2$ )	$Gp$	dB	21.5	21.5	21.5	23.0	13.5	13.2
Power Gain Flatness (0.1–3.5 GHz)	$\Delta Gp$	dB	1.3	2.0	2.7	3.0	0.6	0.35
Noise Figure	$NF$	dB	3.7	3.3	3.5	4.4	4.5	2.2
Output Power at 1 dB Gain Compression	$P1dB$	dBm	1.8	9.8	12.7	16.1	5.5	17.3
Output Third Order Intercept Point	$OIP3$	dBm	11.4	19.9	22.9	27.8	19.0	31.0
Device Voltage	$V_d$	V	5	5	5	5	4	3
Device Current	$I_{cc}$	mA	18	35	46	79	60	84
Manufacturer			Agilent	Agilent	Agilent	Agilent	HP	HP

Table D.2: Devices under test: Mixers

	Symbol	Unit	ZFM-15	ZFM-4212	MCA-35LH
LO/RF Operating Frequency	$f_{LO}/f_{RF}$	MHz	10–3000	2000–4200	500–3500
IF Operating Frequency	$f_{IF}$	MHz	10–800	DC–1300	10–1500
LO Power	$P_{LO}$	dBm	10	7	10
Output Power at 1 dB Gain Compression	$P1dB$	dBm	5	1	6
Conversion Loss	$CL$	dB	6.13	5.44	6.9
LO-RF Isolation	$L - R$	dB	35	25	29
LO-IF Isolation	$L - I$	dB	30	18	26
Manufacturer			Mini-Circuits	Mini-Circuits	Mini-Circuits

# Bibliography

- Allen, J. B., 1977, Short Term Spectral Analysis, Synthesis, and Modification by Discrete Fourier Transform, *IEEE Trans. Acoust., Speech, and Signal Processing*, ASSP-25, 3, 235–238.
- Allen, J. B., Rabiner, L. R., 1977, A Unified Approach to Short-Time Fourier Analysis and Synthesis, *Proceedings of the IEEE*, 65, 11, 1558–1564.
- Allen, M., Lunine, J. I., Yung, Y. L., 1984, The vertical distribution of ozone in the mesosphere and lower thermosphere, *J. Geophys. Res.*, 89, 4841–4872.
- Andrews, D. G., 2000, *An Introduction to Atmospheric Physics*, Cambridge Univ. Press.
- Arzeni, C., Manes, G., Masotti, L., 1975, Programmable Signal Processing by Analog Chirp-Transformation Using SAW Devices, *Proceedings of the IEEE*, 1975 Ultrasonics Symposium, 371–376.
- Baars, J. W. M., Martin, R. N., Mangum, J. G., McMullin, J. P., Peters, W. L., 1999, The Heinrich Hertz Telescope and the Submillimeter Telescope Observatory, *The Publications of the Astronomical Society of the Pacific*, 111, 759, 627–646.
- Beaudin, G., Gulkis, S., Frenking, M., Hartogh, P., Allen, M., Bockelée-Morvan, D., Crovisier, J., Despois, D., Encrenaz, P., Encrenaz, T., Germain, B., Hofstadter, M., Ip, W., Janssen, M., Lellouch, E., Mann, I., Muhleman, D., Rauer, H., Schloerb, F.P., Spilker, T., 1998, A Microwave Radiometer/Spectrometer for the Rosetta Orbiter, *Proceedings of the 2nd ESA Workshop on Millimetre Wave Technology and Applications*, ESA WPP149, 43–48.
- Bedrosian, E., Rice, S. O., 1971, The output properties of volterra system (nonlinear systems with memory) driven by harmonic and Gaussian inputs, *Proceedings of the IEEE*, 59, 1968–1707.
- Benz, A. O., Grigis, P. C., Hungerbühler, V., Meyer, H., Monstein, C., Stuber, B., Zardet, D., 2005, A broadband FFT spectrometer for radio and millimeter astronomy, *Astronomy & Astrophysics*, 442, 2, 767–773.
- Berceli, T., Marozsák, T., 2006, A new microwave amplifier nonlinearity measurement method, *Proc. of the EuMA*, 255–258, doi: 10.1109/EUMC.2006.281286.
- Berger, U., von Zahn, U., 1999, The two-level structure of the mesopause: A model study, *J. Geophys. Res.*, 104, 22083–22093.

- Bertocco, M., Sona, A., 2004, On the Power Measurement via a Spectrum Analyzer, Proc. of the 21st IEEE Instrumentation and Measurement Technology Conference, 2, 958–963.
- Bich, W., Cox, M. G., Harris, P. M., 2006, Evolution of the 'Guide to the Expression of Uncertainty in Measurement', *Metrologia*, 43, 4, S161–S166.
- Bieging, J. H., Shaked, S., Gensheimer, P. D., 2000, Submillimeter- and Millimeter-Wavelength Observations of SIO and HCN in Circumstellar Envelopes of AGB Stars, *ApJS*, 543, 2, 897–921.
- Biver, N., Bockelée-Morvan, D., Crovisier, J., Davies, J. K., Matthews, H. E., Wink, J. E., Rauer, H., Colom, P., Dent, W. R. F., Despois, D., Moreno, R., Paubert, G., Jewitt, D., Senay, M., 1999, Spectroscopic Monitoring of Comet C/1996 B2 (Hyakutake) with the JCMT and IRAM Radio Telescopes, *The Astronomical Journal*, 118, 4, 1850–1872.
- Blake, G. A., Qi, C., Hogerheijde, M. R., Gurwell, M. A., Muhleman, D. O., 1998, Sublimation from icy jets as a probe of the interstellar volatile content of comets, *Nature*, 398, 213–216.
- Bohnhardt, H., Kaufl, H. U., Keen, R., Camilleri, P., Carvajal, J., Hale, A., 1995, Comet 73P/Schwassmann-Wachmann 3, *IAU Circ.*, 6274, 1.
- Borremans, J., De Locht, L., Wambacq, P., Rolain, Y., 2007, Nonlinearity Analysis of Analog/RF Circuits Using Combined Multisine and Volterra Analysis, Design, Automation & Test in Europe Conference & Exhibition, 1–6, doi: 10.1109/DATE.2007.364601.
- Brillet, J., 1989, A theoretical study of ozone measurements made with ground-based microwave sensors, *Journal of Geophysical Research*, 94, 12833–12850.
- Burke, B., Graham-Smith, F., 1997, *An Introduction to Radio Astronomy*, Cambridge Univ. Press.
- Carr, P. H., Devito, P. A., Szabo, T. L., 1972, The Effect of Temperature and Doppler Shift on the Performance of Elastic Surface Wave Encoders and Decoders, *IEEE Transactions on Sonics and Ultrasonics*, 19, 3, 357–367.
- Chandrasekhar, S., 1960, *Radiative Transfer*, Dover.
- Charnley, S. B.; Rodgers, S. D.; Butner, H. M.; Ehrenfreund, P., 2002, Chemical Processes in Cometary Comae, *Earth, Moon, and Planets*, 90, 1, 349–360.
- Cole, A. E., Court, A., Kantor, A. J., 1965, Model atmospheres, *Handbook of Geophysics and Space Environment*, Cambridge Res. Labs.
- Connor, B. J., Siskind, D. E., Tsou, J. J., Parrish, A., Remsberg, E. E., 1994, Ground-based microwave observations of ozone in the upper stratosphere and mesosphere, *J. Geophys. Res.*, 99, 16757–16770.
- Crovisier, J., Encrenaz, T., 2000, *Comet Science*, Cambridge Univ. Press.

- Darlington, S., 1964, Demodulation of wide band low-power FM signals, *Bell Syst. Tech. J.*, 43, 339.
- de La Noë, J., Lezeaux, O., Guillemin, G., Lauqué, R., Baron, P., Ricaud, P., 1998, A ground-based microwave radiometer dedicated to stratospheric ozone monitoring, *J. Geophys. Res.*, 103, 22147–22161.
- Dello Russo, N., Vervack, R. J., Weaver, H. A., Biver, N., Bockelée-Morvan, Crovisier, J., Lisse, C. M., 2007, Compositional homogeneity in the fragmented comet 73P/Schwassmann-Wachmann 3, *Nature*, 448, 172–175.
- Despois, D., Crovisier, J., Bockelee-Morvan, D., Gerard, E., Schraml, J., 1986, Observations of hydrogen cyanide in comet Halley, *Astronomy & Astrophysics*, 160, 2, L11–L12.
- Drahus, M., Küppers, M., Jarchow, C., Paganini, L., Hartogh, P., Villanueva, G., 2007, The HCN molecule as a tracer of the nucleus rotation of comet 73P-C/Schwassmann-Wachmann 3, *A&A*, submitted.
- Fray, N., Bénilan, Y., Cottin, H., Gazeau, M.-C., Crovisier, J., The origin of the CN radical in comets: A review from observations and models, *Planetary and Space Science*, 53, 1243–1262.
- Friedel, D. N., Remijan, A. J., Snyder, L. E., A’Hearn, M. F., Blake, G. A., de Pater, I., Dickel, H. R., Forster, J. R., Hogerheijde, M. R., Kraybill, C., Looney, L. W., Palmer, P., Wright, M. C. H., 2005, BIMA Array Detections of HCN in Comets LINEAR (C/2002 T7) and NEAT (C/2001 Q4), *The Astrophysical Journal*, 630, 1, 623–630.
- Gladman, B., 2005, The Kuiper Belt and the Solar System’s Comet Disk, *Science*, 307, 5706, 71–75.
- Glesser, L. J., 1998, Assessing uncertainty in measurement, *Stat. Sci.*, 13, 277–290.
- Gordy, W., Cook, R. L., 1970, *Microwave Molecular Spectra*, Chemical Applications of Spectroscopy, Wiley.
- Gulkis, S., Allen, M., Backus, C., Beaudin, G., Biver, N., Bockelée-Morvan, D., Crovisier, J., Despois, D., Encrenaz, P., Frerking, M., Hofstadter, M., Hartogh, P., Ip, W., Janssen, M., Kamp, L., Koch, T., Lellouch, E., Mann, I., Muhleman, D., Rauer, H., Schloerb, P., Spilker, T., 2007, Remote sensing of a comet at millimeter and submillimeter wavelengths from an orbiting spacecraft, *Planetary and Space Science*, 55, 9, 1050–1057.
- Harris, A. I., Isaak, K. G., Zmuidzinas, J., 1998, WASP: wideband spectrometer for heterodyne spectroscopy, *Proceedings SPIE*, 3357, 384–394.
- Harris, A. I., 2002, Spectrometers for Heterodyne Detection, *Proc. of the Far-IR, Sub-mm & mm Detector Technology Workshop*, NASA/CP-211408.
- Harris, A. I., 2003, Heterodyne spectrometers with very wide bandwidths, *Proceedings of the SPIE*, 4855, 279–289.

- Hartfuss, H. J., Geist, T., Hirsch, M., 1997, Heterodyne methods in millimetre wave plasma diagnostics with applications to ECE, interferometry and reflectometry, *M. Plasma Phys. Control. Fusion*, 39, 1693–1769.
- Hartogh, P., 1989, Chirptransformations-Spektrometer für die passive Millimeterwellenradiometrie: Messung der 142 GHz Emissionslinie des atmosphärischen Ozons, Ph.D. thesis (University of Göttingen)
- Hartogh, P., 1998, High resolution chirp transform spectrometer for middle atmospheric sounding, *Proc. of SPIE*, 3220, 115–124.
- Hartogh, P., 2004, Microwave Investigation of Planets, *Proc. 37th. ESLAB Symposium*, ESA SP-543.
- Hartogh, P., Hartmann, G., 1990, A high-resolution chirp transform spectrometer for microwave measurements, *Meas. Sci. Technol.*, 1, 592–595.
- Hartogh, P., Jarchow, C., 1995, Groundbased detection of middle atmospheric water vapor and ozone, *Proc. SPIE*, 2586, 188–213.
- Hartogh, P., Jarchow, C., Sonnemann, G.R., Grygalashvyly, M., 2004, On the spatiotemporal behaviour of ozone within the upper mesosphere/mesopause region under nearly polar night conditions, *J. Geophys. Res.* 109, D18303.
- Heiter, G. L., 1973, Characterization of Nonlinearities in Microwave Devices and Systems, *IEEE Transactions on Microwave Theory and Techniques*, MTT-21, 12, 797–805.
- Hogerheijde, M. R., de Pater, I., Wright, M., Forster, J. R., Snyder, L. E., Remijan, A., Woodney, L. M., A’Hearn, M. F., Palmer, P., Kuan, Y.-J., Huang, H.-C., Blake, Geoffrey A., Qi, C., Kessler, J., Liu, S.-Y., 2004, Combined BIMA and OVRO Observations of Comet C/1999 S4 (LINEAR), *The Astronomical Journal*, 127, 4, 2406–2412.
- Hofstadter, M. D., Hartogh, P., McMullin, J. P., Martin, R. N., Jarchow, C., Peters, W., 1999, A Search for Variability in the HCN to H<sub>2</sub>CO Ratio in Comet Hale-Bopp, *Earth, Moon and Planets*, 78, 1/3, 53–61.
- Holland, K., Howes, J., 2002, Improvements to the microwave mixer and power sensor linearity measurement capability at the National Physical Laboratory, *IEE Proc. Sci. Meas. Technol.*, 149, 6, 329–332.
- Huebner, W. F., Buhl, D., Snyder, L. E., 1974, HCN radio emission from Comet Kohoutek /1973f/, *Icarus*, 23, 580–584.
- Iida, H., Widarta, A., Kawakami, T., Komiyama, K., 2006, An accurate microwave attenuation measurement system using an inductive voltage divider based on a single-channel IF substitution, *Meas. Sci. Technol.*, 17, 1947–1949.
- Irvine, W. M., Dickens, J. E., Lovell, A. J., Schloerb, F. P., Senay, M., Bergin, E. A., Jewitt, D., Matthews, H. E., 1997, The HNC/HCN Ratio in Comets, *Earth, Moon, and Planets*, 78, 1/3, 29–35.

- Jack, M. A., Grant, P. M., Collins, J. H., 1980, The theory, design, and applications of surface acoustic wave Fourier-transform processors, *IEEE Proceedings*, 68, 450–468.
- Janssen, M. A., 1993, *Atmospheric Remote Sensing by Microwave Radiometry*, John Wiley & Sons.
- Jarchow, C., 1998, Bestimmung atmosphärischer Wasserdampf- und Ozon-profile mittels bodengebundener Millimeterwellen-Fernerkundung, MPAE-W-016-99-06, Ph.D. thesis.
- Jarchow, C., Hartogh, P., 1995, Retrieval of data from ground-based microwave sensing of the middle atmosphere: Comparison of two inversion techniques, *Proc. SPIE in Global Process Monitoring and Remote Sensing of the Ocean and Sea Ice*, 2586, 196–205.
- Keen, N., Spurett R., Wylde R., 1995, An absolute blackbody source for radiometer calibration at sub-millimeter wavelengths, *Proceedings of the ESA Workshop on Millimeter Wave Techniques and Applications*, 4.2.1–4.2.10.
- Klauder, J. R., Price, A. C., Davlington, S., Albersheim, W. J., 1960, The theory and design of chirp radars, *Bell Syst. Tech. J.*, 39, 745–808.
- Klein, B., Philipp, S. D., Krämer, I., Kasemann, C., Güsten, R., Menten, K. M., 2006, The APEX digital Fast Fourier Transform Spectrometer, *Astronomy & Astrophysics*, 454, 2, 29–32.
- Kleipool, Q. L., Whyborn, N. D., Helmich, F. P., Schrijver, H., Goede, A. P. H., Lelieveld, J., Künzi, K., 2000, Error Analysis of a Heterodyne Submillimeter Sounder for the Detection of Stratospheric Trace Gases, *Applied Optics*, 39, 30, 5518–5530.
- Kraus, J. D., 1986, *Radio Astronomy*, Cygnus-Quasar Books.
- Kramer, M. L., Jones, D. L., 1994, *Proceedings of the IEEE-SP Int. Symp. on Time-Frequency and Time-Scale Analysis*, 264–267.
- Kubat, F., Ruile, W., Hesjedal, T., Stotz, J., Rosler, U., Reindl, L.M., 2004, Calculation and experimental verification of the acoustic stress at GHz frequencies in SAW resonators, *IEEE Transactions on Ultrasonics, Ferroelectrics and Frequency Control*, 51, 11, 1437–1448.
- Kuntz, M., Hochschild, G., Krupa, R., 1997, Retrieval of ozone mixing ratio profiles from ground-based millimeter wave measurements disturbed by standing waves, *Journal of Geophysical Research*, 102, D18, 21965–21976.
- Kutner, M. L., Ulich, B. L., 1981, Recommendations for calibration of millimeter-wavelength spectral line data, *ApJS*, 1, 250, 341–348.
- Küppers, M., Hartogh, P., Paganini, L., 2006, The homogeneity of cometary nuclei: Observations of split comet 73/P Schwassmann-Wachmann 3, *Submillimeter Telescope Observatory proposal*.

- Lellouch, E., Gerin, M., Combes, F., Atreya, S., Encrenaz, T., 1989, Observations of the  $J = 1-0$  CO lines in the Mars atmosphere - Radiodetection of  $^{13}\text{CO}$  and monitoring of  $^{12}\text{CO}$ , *Icarus*, 77, 1, 414–438.
- Li, X., 2008, Wideband-CTS development, Ph.D. thesis (Albert-Ludwigs-Universität Freiburg im Breisgau), in preparation.
- Maas, S. A., 2003, *Nonlinear Microwave and RF Circuits*, Artech House.
- Maines, J. D., Paige, E. G. S., 1976, Surface-acoustic-wave devices for signal processing applications, *IEEE Proceedings*, 64, 639–652.
- Mauersberger, R., Guelin, M., Martin-Pintado, J., Thum, C., Cernicharo, J., Hein, H., Navarro, S., 1989, Line calibrators at  $\lambda = 1.3, 2,$  and  $3$  mm, *Astronomy and Astrophysics Supplement Series*, 79, 2, 217–261.
- Mertz, L., 1965, *Transformations in Optics*, John Wiley & Sons.
- Morgan, D. P., 1998, History of SAW devices, *IEEE Proceedings, Frequency Control Symposium*, 439–460, DOI: 10.1109/FREQ.1998.717937.
- Mumma, M. J., DiSanti, M. A., dello Russo, N., Fomenkova, M., Magee-Sauer, K., Kaminski, C. D., Xie, David X., 1996, Detection of abundant ethane and methane, along with carbon monoxide and water, in comet C/1996 B2 Hyakutake: Evidence for interstellar origin, *Science*, 272, 5266, 1310–1314.
- Murk, A., Kikuchi, K., Inatani, J., 2005, Linearity Measurements of the 640 GHz SIS Mixer for JEM/SMILES, 16th International Symposium on Space Terahertz Technology, 1–4.
- Müller, S. C., Murk, A., Monstein, C., Kämpfer, N., Meyer, H., 2006, Microwave remote sensing of stratospheric trace gases using digital Fast Fourier Transform spectrometers, *GeMiC 2006 - Conference Proceedings*.
- Narasimhan, S. V., Pavanalatha, S., 2004, Estimation of evolutionary spectrum based on short time Fourier transform and modified group delay, *Signal Processing*, 84, 11, 2139–2152.
- Paganini, L., Hartogh, P., 2006, Description of a New 400 MHz bandwidth Chirp Transform Spectrometer, *Advances in Geosciences, Vol. 7: Planetary Science* (Eds. Anil Bhardwaj et al.), World Scientific Publishing Co., 55–68. ISBN-13: 978-981-270-986-8.
- Paganini, L., Hartogh, P., Reindl, L., 2007, An improved method for nonlinearity detection applied to a new 400-MHz Chirp Transform Spectrometer, *Transactions on Systems, Signals and Devices*, accepted for publication.
- Reindl, L., Ruppel, C.C.W., Kirmayr, A., Stockhausen, N., Hilhorst, M.A., Balendonck, J., 2001, Radio-Requestable Passive SAW Water-Content Sensor, *IEEE Transactions on Microwave Theory and Techniques*, 49, 4, 803–808.

- Reindl, L., Pohl, A., Scholl, G., Weigel, R., 2001, SAW-based radio sensor systems, *IEEE Sensors Journal*, 1, 1, 69–78.
- Reindl, L. M., Shrena, I. M., 2004, Wireless measurement of temperature using surface acoustic waves sensors, *IEEE Transactions on Ultrasonics, Ferroelectrics and Frequency Control*, 51, 11, 1457–1463.
- Reinhardt, V. S., Shih, Y. C., Toth, P. A., Reynolds, S. C., Berman, A. L., 1995, Methods for Measuring the Power Linearity of Microwave Detectors for Radiometric Applications, *IEEE Transactions on Microwave Theory and Techniques*, 43, 4, 715–720.
- Rodgers, C. D., 1976, Retrieval of Atmospheric Temperature and Composition From Remote Measurements of Thermal Radiation, *Reviews of Geophysics and Space Physics*, 14, 4, 609–624.
- Rodgers, S. D., Charnley, S. B., 1998, HNC and HCN in Comets, *Astrophysical Journal*, 501, L227.
- Rodgers, S. D., Charnley, S. B., 2002, On the origin of HNC in Comet Lee, *Monthly Notices of the Royal Astronomical Society*, 323, 1, 84–92.
- Rodgers, S. D., Butner, H. M., Charnley, S. B., Ehrenfreund, P., 2003, The HNC/HCN ratio in comets: Observations of C/2002 C1 (Ikeya-Zhang), *Advances in Space Research*, 31, I12, 2577–2582.
- Rohlfs, K., Wilson, T. L., 2004, *Tools of Radio Astronomy* (4th. edition), Springer-Verlag.
- Seele, C., Hartogh, P., 1999, Water vapor of the polar middle atmosphere: Annual variation and summer mesosphere conditions as observed by ground-based microwave spectroscopy, *Geophys. Res. Lett.*, 26, 11, 1517–1520.
- Seele, C., 1999, An extended inversion technique for remotely sensed microwave spectra - Tests on the influence of baseline disturbances, noise and apriori information, Internal MPAE-W-016-99-01 Doc.
- Schieder, R., Kramer, C., 2001, Optimization of heterodyne observations using Allan variance measurements, *Astronomy & Astrophysics*, 373, 746–756.
- Slobodnik, A. J., 1976, Surface acoustic waves and SAW materials, *IEEE Proceedings*, 64, 5, 581–595.
- Sonnemann, G. R., Hartogh, P., Jarchow, C., Grygalashvyly, M., Berger, U., 2007, On the winter anomaly of the night-to-day ratio of ozone in the middle to upper mesosphere in middle to high latitudes, *Advances in Space Research*, 40, 846–854.
- Townes, C. H., Schawlow, A. L., 1975, *Microwave Spectroscopy*, Dover.
- Ulaby, F., Moore, R., Fung, A., 1981, *Microwave Remote Sensing*, Addison-Wesley Publishing Co.

- Ulich, B. L., Haas, R. W., 1976, Absolute calibration of millimeter-wavelength spectral lines, *ApJS*, 30, 247–258.
- Veal, J. M., Snyder, L. E., Wright, Melvyn, Woodney, L. M., Palmer, Patrick, Forster, J. R., de Pater, Imke, A’Hearn, M. F., Kuan, Y.-J., 2002, An Interferometric Study of HCN in Comet Hale-Bopp (C/1995 O1), *The Astronomical Journal*, 119, 3, 1498–1511.
- Vila-Vilaró, B., Cepa, J., Butner, H. M., 2003, CO (3-2) Observations of Early-Type Galaxies with the Heinrich Hertz Telescope, *ApJS*, 594, 1, 232–246.
- Villanueva, G., 2004, The High Resolution Spectrometer for SOFIA-GREAT: Instrumentation, Atmospheric Modeling and Observations, Ph.D. thesis (Albert-Ludwigs-Universität Freiburg im Breisgau).
- Villanueva, G., Hartogh, P., 2004, The High Resolution Chirp Transform Spectrometer for the SOFIA-GREAT Instrument, *Exp. Astron.*, 18, 77–91.
- Villanueva, G. L., Hartogh, P., Reindl, L., 2006, A digital dispersive matching network for SAW devices in Chirp Transform Spectrometers, *IEEE Transactions Microwave Theory Tech.*, 54, 4, 1415–1424.
- Villanueva, G. L., Boney, B. P., Mumma, M. J., Magee-Sauer, K., DiSanti, M. A., Salyk, C., Blake, G. A., 2006, The Volatile Composition of the Split Ecliptic comet 73P/Schwassmann-Wachmann 3: A Comparison of Fragments C and B, *ApJS*, 650, 1, L87–L90.
- Villanueva, G., Mumma, M. J., Boney, B. P., Drahus, M., Paganini, L., Kueppers, M., DiSanti, M. A., Magee-Sauer, K., Hartogh, P., Jarchow, C., Milam, S., Ziurys, L. M., 2006, Submillimeter Molecular Observations Of The Split Ecliptic Comet 73P/Schwassman-Wachmann 3, DPS meeting 38, *Bulletin of the American Astronomical Society*, 38, 485.
- von Zahn, U., Baumgarten, G., Berger, U., Fiedler, J., Hartogh, P., 2004, Noctilucent clouds and the mesospheric water vapour: the past decade, *Atmos. Chem. Phys.*, 4, 2449–2464.
- Wang, Y., Jaffe, D. T., Graf, U. U., Evans II, 1994, Single-sideband calibration for CO, (13)CO, HCN, and CS lines near 345 GHz, *Astrophysical Journal Supplement Series*, 95, 2, 503–515.
- Widarta, A., Kawakami, T., Suzuki, K., 2003, Dual Channel IF Substitution Measurement System for Microwave Attenuation Standard, *IEICE Trans. Electron.*, E86-C, 8, 1580–1583.
- Williamson, R. C., Smith, H.I., 1973, The Use of Surface-Elastic-Wave Reflection Gratings in Large Time-Bandwidth Pulse-Compression Filters, *IEEE Transactions on Microwave Theory and Techniques*, 21, 4, 195–205.
- Williamson, R. C., 1976, Properties and Applications of Reflective-Array Devices, *Proceedings of the IEEE*, 64, 5, 702–710.

- Woodney, L. M., A'Hearn, M. F., Schleicher, David G., Farnham, Tony L., McMullin, J. P., Wright, M. C. H., Veal, J. M.,; Snyder, Lewis E., de Pater, Imke, Forster, J. R., Palmer, Patrick, Kuan, Y.-J., Williams, Wendy R., Cheung, Chi C., Smith, Bridget R., 2002, Morphology of HCN and CN in Comet Hale-Bopp (1995 O1), *Icarus*, 157, 1, 193–204.
- Zommerfelds, W. C., Kunzi, K. F., Summers, M. E., Bevilacqua, R. M., Strobel, D. F., Allen, M., Sawchuck, W. J., 1989, Diurnal variations of mesospheric ozone obtained by ground-based microwave radiometry, *J. Geophys. Res.*, 94, 12819–12832.



# Publications

## Publications in refereed scientific journals

**L. Paganini** and P. Hartogh, Description of a New 400 MHz bandwidth Chirp Transform Spectrometer, *Advances in Geosciences*, Vol. 7: Planetary Science (Eds. Anil Bhardwaj et al.), 55–68, World Scientific Publishing Co., 2006. ISBN-13: 978-981-270-986-8.

M. Drahus, M. Küppers, C. Jarchow, **L. Paganini**, P. Hartogh, and G. L. Villanueva, The HCN molecule as a tracer of the nucleus rotation of comet 73P/Schwassmann-Wachmann 3, *Astronomy & Astrophysics*, submitted, 2007.

**L. Paganini**, P. Hartogh, and L. Reindl, An improved method for nonlinearity detection applied to a new 400-MHz Bandwidth Chirp Transform Spectrometer, *Transactions on Systems, Signals & Devices*, 3, 4, 1–15, 2008.

**L. Paganini**, P. Hartogh, and L. Reindl, A high-accuracy method for nonlinearity detection in microwave backend systems, *IEEE Transactions on Microwave Theory and Techniques*, in preparation, 2008.

M. Drahus, **L. Paganini**, C. Jarchow, P. Hartogh, Observations of comet 17P/Holmes, in preparation, 2008.

## Contributed papers in conference proceedings

**L. Paganini**, P. Hartogh, and L. Reindl, An improved method for nonlinearity detection applied to a new 400-MHz bandwidth Chirp Transform Spectrometer, *Proceedings of the Fourth IEEE International Multi-Conference on Systems, Signals & Devices* (Summary book), 4, 381, Tunisia, 2007. ISBN: 978-9973-959-05-8.

## Circulars

M. Drahus, **L. Paganini**, L. Ziurys, W. Peters, M. Soukup, M. Begam, Comet 17P/Holmes, *IAU Circ.* (Edited by D. W. E. Green), 8891, 1, 2007.



# Acknowledgements

I would like to thank the Max Planck Institute for Solar System Research (MPS), Prof. Dr. Ulrich Christensen and Prof. Dr. Sami Solanki (the Directors of the MPS), and the International Max Planck Research School (IMPRS) for providing me with the opportunity and the financial support to carry out my research study.

I am grateful to my supervisor, Dr. Paul Hartogh, for giving me the chance to continue my research in the fascinating field of microwaves. Thanks for your guidance, support and constructive discussions.

For accepting me as his student at the University of Freiburg and for the support provided during this work, I wish to thank Prof. Dr. Leonhard Reindl. And, for his concern and interesting recommendations, thanks to Dr. William D. Walker.

I thank the coordinator of the IMPRS, Dr. Dieter Schmitt, for his tireless work and useful advice.

The members of my working group also deserve special recognition, for their useful advice and exchange of ideas: Dr. Christopher Jarchow, Dr. Miriam Rengel, Michal, Kristofer, Xianyi, Song Li, Pit, Eckhard, Helmut and Markus. Thanks to our group secretary: Frau Gerlinde Bierwirth.

I am grateful to the administrative staff of the institute (headed by Andreas Poprawa) who helped me whenever I had a problem.

In Arizona (year 2006), I had the challenge of integrating the spectrometer to the HHSMT. Such challenge would have been much more difficult without the friendly help of Dr. William Peters and the HHSMT staff. I really enjoyed while being in there, thank you.

I cannot forget two people that have given me invaluable advice about life and my scientific career: Gerónimo Villanueva and Luciano Rodriguez. Knowing both of you made my life in Germany a 'warm' place.

To the people at IEMA who gave me the chance to discover the research world, I especially thank Enrique Puliafito, Jose Luis Quero, Carlos Puliafito and Miguel Gantuz.

During my stay in Lindau and Göttingen, I have interacted with different people from all around the world. Thanks to my colleagues and friends at the institute for making these three years such an interesting experience: Jean & Silvia, Bruno, Dana, Cleme, Maya, and all of you. Because they always reply positively whenever I have questions about English grammar, thanks to Han, Ray, and Kris.

For their real and enduring friendship, my friends in Mendoza (Leo, Dani, Ariel and Andrés), who were 'there' during the good and bad times. "Esto se los dedico a ustedes".

Finally, my thanks must go to my family, who have always trusted and encouraged me to pursue what I believe in. "Gracias por apoyarme incondicionalmente en cada etapa de mi vida". And Catherine, for your patience, support and help. You make me feel that there are no horizons.



# Lebenslauf

**Name:** Lucas Paganini

**Geburt:** Am 23. Juni 1980 in Mendoza, Argentinien

**Nationalität:** Argentinisch

**Schulbildung:** 03/1993 bis 12/1997 Gymnasium "San Luis Gonzaga"

**Studium:** 02/1998 bis 12/2003 Universidad de Mendoza, Facultad de Ingeniería  
Elektronik und Telekommunikation Ingenieur  
Dissertation:  
"Experimental study of living organisms through the  
development of a microwave radiative cavity using a  
power-controlled magnetron as radiation source"

12/2004 bis 12/2007 Doktorarbeit  
Während dieser Zeit Tätigkeit als  
wissenschaftlicher Mitarbeiter am Max-Planck-Institut  
für Sonnensystemforschung in Katlenburg-Lindau